



**NTNU – Trondheim**  
Norwegian University of  
Science and Technology

# Phase Stability and Point Defects in $\text{InMnO}_3$

**Mari Reidulff**

Chemical Engineering and Biotechnology

Submission date: December 2014

Supervisor: Sverre Magnus Selbach, IMTE

Norwegian University of Science and Technology  
Department of Materials Science and Engineering



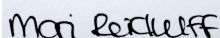
# Preface

The studies in this master thesis have been carried out at the Norwegian University of Science and Technology (NTNU), at the Department of Material Science and Engineering during the fall of 2014. My main supervisor has been Assoc. Professor Sverre M. Selbach and my co-advisor has been Ph.D. candidate Sandra H. Skjærvø. The present master thesis is a continuation of my project work *The effect of point defects on the polar and non-polar phases of hexagonal  $InMnO_3$* [1] carried out during the spring of 2014. The hypothesis and idea behind the previous project and this master thesis are attributed to Assoc. Professor Sverre M. Selbach. The author has performed all work. Since this is a continuation of my previous project[1], parts of the theory have been improved and reused in this thesis.

## Acknowledgement

I would like to give a special thank to my supervisor Sverre M. Selbach. His guidance, feedback and our discussions throughout the project have been of great importance for the final result. Not to mention his dedication to the project and knowledge about everything. The dream-team consisting of my co-supervisor Sandra H. Skjærvø, Gerhard Olsen and Didrik Småbråten need a big thanks for always keeping their door open for solving computational challenges and providing comments on my work. I want to express my gratitude to the participants on the regular ferro- and DFT meetings for showing interest and giving feedback on the project and its results. I also want to thank my family for always believing in me and supporting me. In the end I want to thank Vegar Bergum for encouraging me and being who you are.

Trondheim, 2014-12-15



Mari Reidulff



# Abstract

During the last decade hexagonal manganites ( $\text{h-RMnO}_3$ ) have been a widely researched topic. This is mainly due to their multiferroic property that makes them a potential material for use in future electronics, data storage and sensors. The multiferroic property consists of the combination of ferroelectricity and magnetic order. In general, hexagonal manganites are assigned to the polar  $P6_3cm$ -space group and show ferroelectric behaviour at room temperature. However, recent experimental and computational studies on  $\text{InMnO}_3$  have shown deviating dielectric properties for this material. Both ferroelectric and paraelectric behaviour have been detected, which have raised questions regarding which space group is the most stable for  $\text{InMnO}_3$ . The two proposed space groups in literature are ferroelectric, polar,  $P6_3cm$  and paraelectric, non-polar,  $P\bar{3}c1$ .

In this project the effect of point defects on the relative stability of  $P6_3cm$  and  $P\bar{3}c1$  is investigated through a first-principles study using density functional theory. From previous work it has been shown that interstitial and vacant oxygen decrease the energy difference between  $P\bar{3}c1$  and  $P6_3cm$ , hence disfavour the polar structure. In this project the ground-state energies for both space groups with In-vacancies are found, the phase transition between non-polar  $P\bar{3}c1$  and polar  $P6_3cm$  are investigated and the effect of point defects of the polarization of  $P6_3cm$  is studied. With In-vacancies present in  $\text{InMnO}_3$  under oxidizing (ox.) conditions the non-polar  $P\bar{3}c1$  phase has the lowest energy and is therefore the most stable. Stoichiometric  $\text{InMnO}_3$  is an insulator but has shown to turn metallic when In-vacancies under ox. conditions are present. This was found for both the polar and non-polar phase. In-O-vacancy pairs created in a reducing environment favoured the polar  $P6_3cm$  structure. Under these conditions the non-polar  $P\bar{3}c1$  phase turned metallic, while the polar  $P\bar{3}c1$  stayed insulating with some signs of shallow states in the band gap. The phase transition study revealed the presence of an activation energy barrier between stoichiometric  $P\bar{3}c1$  and  $P6_3cm$ . This activation energy barrier increased with point defects of interstitial and vacant oxygen present, decreased for In-O-vacancy pairs and disappeared for In-vacancies at ox. condition. The polarization of  $P6_3cm$  increased with point defects of vacant oxygen and decreased substantially with In-vacancies present. The study has shown the great importance of point defects for the stability of the two phases in  $\text{InMnO}_3$ , and has revealed a possible transition from insulator to metal with certain point defects present.



# Sammendrag

I løpet av det siste tiåret har heksagonale manganitter ( $\text{h-RMnO}_3$ ) vært et populært forskningsområde. Dette er hovedsakelig på grunn av deres multiferroiske egenskaper som gjør dem til potensielle materialer for bruk i fremtidig elektronikk, datalagringsenheter og sensorer. Den multiferroiske egenskapen består av en kombinasjon av ferroelektrisitet og ferromagnetisme. Heksagonale manganitter krystalliseres i den polare romgruppen  $P6_3cm$  og er vanligvis ferroelektriske ved romtemperatur. Imidlertid har nyere eksperimentelle og teoretiske studier på  $\text{InMnO}_3$  vist avvikende dielektriske egenskaper for dette materialet. Både ferro- og paraelektriske egenskaper har blitt detektert. Spørsmålet er nå hvilken romgruppe som er den mest stabile for  $\text{InMnO}_3$ . Litteraturen foreslår to ulike romgrupper; Polare  $P6_3cm$  som gir ferroelektriske egenskaper og upolare  $P\bar{3}c1$  som gir paraelektriske egenskaper.

I dette prosjektet er effekten av punktdefekter på den relative stabiliteten til  $P6_3cm$  og  $P\bar{3}c1$  studert gjennom en *ab initio*-studie ved bruk av tetthetsfunksjonalteori. Fra tidligere arbeider har det blitt vist at interstitielle oksygen og oksygenvakanser reduserer energiforskjellen mellom  $P\bar{3}c1$  og  $P6_3cm$ . I dette prosjektet er energien til grunntilstanden for begge romgruppene med In-vakanser funnet, faseovergangen mellom upolar  $P\bar{3}c1$  og polar  $P6_3cm$  undersøkt og effekten av punktdefekter på polarisasjonen av  $P6_3cm$  studert. Med In-vakanser tilstede i  $\text{InMnO}_3$  ved oksiderende (oks.) betingelser har den upolare  $P\bar{3}c1$ -fasen lavest energi og er derfor den favoriserte fasen. Støkiometrisk  $\text{InMnO}_3$  er en isolator, men har vist seg å bli metallisk når In-vakanser i et oks. miljø er tilstede. Dette ble funnet for både den polare og upolare fasen. In-O-vakanspar i et reduserende miljø favoriserte den polare  $P6_3cm$  fasen. Under slike forhold ble den upolare  $P\bar{3}c1$  fasen metallisk, mens den polar  $P6_3cm$  fortsatt var isolerende, men med tegn til tilstander i båndgapet. Studiet av faseovergangen viste at det finnes en aktiveringsenergibarriere mellom støkiometrisk  $P\bar{3}c1$  og  $P6_3cm$ . Denne energibarrieren økte med punktdefekter av interstitielle oksygen og oksygenvakanser tilstede, avtok med In-O-vakanspar og forsvant for In-vakanser ved oks. betingelser. Polarisasjonen av  $P6_3cm$  økte med oksygenvakanser tilstede og ble vesentlig redusert i tilfelle med In-vakanser. Dette prosjektet har vist at punktdefekter har stor betydning for stabiliteten til de to fasene i  $\text{InMnO}_3$ , og har avdekket en mulig overgang fra isolator til metall med visse punktdefekter tilstede.





# Contents

<b>Preface</b>	<b>ii</b>
<b>Abstract</b>	<b>iv</b>
<b>Sammendrag</b>	<b>vi</b>
<b>1 Introduction</b>	<b>1</b>
1.1 Indium manganite - why study this material? . . . . .	1
1.2 Previous work . . . . .	2
1.3 Objective . . . . .	3
<b>2 Indium manganite</b>	<b>5</b>
2.1 Hexagonal manganites . . . . .	5
2.2 Stable crystal structures for $\text{InMnO}_3$ . . . . .	6
2.3 Properties of $\text{InMnO}_3$ . . . . .	8
2.4 Crystal structure parameters . . . . .	9
<b>3 Point defects</b>	<b>11</b>
3.1 Intrinsic defects . . . . .	11
3.2 Indium vacancies . . . . .	12
3.2.1 Oxidizing environment . . . . .	13
3.2.2 Reducing environment . . . . .	13
3.3 Oxygen vacancies . . . . .	14
3.4 Interstitial oxygen . . . . .	14
3.5 Manganese vacancies . . . . .	15
3.5.1 Oxidizing conditions . . . . .	15
3.5.2 Reducing conditions . . . . .	15
3.6 Choice of defect positions . . . . .	16
3.6.1 Indium vacancies . . . . .	17
3.6.2 Oxygen vacancies in connection with indium vacancies . . . . .	18
3.7 Formation energy . . . . .	20
3.8 Limitations for experimental studies on point defects . . . . .	21

<b>4</b>	<b>Phase transitions</b>	<b>23</b>
4.1	Definitions of phase transitions . . . . .	23
4.2	Ferroelectric phase transition in hexagonal manganites . . . . .	24
4.2.1	The Landau model . . . . .	26
4.2.2	Phase transition from $P6_3/mmc$ to $P6_3cm$ . . . . .	26
4.2.3	Polarization . . . . .	27
4.3	Symmetry considerations for phase transitions . . . . .	28
4.3.1	Group/subgroup relationship . . . . .	29
4.3.2	Symmetry for $P\bar{3}c1$ , $P6_3cm$ and $P3c1$ . . . . .	30
4.4	Possible transition paths for $\text{InMnO}_3$ . . . . .	30
4.4.1	Transitions in stoichiometric and non-stoichiometric cells . . . . .	31
<b>5</b>	<b>Density functional theory</b>	<b>33</b>
5.1	The Schrödinger equation . . . . .	33
5.2	Density functional theory . . . . .	35
5.2.1	The Kohn-Hohenberg theorems . . . . .	35
5.2.2	The Kohn-Sham equations . . . . .	36
5.2.3	The exchange-correlation functional . . . . .	37
5.2.4	Result of DFT . . . . .	37
5.3	From theory to calculations . . . . .	38
5.3.1	From bulk to k-space . . . . .	38
5.3.2	Cut-off energy . . . . .	40
5.3.3	Pseudopotentials . . . . .	40
5.4	Numerical optimization . . . . .	41
5.4.1	Energy criterion . . . . .	41
5.4.2	Force criterion . . . . .	42
5.5	Types of DFT-calculations . . . . .	42
5.5.1	Calculation of minimum energy of a structure . . . . .	42
5.5.2	Density of states calculations . . . . .	43
5.5.3	Calculations of activation energies for transitions . . . . .	44
5.5.4	Polarization - Berry-Phase calculations . . . . .	46
5.5.5	Limitations of DFT . . . . .	47
5.6	Vienna Ab-initio Simulation Package (VASP) . . . . .	48

---

5.6.1	Features . . . . .	48
5.6.2	Input-files . . . . .	49
<b>6</b>	<b>Computational procedure</b>	<b>51</b>
6.1	Convergence testing . . . . .	51
6.1.1	K-point and cut-off testing . . . . .	51
6.1.2	Force testing . . . . .	52
6.2	Hubbard U and pseudopotentials . . . . .	55
6.3	The supercell approach . . . . .	55
6.4	Ground-state energy calculations . . . . .	56
6.5	Climbing image nudged elastic band calculations . . . . .	56
6.6	Berry-Phase calculations . . . . .	57
6.7	Summary of parameters . . . . .	57
<b>7</b>	<b>Results</b>	<b>59</b>
7.1	In-vacancies . . . . .	59
7.1.1	Oxidizing conditions - Only In-vacancy . . . . .	59
7.1.2	Reducing conditions - In-O vacancy pairs . . . . .	63
7.1.3	Energy difference . . . . .	70
7.1.4	Calculation of formation energy of defects . . . . .	71
7.2	Phase transition calculations . . . . .	72
7.2.1	Stoichiometric cell . . . . .	72
7.2.2	Defect cells . . . . .	73
7.2.3	Summary - activation energy barriers . . . . .	79
7.3	Calculations of polarization . . . . .	80
<b>8</b>	<b>Discussion</b>	<b>83</b>
8.1	In-vacancies . . . . .	83
8.1.1	Oxidizing conditions - Favouring the non-polar phase . . . . .	83
8.1.2	Middling reducing conditions - In-O vacancy pairs . . . . .	85
8.1.3	Energy differences for In-vacancies . . . . .	90
8.1.4	Formation energy of defects . . . . .	91
8.2	Stability of the polar and non-polar phase with point defects . . . . .	92
8.2.1	Energy differences compared to experimental . . . . .	92

8.2.2	Energy differences compared to temperature . . . . .	94
8.3	In-vacancies alter the insulating properties of $\text{InMnO}_3$ . . . . .	96
8.3.1	In-vacancies under ox. conditions lead to metallic properties . . . . .	96
8.3.2	In-O vacancy pairs leads to different behaviour of polar and non-polar phase . . . . .	99
8.3.3	Commercial approach and possible error . . . . .	102
8.4	Phase transition between $P\bar{3}c1$ and $P6_3cm$ . . . . .	102
8.4.1	Phase transition path for a stoichiometric cell . . . . .	103
8.4.2	The effect of point defects . . . . .	104
8.5	Polarization . . . . .	105
8.5.1	Comparison with experimental values . . . . .	105
8.5.2	Change in polarization with non-stoichiometric $\text{InMnO}_3$ . . . . .	106
8.5.3	Effect of volume on polarization . . . . .	108
8.6	Further work . . . . .	109
8.6.1	Experimental verification . . . . .	109
8.6.2	Computational verification . . . . .	110
8.6.3	Phonon spectra and magnetism . . . . .	111
8.6.4	Mn-vacancies and other point defects . . . . .	112
<b>9</b>	<b>Conclusion</b> . . . . .	<b>113</b>
	<b>Bibliography</b> . . . . .	<b>115</b>
	<b>Appendix A VASP</b> . . . . .	<b>121</b>
A.1	Input-files . . . . .	121
A.1.1	INCAR . . . . .	121
A.1.2	POSCAR . . . . .	122
A.1.3	KPOINTS . . . . .	122
A.1.4	Job script . . . . .	123
A.1.5	POTCAR . . . . .	124
A.2	Density of state calculations . . . . .	124
A.3	Climbing image nudged elastic band calculations . . . . .	125
A.4	Berry-Phase calculations . . . . .	125

<b>Appendix B</b>	<b>Supplementary from project work - choice of parameters</b>	<b>127</b>
B.1	Convergence testing . . . . .	127
B.2	The meaning of pseudopotential and Hubbard U . . . . .	129
<b>Appendix C</b>	<b>Results from project work</b>	<b>133</b>
C.1	Stoichiometric cell . . . . .	133
C.2	Interstitial oxygens . . . . .	135
C.3	Oxygen vacancies . . . . .	138
C.4	Energy differences . . . . .	141
<b>Appendix D</b>	<b>Vapour pressure of In and Y</b>	<b>143</b>



# Chapter 1

## Introduction

Hexagonal manganites have drawn a lot of attention in the research community the last decade. Particularly due to the fact that hexagonal manganites are both ferroelectric and antiferromagnetic, meaning they are classified as multiferroics. The market experiences a trend where technology developers try to minimize the size of their devices. This makes the multiferroicity a much-desired property, since it gives the possibility for one component to perform more than one task[2]. Examples of technological applications where the multiferroic property is desired are ferroelectric random access memory (FeRAM) and magnetic data storage[2]. Hexagonal manganites are also promising candidates for use as chemical oxygen storage for chemical looping combustion[3].

Multiferroic hexagonal manganites have demonstrated to not only be important for commercial use. The improper ferroelectric phase transition from the low-symmetric phase  $P6_3cm$  to the high-symmetric phase  $P6/mmc$  has proved to display an appropriate symmetry-breaking characteristic for explaining the Kibble-Zurek scenario[4]. The Kibble-Zurek scenario describes the phase transitions taking place right after the *Big Bang*. By studying the paraelectric/ferroelectric phase transition in hexagonal manganites a better understanding of the phase transitions that occurred during the creation of universality can be obtained.

### 1.1 Indium manganite - why study this material?

As listed above hexagonal manganites have several interesting properties and areas of application. This alone is a motivation for studying these materials further. One of the most studied hexagonal manganites is  $YMnO_3$ . This material has showed to crystallize into the polar space group  $P6_3cm$  at room temperature, and obtain ferroelectric properties[5, 6]. The same is demonstrated for other rare-earth hexagonal manganites, e.g.  $ScMnO_3$  and  $LuMnO_3$ [7]. Since  $InMnO_3$  is another member of the hexagonal manganite family the same ferroelectric

property would be expected.

InMnO<sub>3</sub> is not studied in the same extent as YMnO<sub>3</sub>, and unlike YMnO<sub>3</sub> the research done is ambiguous. Already in 1995 Greedan et al.[8] observed unusual magnetic properties for InMnO<sub>3</sub>. These were later supported by Belik et al.[9] which found no spontaneous polarization for InMnO<sub>3</sub>, meaning the material displayed paraelectric properties. Huang et al.[10] prepared samples of InMnO<sub>3</sub> by use of different synthesis routes. The different samples showed varying properties, some were ferroelectric and some paraelectric. As the discussion above indicates the properties of InMnO<sub>3</sub> is not as crystal clear as for the other hexagonal manganites, e.g. YMnO<sub>3</sub>. This makes it interesting to investigate what effects participate in deciding the dielectric properties of InMnO<sub>3</sub>.

The main discussion in literature today is regarding which crystal structure is the most stable for InMnO<sub>3</sub>. The two competing structures are polar  $P6_3cm$ , as in YMnO<sub>3</sub>, and non-polar  $P\bar{3}c1$ . Since these two structures produce two different dielectric properties, ferroelectricity and paraelectricity respectively, the characterization of which of these are most stable can help solve the mysteries around InMnO<sub>3</sub>. When preparing a sample of a material it is impossible to make a stoichiometric compound and there will always be some point defects present, see section 3. Mapping the effect different point defects have on the stability of the two crystal structures might give a better understanding of the deviating dielectric properties. The hypothesis of this project is that dissimilar thermal history and small variation in stoichiometry are the main reasons for the varying dielectric properties for InMnO<sub>3</sub> documented in literature.

## 1.2 Previous work

In previous work performed by the author[1] the effect of interstitial and vacant oxygen atoms on the stability of  $P\bar{3}c1$  and  $P6_3cm$  for InMnO<sub>3</sub> were investigated by a density functional theory study (DFT). The work showed that for a stoichiometric cell the polar phase is more stable than the non-polar phase. However, when point defects of interstitial and vacant oxygen atoms were introduced in the structure the energy difference between the two phases decreased. This indicated that non-stoichiometry and different preparation routes can affect the stability of the ferroelectric versus the paraelectric phase of InMnO<sub>3</sub>. A summary of the



results from previous work can be found in Appendix C.

### 1.3 Objective

The objective of this project is to further look into the stability of the ferroelectric and paraelectric phase of  $\text{InMnO}_3$ . As a continuation of the previous work In-vacancies will be studied to investigate the effect on the energy difference between the two phases. The polarization of the polar  $P6_3cm$ -phase is calculated, for a stoichiometric cell and cells with defects, to investigate the impact point defects have on the polarization. Based on phase transition theory, calculations are also done to find out if an activation energy barrier exists when going between the ferroelectric and paraelectric phase. What happens to this potential energy barrier when point defects are introduced in the material is also addressed.

At this point, no other studies on point defects in  $\text{InMnO}_3$  have been published. In addition no other studies have used density functional theory to investigate the potential energy barrier that has to be overcome when transferring between structures. Thus this project represents a new approach to explain the cause behind varying properties of  $\text{InMnO}_3$ . A study on point defects has in addition several other advantages. Point defects give in general a better understanding of the material, and can be used as a tool to optimize, tune and make new properties. This gives an additional motivation to the project as it is possible to both verify/invalidate the hypothesis and get a better understanding of a poorly understood material.



## Chapter 2

# Indium manganite

## 2.1 Hexagonal manganites

Hexagonal manganites ( $h\text{-RMnO}_3$ ,  $R = \text{Sc, Y, In, Ho,} \dots \text{Lu}$ ) were discovered in 1962 by Yakel et al.[5]. Since then they have been a popular research topic due to their multiferroic properties<sup>1</sup>. In hexagonal manganites ferroelectricity and antiferromagnetism exist at the same time, and they are therefore regarded as a multiferroic[7]. Alternating layers of  $R^{3+}$  and corner-sharing trigonal bipyramids of  $\text{MnO}_5$  result in the multiferroic property. Most hexagonal manganites are assigned to the polar  $P6_3cm$  structure. It would be natural to expect  $\text{InMnO}_3$  to obtain the same crystal structure and properties as the other hexagonal manganites. However, recent work by Kumagai et al.[7] has showed that the  $P\bar{3}c1$ -structure might describe the observed dielectric properties better.

$\text{InMnO}_3$  is not a very widely studied material compared to the prototypical hexagonal manganite,  $\text{YMnO}_3$ . It is quite difficult to synthesize  $\text{InMnO}_3$ [9], and that is probably the reason for few articles discussing the structure and properties. This results in a poor understanding of the material. The debate regarding the correct space group for  $\text{InMnO}_3$  is of special interest for this project. Different articles show contradicting behaviour for  $\text{InMnO}_3$ , and different research groups assign  $\text{InMnO}_3$  to different space groups. From a commercial view point the most important opportunity for  $\text{InMnO}_3$  is its electronic properties. The designated space group decide if the material is ferroelectric or paraelectric, and emphasize the importance of understanding the structure of this material.

---

<sup>1</sup>A multiferroic material is a material that combines two or more of the following properties: ferromagnetism, ferroelectricity, ferroelasticity and/or ferrotoroidicity[2].

## 2.2 Stable crystal structures for $\text{InMnO}_3$

As mentioned, the debate regarding the crystal structure for  $\text{InMnO}_3$  is between two space groups,  $P\bar{3}c1$  and  $P6_3cm$ . See Figure 2.1 and 2.2 for an illustration of these two. The main difference between the two structures is that the hexagonal  $P6_3cm$  structure is polar non-centrosymmetric, while the trigonal  $P\bar{3}c1$  structure is non-polar centrosymmetric. In the polar  $P6_3cm$ -structure the  $\text{MnO}_5$  trigonal bipyramids tilt and trimerize with a trimerization phase of  $n \cdot 60^\circ$ , where  $n$  is an integer[7]. The result of this tilting is a net ferroelectric polarization caused by an additional displacement of the  $\text{In}^{3+}$  sublattice relative to the layers of  $\text{MnO}_5$  trigonal bipyramids. Materials that crystallize in the non-polar  $P\bar{3}c1$ -structure will not obtain ferroelectricity. This is due to trimerization of the  $\text{MnO}_5$  trigonal bipyramids in intermediate angles, causing the inversion centre to be retained. All figures of the  $\text{InMnO}_3$ -structure presented in this project are made by use of the visualizing software Vesta[11].

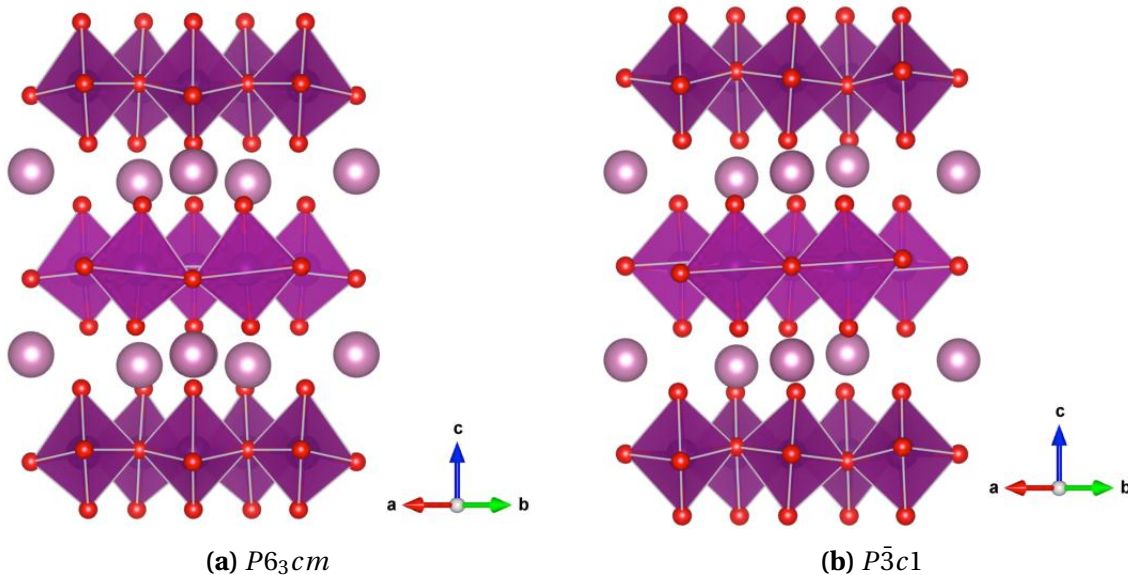


**Figure 2.1:**  $P6_3cm$ -structure, a), and  $P\bar{3}c1$ -structure, b), for  $\text{InMnO}_3$ . The structures show one unit cell. The positions and lattice parameters are based on experimental work by Kumagai et al.[7]. The figures are made by the visualization tool Vesta[11].

Lee et al. [12] present a nice way of showing one of the structural differences between  $P\bar{3}c1$  and  $P6_3cm$ , which results in absence of spontaneous polarization, paraelectricity, and spon-

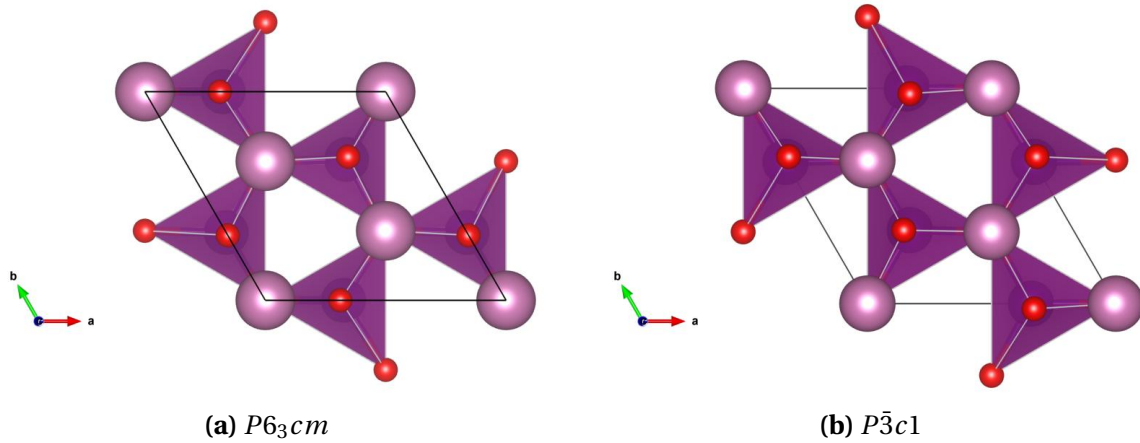


**Figure 2.2:**  $P6_3cm$ -structure, a), and  $P\bar{3}c1$ -structure, b), for InMnO<sub>3</sub> seen along the  $c$ -axis. Note the difference in the tilting of the MnO<sub>5</sub>-trigonal bipyramids by examining the apical oxygen placed in the middle of each trigonal bipyramid.

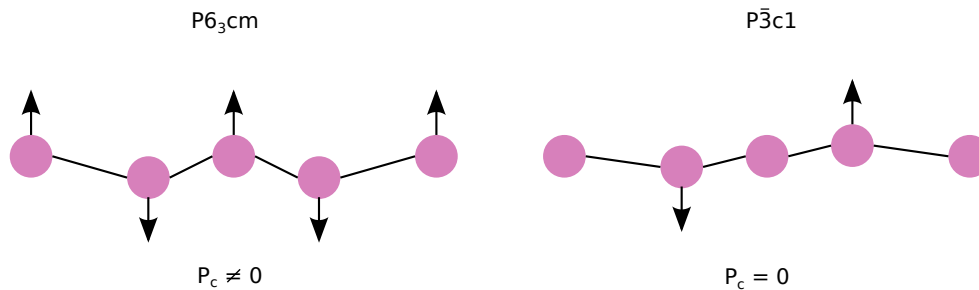


**Figure 2.3:** Sketch of the different displacements of the In-atoms in the In-layer for the  $P\bar{3}c1$ -phase compared  $P6_3cm$ [12].

taneous polarization, ferroelectricity. Figure 2.3 show the In-layer along the  $c$ -axis in both structures. This can also be observed in 2.1 by looking at the In-layer (pink atoms). The figure shows that the In-atoms have an up-down-up-down-up configuration in the  $P6_3cm$ -structure, leading to a net polarization. In the  $P\bar{3}c1$ -structure they have a none-down-none-up-none configuration, leading to no net polarization. This combined with the specific tilting of the trigonal bipyramids result in the respective properties. A more thorough explanation of this is given in section 4.2.2.

Already in 1994 J. E. Greedan et al.[8] observed unusual magnetic properties for InMnO<sub>3</sub>. They noticed that the length of the  $c$ -axis for InMnO<sub>3</sub> was substantially larger compared to

the *c*-axis for other hexagonal manganites, R-MnO<sub>3</sub>, regardless of what the R-ion represented. This indicates that the bonding between In and the Mn-O-bipyramids is weaker than in other hexagonal manganites, and might be a reason for deviating properties for InMnO<sub>3</sub>.

### 2.3 Properties of InMnO<sub>3</sub>

Different synthesis routes for InMnO<sub>3</sub> have demonstrated to result in different properties. Huang et al.[10] prepared InMnO<sub>3</sub> by a solid-state reaction method with the following preparation route: In<sub>2</sub>O<sub>3</sub> (99.999%) and MnO<sub>2</sub> (99.99%) powders in a stoichiometric ratio were ground, pressured into four pellets and heated at 980<sup>0</sup> C in air. The four pellets were then cooled in four different ways, see Table 2.1. After cooling the dielectric behaviour of each pellet was investigated. The experiments showed different dielectric behaviour for the four different preparation routes. Some displayed paraelectric properties, while other displayed ferroelectric properties. This is summarized in Table 2.1. Polarization hysteresis loop measurements proposed by Belik et al.[9] showed that the hysteresis loop for InMnO<sub>3</sub> is not ferroelectric. They therefore concluded that InMnO<sub>3</sub> will behave like a paraelectric in the temperature and electric-field ranges studied. These observations are supported by similar experimental observations done by Kumagai et al.[7].

**Table 2.1:** Cooling paths for synthesizing of InMnO<sub>3</sub> from experiments prepared by Huang et al.[10] giving different dielectric properties.

Name	Synthesis route	Dielectric properties
IMO-a	Slowly cooled (2°C/h) from 980°C	Polar (ferroelectric)
IMO-b	Furnace cooled	Polar matrix with non-polar regions
IMO-c	Quenched from 950°C*	Long-range non-polar regions
IMO-d	Quenched from 650°C*	Polar (ferroelectric)

\*The samples was cooled slowly (10<sup>0</sup>C/h from 980<sup>0</sup>C) until they reached the temperature where they were quenched from.

Both Kumagai et al.[7] and Lee et al.[12] have performed DFT-calculations on InMnO<sub>3</sub>, comparing *P*6<sub>3</sub>*cm* and *P* $\bar{3}$ *c1*. This is the "experimental" approach that is going to be used in this project, and their results will therefore be important for comparison. The conclusions drawn from the two studies are contradicting. Kumagai's calculations suggest that the *P* $\bar{3}$ *c1*-

structure is the most stable, while Lee's calculations favour  $P6_3cm$ . Although the two studies favour different crystal structures, both showed that the energy difference between the two proposed structures is very small compared to other hexagonal manganites,  $\text{RMnO}_3$  (R=Sc, Lu, Y)[7].

As described in this section the dielectric properties and structure of  $\text{InMnO}_3$  are not agreed upon in literature. The main point to emphasize from recent studies is that the energy difference between  $P\bar{3}c1$  and  $P6_3cm$  for  $\text{InMnO}_3$  is minimal. This means the two structures are almost equally stable. In addition, the fact that different preparation methods yield different dielectric properties might indicate that the synthesis route and surroundings affect the structure  $\text{InMnO}_3$  crystallize into.

## 2.4 Crystal structure parameters

Kumagai et al.[7] used powder XRD to obtain the atomic positions for both  $P\bar{3}c1$  and  $P6_3cm$ . These values are used as a basis for DFT-calculations performed in this project. The lattice parameters for  $P\bar{3}c1$  and  $P6_3cm$  are given in Table 2.2 and the atomic positions are given as fractional coordinates in Table 2.3.

**Table 2.2:** Lattice parameters, a and c, for the  $P\bar{3}c1$  and  $P6_3cm$ -structure for  $\text{InMnO}_3$  from experimental work by Kumagai et al.[7].

Structure	Lattice parameter, a [Å]	Lattice parameter, c [Å]	Volume [Å <sup>3</sup> ]
$P\bar{3}c1$	5.8846	11.4850	344.44
$P6_3cm$	5.8846	11.4854	344.44

**Table 2.3:** Atomic positions given in fractional coordinates for the  $P\bar{3}c1$  and  $P6_3cm$ -structure for  $\text{InMnO}_3$  from experimental work by Kumagai et al.[7].

Structure	Site	x	y	z
$P\bar{3}c1$	In1	1/3	2/3	0.51674(8)
	In2	0	0	0
	Mn	0.6587(10)	0	1/4
	O1	0	0	1/4
	O2	1/3	2/3	0.7312(7)
	O3	0.6829(25)	0.0241(10)	0.0858(2)
	$P6_3cm$	In1	0	0
In2		1/3	2/3	0.2383(6)
Mn		0.3250(10)	0	0
O1		0.3117(22)	0	0.174911
O2		0.6466(18)	0	0.3445(10)
O3		0	0	0.4746(20)
O4		1/3	2/3	0.0077(20)



## Chapter 3

# Point defects

A defect is an imperfection in the crystal structure that differentiates a perfect crystal, which can only exist at 0K, from a crystal at temperatures above 0K. In this project only point defects, one subgroup of defects, are considered. Point defects do not extend for more than a few interatomic distances in any direction in the crystal[13]. They can be further divided into intrinsic and extrinsic point defects. Intrinsic point defects, also called structural defects, involve removing or adding an atom of one of the species of the molecule. Extrinsic defects are defects that result from doping with an impurity atom[14].

### 3.1 Intrinsic defects

In this project only intrinsic defects are relevant. Intrinsic defects can be divided into two different categories, vacancies and interstitials. A vacancy represents the removal of an atom in a perfect periodic lattice, leaving a vacant site in the crystal structure. An interstitial represents an extra atom placed in a vacant hole in a perfect periodic lattice. Figure 3.1a and 3.1b give a schematic of a vacancy and interstitial point defect. A certain number of intrinsic defects will always be present in a pure material due to thermodynamic considerations. It exists a thermodynamic equilibrium concentrations of defects for all materials[15]. This equilibrium concentration corresponds to the minimum free Gibbs energy of the material, which depends on both configurational entropy and the enthalpy of defect formation. Exposing the material to a certain environment, e.g. an oxygen rich environment to induce interstitial oxygen or a low partial pressure of oxygen to favour oxygen vacancies, can increase the number of defects. In this project In-vacancies are considered, but defect equations for oxygen vacancies and interstitial oxygen are included as well. Calculations for the latter were performed in a previous project [1] and the results can be found in Appendix C.

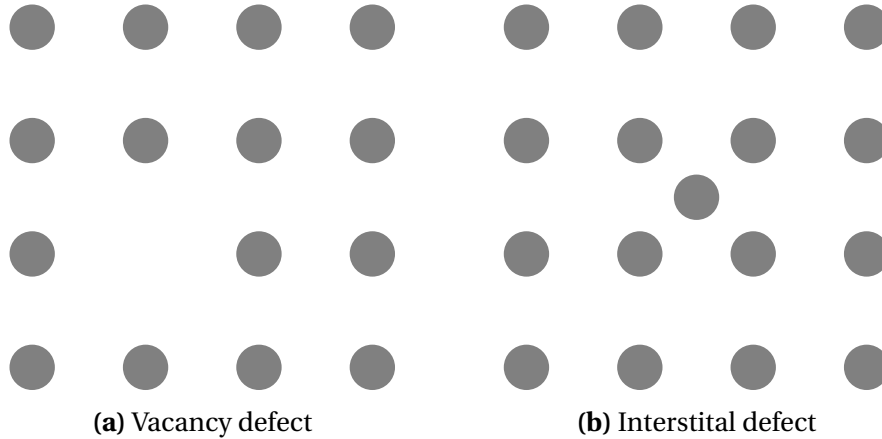


**Figure 3.1:** Sketch showing the two different type of point defects considered, a) the presence of a vacant atom and b) an atom at an interstitial position.

### 3.2 Indium vacancies

The stability of the ferroelectric versus the paraelectric phase could be connected to the fundamental differences in the  $\text{In}^{3+}$ -cation compared to other  $\text{R}^{3+}$ -cations. In has filled 4d-orbitals ( $\text{In}^{3+}:[\text{Kr}]4s^24p^64d^{10}$ ) in contrast to for instance Y which has unoccupied 4d-orbitals ( $\text{Y}^{3+}:[\text{Kr}]4s^24p^64d^0$ ). Since the d-orbitals in In are completely filled the formally unoccupied 5s and 5p-orbitals have low enough energy to bind covalently to O-2p. This results in occupied In-5s states at the bottom of the valence band[7]. For  $\text{YMnO}_3$  the energy differences between the valence band, Y-5s and O-2p states, are substantially higher. Therefore the possibility for covalency between O-2p and Y-5s is negligible. Compared to other hexagonal manganites the  $a$  lattice parameter is smaller than expected and  $c$ -lattice parameter larger than expected for  $\text{InMnO}_3$ [9]. DFT-calculations performed by Kumagai et al.[7] and experiments by Greedan et al.[8] demonstrate this trend. The extended  $c$  lattice parameter means that the layers of In and  $\text{MnO}_5$  bipyramids are further apart. This is perhaps an effect of the increased covalency between In and O.

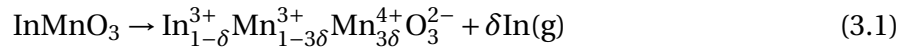
The origin of ferroelectricity in hexagonal manganites ( $\text{h-RMnO}_3$ ) is tilting of the  $\text{MnO}_5$ -trigonal bipyramids compared to the R-layer, see section 4.2.2. The additional In-O covalency makes it harder to tilt the  $\text{MnO}_5$  bipyramids. This could be a reason for the low energy differences between the paraelectric  $P\bar{3}c1$ -phase and ferroelectric  $P6_3cm$ -phase in  $\text{InMnO}_3$ . In

contrast,  $\text{YMnO}_3$  is clearly favouring  $P6_3cm$ . Possibly because the negligible Y-O covalency results in less resistance against tilting.

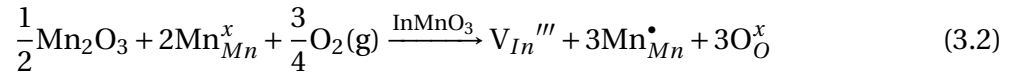
Recently it has been shown that a large Y deficiency is possible for  $\text{YMnO}_3$  [16]. It is likely that this is the case for  $\text{InMnO}_3$  as well. In-vacancies are studied in detail in this project due to the possible effect the difference in R-cation, for instance In versus Y, has on phase stability. In connection to the topics discussed above it is expected that a study on In-vacancies will increase the understanding of  $\text{InMnO}_3$ . For In-vacancies it is important to both consider vacancies formed under oxidizing and reducing conditions. Note that the defect reactions written below takes into account how the non-stoichiometry can arise, in this case by evaporation. The Kröger-Vink equations do not cover this.

### 3.2.1 Oxidizing environment

Under oxidizing condition the probability of oxygen vacancy formation is small. Charge compensation is therefore believed to happen only on Mn-atoms. The defect reaction for an indium vacancy in an oxidizing environment is given by the following:

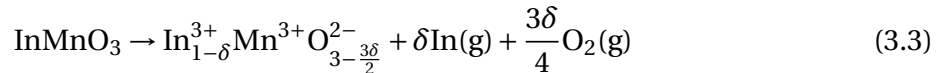


Written in Kröger-Vink notation this becomes:

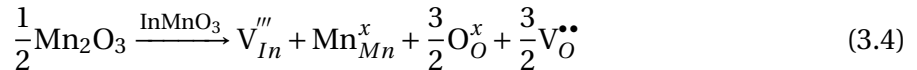


### 3.2.2 Reducing environment

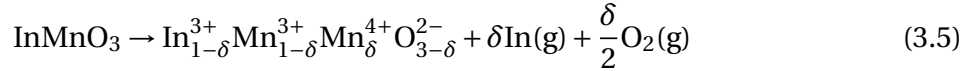
Under reducing conditions oxygen vacancies are favoured and preferred for charge compensation. The defect reaction for an indium vacancy in a very reducing environment is given by the following:



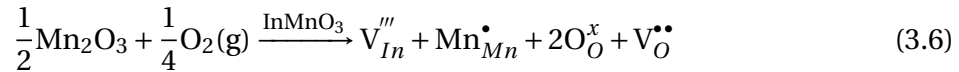
Written in Kröger-Vink notation this becomes:



However, this is not very likely to happen nor easy to simulate by calculations. When removing three electronegative oxygen atoms in proximity to an In-vacancy a very unstable structure is created. To simulate reducing conditions a middling reducing environment is used instead. The charge compensation will then be by creating one oxygen vacancy and oxidize one Mn-atom from 3+ to 4+. The reaction is given as the following:

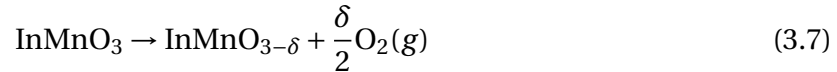


Written in Kröger-Vink notation this becomes:

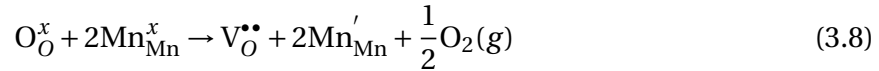


### 3.3 Oxygen vacancies

The defect equation for an oxygen vacancy in the InMnO<sub>3</sub>-structure is given by the following:



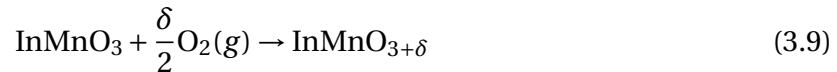
Written in Kröger-Vink notation this becomes:



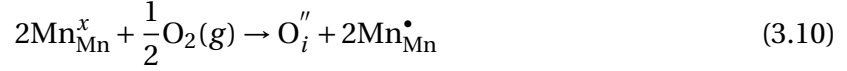
It is assumed that the charge compensating electrons are localized on Mn because Mn has several possible oxidation states, while In only have one oxidation state. For one oxygen vacancy it is assumed that two Mn-atoms will be affected. The oxidation state of the two Mn-atoms will be reduced from +3 to +2 and Mn changed from 3d<sup>4</sup> to 3d<sup>5</sup>.

### 3.4 Interstitial oxygen

The defect equation for an interstitial oxygen in the InMnO<sub>3</sub>-structure is given by the following:



Written in Kröger-Vink notation this becomes:



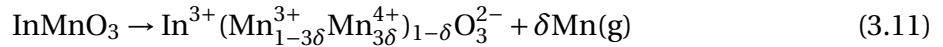
With the same explanation as for oxygen vacancies it is assumed that the charge compensating holes are localized on Mn. In this case the valence of the Mn-atoms will be oxidized from +3 to +4 and Mn change from  $3d^4$  to  $3d^3$ .

## 3.5 Manganese vacancies

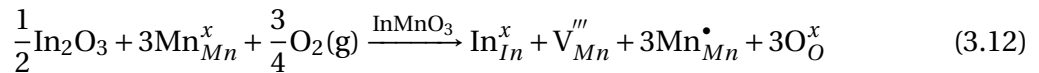
Manganese vacancies are also a possibility. Like oxygen, manganese is present in all hexagonal manganites. It would therefore be of interest to examine the effect manganese vacancies have on the stability of the paraelectric versus the ferroelectric phase of  $\text{InMnO}_3$ . Like In-vacancies, manganese vacancies can be present in both oxidizing and reducing conditions.

### 3.5.1 Oxidizing conditions

The defect reaction for a manganese vacancy in an oxidizing environment is given by the following:

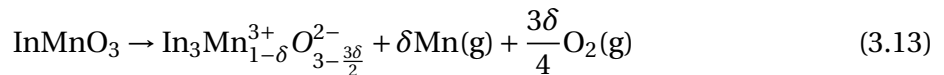


Written in Kröger-Vink notation this becomes:

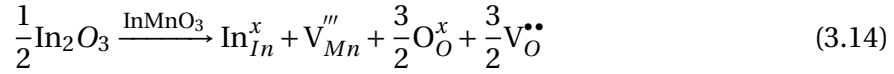


### 3.5.2 Reducing conditions

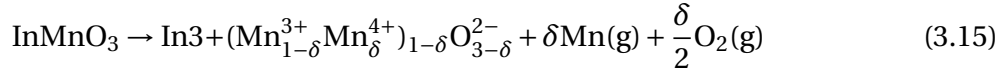
The defect reaction for a manganese vacancy in a reducing environment is given by the following:



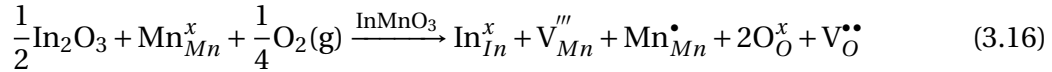
Written in Kröger-Vink notation this becomes:



As for indium vacancies, middling reducing conditions are most likely to produce the most stable structure. The defect reaction for creating a manganese vacancy in middling reducing conditions is given as the following:



Written in Kröger-Vink notation this becomes:



It is expected that a Mn-vacancy will be followed by local charge compensation on the other Mn-atoms in the Mn-plane. This because both In and O have completely filled orbitals in the outer shell,  $\text{O}^{2-} [3s^2]$  and  $\text{In}^{3+} [4d^{10}]$  [17], while Mn occurs as both  $\text{Mn}^{2+}$ ,  $\text{Mn}^{3+}$  and  $\text{Mn}^{4+}$ . By assuming that charge compensation occur on every other Mn-atom, as illustrated in Figure 3.2, one Mn-vacancy will affect three other atoms in the unitcell. The figure shows four unitcells put together in a supercell since one unitcell is not sufficient to include all relevant atoms. If calculations were performed on this supercell a total of four out of twelve Mn-atoms will be affected, see Figure 3.2. This makes the calculations represent something far from a real situation. Expanding the number of cells even more could be a solution to the problem, but this would also be very computationally challenging. Therefore, Mn-vacancies are not considered further in this project.

### 3.6 Choice of defect positions

Defect positions are chosen by one important factor, symmetry inequivalence. Symmetry inequivalent positions are unique positions in a unit cell. Therefore symmetry equivalent positions of point defects will have the same effect on properties and stability. Thus, it is only necessary to test symmetry inequivalent point defect positions.

As stated in section 3.2, In-vacancies can arise as a result of two different mechanisms regarding if  $\text{InMnO}_3$  is present in an oxidizing or reducing environment. In theory it is not verified which of these is most favourable. Therefore both mechanisms have to be tested for all va-

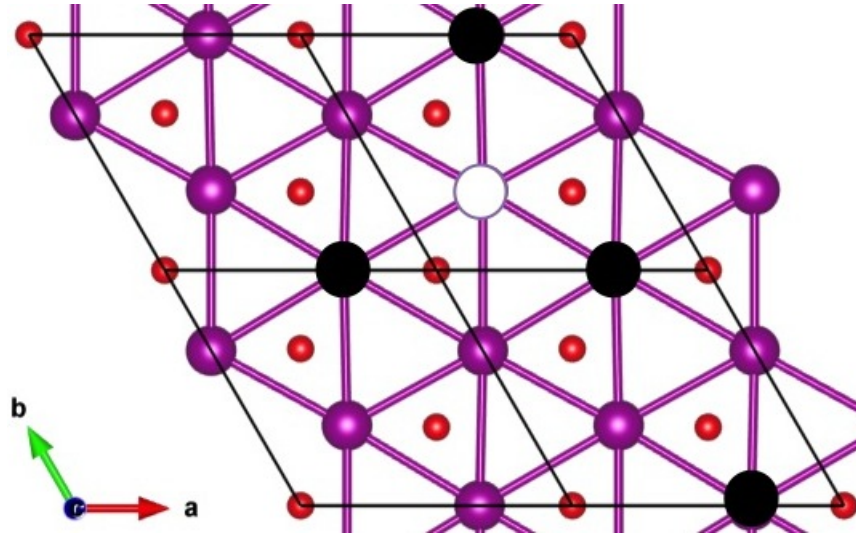


**Figure 3.2:** Illustration of the Mn-layer for a  $2 \times 2 \times 1$  supercell in  $\text{InMnO}_3$  seen along the  $c$ -axis. The white atom represents a Mn-vacancy and the black atoms represent oxidized  $\text{Mn}^{4+}$ .

cancy positions. Point defect positions for interstitial oxygen and vacant oxygen can be found in Table C.3 and C.6.

### 3.6.1 Indium vacancies

As observed in Table 2.3 the  $P\bar{3}c1$ - and  $P6_3cm$ -structure have two symmetry inequivalent positions for In. It is therefore relevant to test the effect on the ground-state energy when removing an In-atom for both these positions. The defect positions are summarized in Table 3.1. Figure 3.3 shows their positions in the two space groups.

**Table 3.1:** Indium vacancy positions in the  $P\bar{3}c1$ - and  $P6_3cm$ -structure for  $\text{InMnO}_3$ .

Structure	Site	x	y	z
$P\bar{3}c1$	In1	1/3	2/3	0.51674(8)
	In2	0	0	0
$P6_3cm$	In1	0	0	0.2674(6)
	In2	1/3	2/3	0.2383(6)

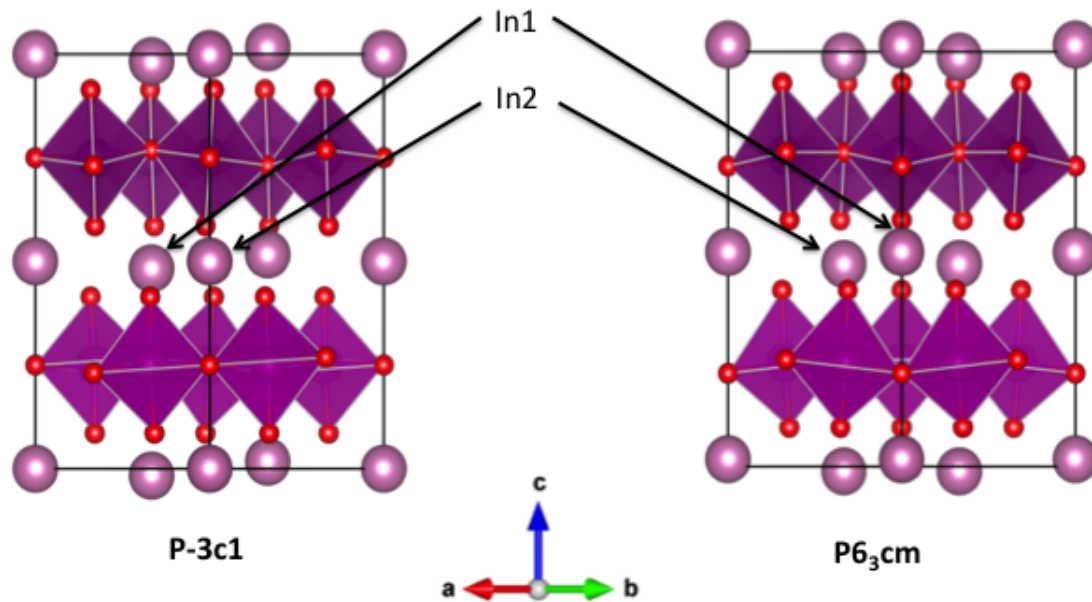


**Figure 3.3:** The  $P6_3cm$  and  $P\bar{3}c1$  structure showing the positions of the different In-vacancy positions listed in Table 3.1.

### 3.6.2 Oxygen vacancies in connection with indium vacancies

For the middling reducing conditions oxygen vacancies are created. When choosing defect positions it is necessary to do one calculation for each of the different oxygen vacancy positions combined with each In. In the  $P6_3cm$  structure it exists four symmetry inequivalent positions, two planar positions placed in the Mn-plane and two apical positions placed above the Mn-atom. However only three of these positions are tested because two of the positions gives approximately the same geometry, hence the same result. Since it exists two different position of the In-atoms, see Table 3.1, the different oxygen positions are relevant for both the In1- and In2-vacancy. The oxygen positions related to In2 are symmetry equivalent positions of those for In1. It is chosen to use a nomenclature for the oxygen vacancy positions related to their position relative to the In-vacancy. This makes it easier to compare relevant energy differences between  $P\bar{3}c1$  and  $P6_3cm$  later in the project. There are a total of three different categories. These are listed below and illustrated schematically in Figure 3.4:

**O-type1** Right above/below the In-vacancy in the Mn-layer.

**O-type2** Slanting above/below the In-vacancy.



**O-type3** Slanting above/below the In-vacancy in the Mn-layer.

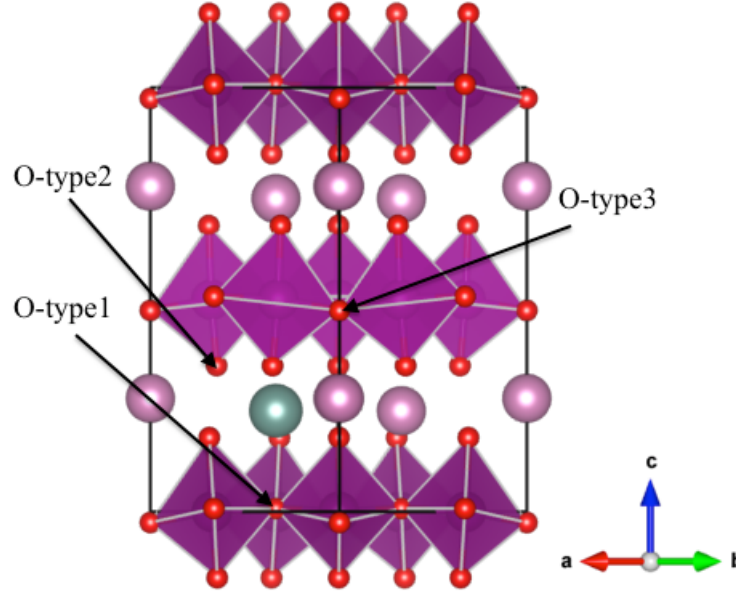


**Figure 3.4:** The  $P6_3cm$  structure showing an In-vacancy, green atom, and the relative position of each oxygen vacancy, O-type1, O-type2 and O-type3 respectively. The same is equivalent for  $P\bar{3}c1$ .

The oxygen positions for  $P6_3cm$  are listed in Table 3.2 with an explanation of their positions compared to the respective In vacancy. For  $P\bar{3}c1$  there exist a total of three symmetry inequivalent oxygen positions, two planar in the Mn-plane and one apical. The positions are given in Table 3.3. Some of the positions for oxygen vacancies differ from the symmetry inequivalent positions listed in Table 2.3. These are just examples of symmetry equivalent positions.

**Table 3.2:** Oxygen vacancy positions in the  $P6_3cm$ -structure for  $\text{InMnO}_3$ .

In-atom	Site	O-type	Position
In1	O1	O-type2	(0.311,0,0.17491)
	O3	O-type1	(0,0,0.474620)
	O4	O-type3	(1/3,2/3,0.00772)
In2	O1	O-type2	(0, 0.311, 0.17491)
	O3	O-type3	(0,0,0.47462)
	O4	O-type1	(1/3,2/3,0.00772)

**Table 3.3:** Oxygen vacancy positions in the  $P\bar{3}c1$ -structure for  $\text{InMnO}_3$ .

In-atom	Site	O-type	Position
In1	O1	O-type3	(0,0,1/4)
	O2	O-type1	(1/3, 2/3,0.23126)
	O3	O-type2	(0.31708,0.34119,0.41418)
In2	O1	O-type1	(0,0,1/4)
	O2	O-type3	(1/3,2/3,0.23126)
	O3	O-type2	(0.34119,0.31708,0.08582)

### 3.7 Formation energy

To determine which defects are most thermodynamically favourable for  $\text{InMnO}_3$  it is necessary to calculate the formation energy of the different defects. To calculate the formation energy of a defect the following equation is used[18]:

$$E_f[X^q] = E_{\text{tot}}[X^q] - E_{\text{tot}}[b] - \sum_i n_i \mu_i + qE_F + E_{\text{corr}} \quad (3.17)$$

where  $E_{\text{tot}}[X^q]$  is the energy of a supercell with a defect,  $E_{\text{tot}}[b]$  the energy of a perfect stoichiometric supercell of the same size,  $n_i$  the number of defects added ( $n_i > 0$ ) or subtracted ( $n_i < 0$ ),  $\mu_i$  the defect atoms respective chemical potential,  $q$  the charge,  $E_F$  the Fermi-energy and  $E_{\text{corr}}$  the correction term for a finite k-point sampling for shallow defects or for elastic/electrostatic interactions between supercells.

Fortunately, by some simple assumptions the two last terms can be neglected. The total charge,  $q$ , equal zero which eliminates the  $qE_F$  term. Also, when using a supercell a single defect will in principle evolve into a periodic array of defects that will interact with each other, see explanation of this in section 5.3.1. By choosing a large enough supercell these defect-defect interactions will be negligible[18]. It is assumed that the supercell used in this project is large enough for the purpose. Regarding shallow defect levels the correction will be zero when using a gamma-centered k-mesh as done in this project. In addition, the electrostatic potential for the defect will align with the bulk potential when the supercell is large [18, 19], meaning  $E_{\text{corr}}$  can be neglected as well.

By taking into account the assumptions listed above the formation energy for an In-vacancy and an In-O-vacancy pair can be calculated by equation 3.18 and 3.19 respectively:

$$E_{f,\text{defect}} = E_{\text{tot},\text{defect}} - E_{\text{tot},\text{perfect}} + \mu_{In} \quad (3.18)$$

$$E_{f,\text{defect}} = E_{\text{tot},\text{defect}} - E_{\text{tot},\text{perfect}} + \mu_{In} + \mu_O \quad (3.19)$$

### 3.8 Limitations for experimental studies on point defects

A computational approach is chosen to investigate point defects in this project. This because there are several limitations when it comes to observing point defects by experimental methods. This section will briefly explain some of the challenges regarding the different experimental methods available.

**XRD** (X-ray diffraction) provides a diffractogram or diffraction pattern of the structure, but only detects long-range order. That means point defects will be impossible to detect directly since they are not periodic. However, for large concentrations of defects changes in the average structure can be detected. A particular problem regarding  $\text{InMnO}_3$  is that the two structure  $P\bar{3}c1$  and  $P6_3cm$  have the same extinction rules for Bragg reflections[7]. It will therefore be hard to distinguish between polar and non-polar samples.

**TEM** (Transmission electron microscopy) provides a local diffraction pattern, opposite to XRD. However, it will have the same problem as XRD since it only detects long-range order.

**XPS** (X-ray photoelectron spectroscopy) is a surface sensitive spectroscopy technique. Since surface and bulk for a material do not have the same defect concentrations and conditions this technique will not disclose the effects of defects in bulk.

**EELS** (Electron energy loss spectroscopy) measures chemical composition and oxidation states as an average over an area. It is a device used with TEM and will therefore experience the same limitations as TEM.

**TGA** (Thermogravimetric analysis) is only bulk sensitive and gives information about weight change in a sample during change in temperature. Since the method is bulk sensitive, it

only gives macroscopic properties and will not reveal the local effects around a defect.

**PDF** (Pair distribution function) is probably the tool that is closest to disclose the effect of point defects. The technique detects short-range order, but is limited by the need of a substantial amount of defects to give a useful result. This might not be the case for all materials.

**EXAFS** (Extended X-Ray absorption fine structure) use low-energy X-ray radiation to excite electrons and give information about local structure. It requires a high concentration of point defects and is therefore limited to the same applications as PDF. In addition, due to low resolution EXAFS is not able to detect anything else than the coordination number for cations, and that with an accuracy of +/-1.

The limitations of different experimental techniques are many. Density functional theory solves this by providing a tool that can accurately describe point defects in a material and its effect on properties and energy. The problem with DFT is that it is not "real" and is based on several assumptions that are going to be covered in Section 5. Despite the fact that DFT is not "real" it the best tool available to give an indication on the effect of point defects in a material.

## Chapter 4

# Phase transitions

This section covers a theoretical introduction to phase transitions, as well as a description of the paraelectric to ferroelectric phase transition for  $\text{InMnO}_3$ . The introduction is mainly based on the book "The Physics of Phase Transitions" by Papon et al.[20]. This book is recommended if a more thorough explanation of the phenomena and mathematical aspects is desired.

### 4.1 Definitions of phase transitions

Stølen and Grande[21] defines a phase as a state that has a particular composition and also definite, characteristic chemical and physical properties. Several phases with identical composition can exist. A phase can be in the solid, liquid or gas state. For some materials it also exists more than one crystalline state[21]. The phases discussed in this project are different crystalline states of the same chemical compound. A phase transition is then a transition where a compound changes its state, from one phase to another. Phase transitions can be divided into two measurable categories with regard to their thermodynamic behaviour[20]:

- A first-order phase transition is a transition with latent heat, resulting in discontinuous thermodynamic quantities as enthalpy and entropy (first derivative of Gibbs energy).
- A second-order transition is a transition without latent heat, resulting in continuous entropy and enthalpy, but discontinuous heat capacity (second derivative of Gibbs energy).

Another viewpoint for categorizing phase transitions is the order parameter. The order parameter is a physical quantity that is defined to be zero at the most symmetric case and non-zero at the least symmetric case[20]. In case of a paraelectric/ferroelectric phase transition, which is relevant for this project, the amplitude of one certain vibrational mode is the order parameter[22]. When the amplitude of this vibrational mode is zero (meaning the vibrational mode has freezed in an outer position) the polarization is non-zero and the material is in the

ferroelectric state. When the amplitude is non-zero the polarization is zero and the material is in the paraelectric state. Transitions can then be characterized based on the existence of an order parameter:

- *Transitions with no order parameter:* The two symmetry groups does not necessary have a group/subgroup relationship, see section 4.3.1. These transitions are always first-order transitions with latent heat, and therefore have an activation energy barrier.
- *Transition where an order parameter can be defined:* The low symmetric phase is a subgroup of the high symmetric phase, see section 4.3.1. If the order parameter is continuous at the transition it is a second-order transition, giving no latent heat and no activation energy barrier. If the order parameter is discontinuous at the transitions it is a first-order transition with latent heat giving an activation energy barrier.

## 4.2 Ferroelectric phase transition in hexagonal manganites

A paraelectric material is a polarizable insulator, meaning the charges in the material are displaced when an electric field is applied. A paraelectric material is most often centrosymmetric, in contrast to a ferroelectric material that is non-centrosymmetric. For a ferroelectric material spontaneous electric polarization appears below a certain temperature, the Curie temperature due to orientation of dipoles[20]. Because a ferroelectric material is non-centrosymmetric the lack of symmetry results in a net polarization when all dipoles are added up. Ferroelectric materials, both polycrystalline and monocrystalline, often consist of ferroelectric domains. This because the structural displacement causing ferroelectricity can be directed in different ways, e.g. the  $\text{MnO}_5$ -trigonal bipyramids in  $\text{InMnO}_3$  can tilt in six different direction resulting in six different structural domains[23]. A domain is defined as an area where all dipole moments are aligned in the same direction. Each domain corresponds to a different direction of the dipole moment, hence a different direction of the spontaneous polarization[24]. The net polarization in a ferroelectric material, without an applied electric field, is the vector sum of the polarization of the different domains. When an electric field is applied the domains with favourable orientation of the polarization grow on the expense of the others[24]. The material is *saturated* when all dipole moments are aligned in the same direction. The result is that a smaller electric polarization is detected for the ferroelectric material without an applied electric field than a saturated material. Figure 4.1 shows the domains in a ferroelectric

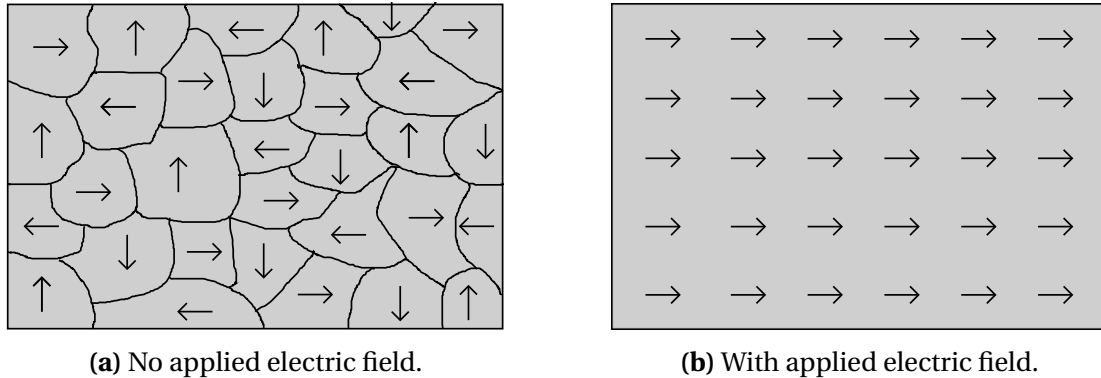


**Figure 4.1:** Sketch of how the polarization in ferroelectric materials have different direction in different domains, but is directed in the same direction when applying an electric field.

material without an applied field, 4.1a, and with an applied field, 4.1b.

The phase transition from paraelectric to ferroelectric can either be first- or second order. Ferroelectric/paraelectric phase transitions can be grouped into two categories:

**An order/disorder transition** is characterized by substitution of atoms in a structure, a typical phase transition in alloys. A small displacement might follow the substitution. By lowering the temperature the structure goes from one phase to another with a higher degree of ordering. An example of this is the transition from  $\beta$ -brass to  $\beta'$ -brass (CuZn)[25]. In the disordered high-temperature structure Cu and Zn are arranged in a random way at the corners and centre of a *bcc*-lattice. When the temperature decreases it transforms into an ordered structure, and form a primitive cube with Cu at cube corners and Zn at cube centre.

**A displacive transition** consists of finite displacements of atoms or molecular rotation in a crystal lattice. The low-temperature phase can be seen as a distorted version of the high-temperature phase. The atoms move collectively, yielding an overall change in the structure, but with no change in composition. The transition is characterized by the group/subgroup relationship between the space groups of the different phases explained in section 4.3.1.

### 4.2.1 The Landau model

The Landau theory is based on the definition of an order parameter,  $\Gamma$ , which describes the cause of the transition. It is related to the change in a macroscopic property during the phase transition. This macroscopic property can be strain, average site occupancy or crystallographic distortion[21]. The physical property measured and connected to this order parameter often scales proportionally or quadratically with the order parameter.

A soft mode can exist for a phase transition between two crystal structures where the space group of the low-symmetry structure is a subgroup of the space group of the high-symmetry structure[21]. A soft mode is a vibrational mode<sup>1</sup> where the frequency decreases and reach zero when it approaches the Curie temperature,  $T_C$ , from above[20]. When this mode has a frequency of zero the displacements caused by the vibrations freeze into the structure and cause ferroelectricity for  $T < T_C$ . This is the basis of the Landau model.

### 4.2.2 Phase transition from $P6_3/mmc$ to $P6_3cm$

The nature of the ferroelectric phase transition from the high-temperature paraelectric phase,  $P6_3/mmc$ , to the low-temperature ferroelectric phase,  $P6_3cm$ , has been widely debated. Fennie et al.[22] performed first-principles density functional theory calculations on possible transition paths for the ferroelectric/paraelectric phase transition in  $YMnO_3$ . They concluded that the most likely path is a second-order transition where a  $K_3$  phonon is frozen into the structure, resulting in a direct transition from the paraelectric  $P6_3/mmc$  phase to the ferroelectric  $P6_3cm$  phase. This is supported by experimental work covering an *in situ* high-temperature synchrotron x-ray powder diffraction study by Kim et al.[27], as well as high-resolution powder neutron diffraction experiments by Gibbs et al.[28].

The zone-boundary mode  $K_3$  is an example of a soft mode as discussed in section 4.2.1. The soft mode is the vibration of  $Mn^{3+}$  resulting in tilting of the  $MnO_5$  trigonal bipyramids. When the mode freezes the tilting of the bipyramids with respect to the c-axis becomes permanent. This results in unequal lengths of the two Y-O apical bonds[28] which lead to an up-down-up-down-up displacement of Y in the yttrium layer. The tilting combined with the displacements of Y-atoms result in a non-centrosymmetric crystal with a net polarization, hence ferroelec-

<sup>1</sup>A vibrational mode is the continuous movement of atoms relative to each other[26].



tricity, as well as a tripling of the unit cell[29]. The hexagonal manganites are considered improper ferroelectrics. For an improper ferroelectric the primary order parameter is not polarization[30]. The mode giving polarization is not the one driving the transition, but rather a secondary effect of the tilting/rotation of the oxygen  $\text{MnO}_5$  trigonal bipyramids[31, 22]. Although these studies were performed on  $\text{YMnO}_3$  the same would be expected for the paraelectric/ferroelectric phase transition in  $\text{InMnO}_3$ .

The phase transition between the high-temperature paraelectric phase,  $P6_3/mmc$ , to the low-temperature ferroelectric phase  $P6_3cm$  is, as mentioned above, a second-order displacive transition[22]. This means it does not need to be an activation energy barrier present for the transition. However, the paraelectric/ferroelectric phase transition between  $P\bar{3}c1$  and  $P6_3cm$  shows a different behaviour. This is explained in section 4.4.

### 4.2.3 Polarization

The ferroelectric property is classified as spontaneous polarization that can easily switch direction by an electric field. Spontaneous polarization means that the material is polarized without an applied electric field. This is due to permanent displacements of atoms resulting in permanent dipoles. It is of interest to investigate how point defects affect the polarization of the ferroelectric  $P6_3cm$  phase. To be able to do that the term polarization has to be better explained.

Polarization of a material occurs when the centre of gravity of positive and negative charges do not coincide[24]. This results in a permanent dipole in the material. Polarization is closely connected to the dipole moment,  $\vec{d}$ , and is defined as the dipole moment divided by the unit volume. A simple way to calculate the polarization is by use of the point charge model, also known as the Clausius-Mosotti model, defined below[32]. The dipole moment is defined as the following:

$$\vec{d} = \sum_i q_i \vec{r}_i \quad (4.1)$$

where  $q$  is the elementary charge,  $i$  the sum over all atoms and  $\vec{r}_i$  the displacement of the atom from the non-polar state. In this project an artificial non-polar state is made for calculating the spontaneous polarization of  $P6_3cm$ . The polarization is calculated by dividing the

dipole moment,  $\vec{d}$ , on the volume of the unit cell,  $V$ :

$$\vec{P} = \frac{\vec{d}}{V} = \frac{1}{V} \sum_i q_i \vec{r}_i \quad (4.2)$$

It is important to note that the dipole moment is a vector quantity, hence the polarization is also defined as a vector. The polarization vector,  $\vec{P}$ , points from the negative to the positive surface. As can be seen from the point charge model the calculated value describes the difference in polarization from the non-polar state to the polar state. When polarization is measured experimentally, with for instance the Sawyer-Tower method[32], it is the change in polarization from one polarized state to another that is measured. This difference divided on two is the spontaneous polarization[33]. Polarization is therefore not stated as an absolute value, but rather a change.

The point charge model is a macroscopic model and not suitable for calculating the polarization in crystals, as for instance  $\text{InMnO}_3$ . In general the polarization consists of two main contributions, the electronic- and ionic polarization. The electronic polarization is a result of a non-centrosymmetric disposition of electrons around the nucleus. The ionic polarization comes from atomic displacements[34]. In the point charge model the total polarization is said to be a sum of the local charge contributions from displacements. Meaning, this model only considers the ionic polarization. However, for a crystal the electronic polarization has a periodic continuous contribution[33], and is therefore not negligible. To find the polarization for crystals the modern theory of polarization has to be used. This is a microscopic model on polarization. The theory includes a quantum approach and will be better understood after a brief introduction to density functional theory. The modern theory of polarization is therefore further explained in section 5.5.4.

### 4.3 Symmetry considerations for phase transitions

To better explain the nature behind different phase transitions a brief introduction to symmetry and group/subgroup relationship is presented. Symmetry considerations where translation symmetry is disregarded, meaning only one point is unchanged during the symmetry operation, are categorized as point groups. There exist 32 different point groups. The

point groups are again divided into seven subcategories: triclinic, monoclinic, orthorhombic, tetragonal, trigonal, hexagonal and cubic[35]. The point groups can be divided further into space groups. Space groups include the possibility of translations. A space group gives a full description of the symmetry of a crystal in space[13]. There exist a total of 230 space groups, each describing all symmetry elements of the crystals related to the given group. The relevant space groups combined with their respective point groups and systems are given in Table 4.1.

**Table 4.1:** Representation of space groups relevant for this project with their respective point groups, lattice systems and polarization[24, 35].

Space group	Crystal system	Point Group	Symmetry elements	Polar
$P6_3cm$	Hexagonal	$6mm$	12	Polar
$P6_3/mmc$	Hexagonal	$6/mmm$	24	Non-polar
$P\bar{3}c1$	Trigonal	$\bar{3}m$	12	Non-polar
$P3c1$	Trigonal	$3m$	6	Polar

### 4.3.1 Group/subgroup relationship

Point groups and space groups consist of a self-consistent<sup>2</sup> finite set of symmetry operation[13]. The group/subgroup relationship between space groups can be defined as the following:

*A group A consist of X different symmetry operations (symmetry elements). A group B consist of  $Y < X$  of the same symmetry operations as group A. From definition, B is a subgroup of A and A is called a supergroup. A subgroup has always lower symmetry than the supergroup.*

The group/subgroup relationships for the space groups presented in Table 4.1 are shown in Figure 4.2. The arrows shows the connection from a group to a subgroup.

<sup>2</sup>Self-consistent means not having parts or aspects which are in conflict or contradiction with each other[36].

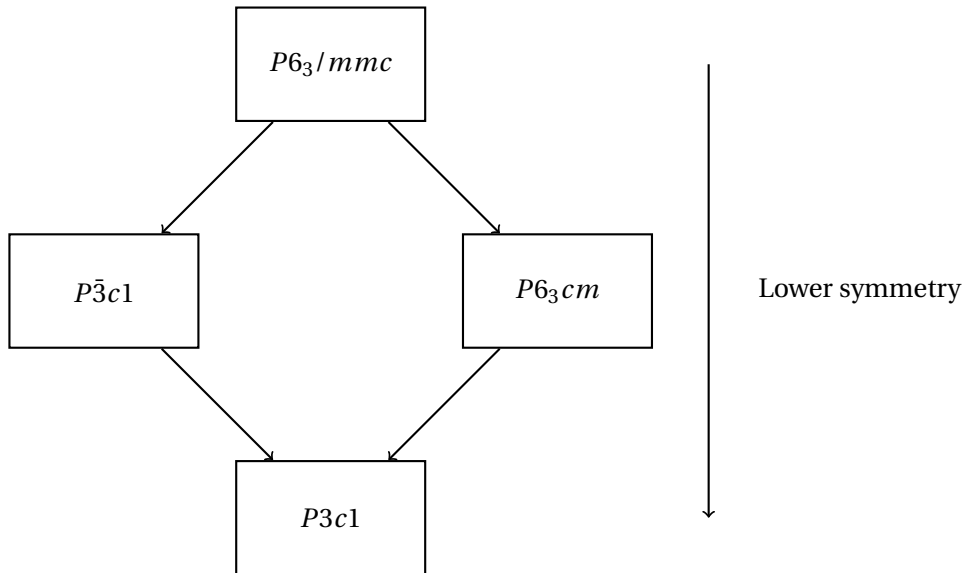


**Figure 4.2:** Representation of the relationship between the space groups  $P\bar{3}c1$ ,  $P6_3cm$  and  $P3c1$ .  $P3c1$  is a subgroup of  $P\bar{3}c1$  and  $P6_3cm$ .  $P\bar{3}c1$  and  $P6_3cm$  are subgroups of  $P6_3/mmc$ . The relationships are found with help from Bilbao Crystallographic Server[37]

### 4.3.2 Symmetry for $P\bar{3}c1$ , $P6_3cm$ and $P3c1$

In  $P6_3cm$  the  $MnO_5$ -trigonal bipyramids trimerize with a trimerization phase of  $n \cdot 60^\circ$ , where  $n$  is an integer[7]. Because of this the In-atoms are displaced up or down along the c-axis. This gives a polar structure and ferroelectricity. When transforming from  $P6_3cm$  to  $P3c1$  the sixfold symmetry axis is lost, but the inversion symmetry causing centrosymmetry is still absent[38]. This gives again a polar structure and ferroelectricity. When  $P3c1$  transform to  $P\bar{3}c1$  the  $MnO_5$ -trigonal bipyramids trimerize at intermediate angles. This results in inversion symmetry and no net polarization since the tiltings neutralize each other.

## 4.4 Possible transition paths for $InMnO_3$

For phase transitions between two structures that have a group/subgroup relationship the transition is a second-order transition, and the activation energy barrier is in theory zero. However, if two structures do not have this relationship an activation energy barrier should be present throughout the transition. As can be seen in Figure 4.2  $P\bar{3}c1$  and  $P6_3cm$  do not

have a group/subgroup relationship and consequently an activation energy barrier must be present for the phase transition between them. The interesting question is then in which direction the value of the activation energy barrier change when intrinsic point defects are introduced in the material.

To find out if intrinsic point defect increase or decrease the activation energy barrier between  $P\bar{3}c1$  and  $P6_3cm$ , the direct phase transition between these structures is investigated. This is done both for a stoichiometric cell and non-stoichiometric cells. If defects reduce/increase the activation energy barrier this might help explain the deviating properties for InMnO<sub>3</sub> found in literature.

Cano et al.[38] have proposed an alternative path for the transition between  $P\bar{3}c1$  to  $P6_3cm$ . Instead of a direct transition, as mentioned above, they suggest that the phase transition goes through an intermediate structure,  $P3c1$ . By observing Figure 4.2 it is noted that  $P\bar{3}c1$  and  $P3c1$ , and  $P6_3cm$  and  $P3c1$  have a group/subgroup relationship.

#### 4.4.1 Transitions in stoichiometric and non-stoichiometric cells

It is of interest to calculate the activation energy barrier between stoichiometric cells, meaning cells without defects. This can be used as a reference state. The following stoichiometric phase transition should be investigated:

- $P\bar{3}c1 \rightarrow P6_3cm$

When investigating the effect point defects have on the activation energy barrier it is chosen to do one calculation on each type of intrinsic defect. This means the following situations have to be considered:

1. Phase transition with an interstitial oxygen.
2. Phase transition with an oxygen vacancy.
3. Phase transition with an indium vacancy under oxidizing conditions.
4. Phase transition with an indium vacancy under middling reducing condition.

The defect positions giving the most stable structure for each of the above categories are used. This is done to reduce the overall calculation effort and still get enough useful information to discuss the hypothesis.

## Chapter 5

# Density functional theory

In this chapter the reader is given an overview of the principles behind density functional theory and how this can be developed into a computational method. The text will not explain the theory in detail, but aims to make the reader understand the basics behind the calculations done in this project. Most of the theory is taken from the book “Density Functional Theory - A practical Introduction” [39] and “Computational Materials Science - An Introduction” [40]. The reader is advised to take a look at these sources if a more thorough explanation of density functional theory is desired. An introduction to the simulation software Vienna Ab-initio Simulation Package (VASP) will be given in section 5.6.

## 5.1 The Schrödinger equation

The Schrödinger equation describes how the energy of quantum mechanical systems change with time. The first thing to do to when introducing DFT is to define the time-dependent Schrödinger equation[41]:

$$i\hbar \frac{\partial}{\partial t} \Psi(\vec{r}, t) = -\frac{\hbar^2}{2m} \nabla^2 \Psi(\vec{r}, t) + V(\vec{r}, t) \Psi(\vec{r}, t) \quad (5.1)$$

Due to too many degrees of freedom it is not possible to solve the Schrödinger equation. Therefore, to be able to implement this equation in a computational tool a few approximations must be applied. The first approximation is the Born-Oppenheimer approximation. Born and Oppenheimer stated that the atomic nuclei has a much larger mass compared to the individual electrons. The electrons will therefore be much more sensitive to changes in their surrounding than the nuclei[42, 43]. By taking this into account the problem can be divided into two subproblems:

1. Solve the equation that describes the electron motion when the atomic nuclei is at a fixed position. This means finding the lowest energy configuration for the electrons, the ground-state energy ( $E_0$ ).

2. Observe how the ground-state energy changes when the atoms are moved around.

The ground-state energy is not dependent on time and the problem can therefore be solved by the time-independent Schrödinger equation. This will further reduce the complexity of the problem. The Schrödinger equation that describes the time-independent situation where multiple electrons interact with multiple nuclei is given by[39]:

$$\left[ \underbrace{-\frac{\hbar^2}{2m} \sum_{i=1}^N \nabla_i^2}_{(1)} + \underbrace{\sum_{i=1}^N V(\vec{r}_i)}_{(2)} + \underbrace{\sum_{i=1}^N \sum_{j<i}^N U(\vec{r}_i, \vec{r}_j)}_{(3)} \right] \Psi = E\Psi \quad (5.2)$$

The symbol  $m$  stands for the electron mass,  $N$  for the number of electrons and  $E$  for the energy. The terms in the parentheses on the left side of the equation represents the Hamilton operator. The Hamilton operator describes the following:

1. Kinetic energy of each electron.
2. Interaction energy between electrons and the atomic nuclei.
3. Interaction energy between different electrons.

The wave function,  $\Psi = \Psi(\vec{r}_1, \dots, \vec{r}_N)$ , where  $N$  is the number of electrons, can be approximated to  $\Psi = \Psi_1(\vec{r})\Psi_2(\vec{r}), \dots, \Psi_N(\vec{r})$ , a product of individual electron wave functions. This product is called the Hartree-product and has shown to be important when solving the Schrödinger equation with DFT[39]. The most difficult term to solve is the term considering interactions between electrons. The individual electron wave functions,  $\Psi_i(\vec{r})$ , cannot be defined without taking into account the individual electron wave functions of all the other electrons in the system. This means that solving the Schrödinger equation is a many-body problem<sup>1</sup>. A material has an excessive number of electrons,  $N$ , that need to be summed over. This combined with the fact that solving the equation is a many-body problem makes it impossible to solve the Schrödinger equation analytically. Fortunately, DFT can help solve that problem.

<sup>1</sup>A many-body problem is a term used for problems where a large number of particles are coupled. To be able to solve the equation for one particle the equation for all the other particles have to be solved as well.



## 5.2 Density functional theory

The density functional theory is based on two mathematical theorems published by Kohn and Hohenberg in 1964[44], and later two set of equations derived by Kohn and Sham in 1965[45].

### 5.2.1 The Kohn-Hohenberg theorems

The first theorem published by Kohn and Hohenberg reads:

The ground-state energy from the Schrödinger equation is a unique functional<sup>2</sup> of the electron density[39]. *(Theorem 1 - Kohn and Hohenberg)*

In other words this theorem states that for every ground-state wave function it exists a ground-state electron density. Written in mathematical terms this can be expressed as[44]:

$$E[n(\vec{r})] = \int V(\vec{r})n(\vec{r})d\vec{r} + F[n(\vec{r})] \quad (5.3)$$

where  $V(\vec{r})$  is the external potential,  $F[n(\vec{r})]$  is the exchange functional and  $n(\vec{r})$  the electron density given as:

$$n(\vec{r}) = 2 \sum_i \Psi_i^*(\vec{r})\Psi_i(\vec{r}) \quad (5.4)$$

A fact that arises from this theorem is that the ground-state electron density determines all properties of the ground-state. Meaning, the Schrödinger equation can be solved by looking only at the electron density. This is beneficial since the electron density is a function of three spatial variables, compared to the electron wave function which is a function of  $3N$  variables. This will reduce the computational effort considerably.

The second theorem stated by Kohn and Hohenberg describes an important property for the functional mentioned in the first theorem:

The electron density that minimizes the energy of the overall functional is the true electron density corresponding to the full solution of the Schrödinger equation[39].

*(Theorem 2 - Kohn and Hohenberg)*

---

<sup>2</sup>A functional takes a function and defines a single number from the functional, compared to a function that takes a value of a variable and define a single number.

Written in mathematical terms this is given in equation 5.5, where  $n_0$  is the minimum electron density [44]:

$$E_0 = E[n_0(\vec{r})] \quad (5.5)$$

This means that the functional representing the relevant electron density can be found by varying the electron density until the energy from the functional is minimized. In DFT-calculations this is done by using approximate forms of the functional as described in detail later, see section 5.2.3.

## 5.2.2 The Kohn-Sham equations

Kohn and Sham developed a set of equations that are based on the theorems given by Hohenberg and Kohn[45]. These equations give an interpretation of the unknown exchange functional,  $F[n(\vec{r})]$ . They divided  $F[n(\vec{r})]$  into three parts given as[40]:

$$F[n(\vec{r})] = E_{kin}^{non} + E_H + E_{xc} \quad (5.6)$$

where  $E_{kin}^{non}$  is the non-interaction kinetic energy,  $E_H$  is the Hartree energy and  $E_{xc}$  is the exchange-correlation energy<sup>3</sup>.

Kohn and Sham presented a way to express each of these terms as a functional of the electron density. The first term is given as [40]:

$$E_{kin}^{non}[n(\vec{r})] = -\frac{1}{2} \sum_i^n \Psi_i^*(\vec{r}) \Delta^2 \Psi_i(\vec{r}) \quad (5.7)$$

where the argument later can be expressed in terms of electron density by using equation 5.4. The second term is given as [40]:

$$E_H[n(\vec{r})] = \frac{1}{2} \int \int \frac{n(\vec{r}) - n(\vec{r}')}{|\vec{r} - \vec{r}'|} d\vec{r} d\vec{r}' \quad (5.8)$$

The Hartree energy,  $E_H$ , comes from interactions between an electron at a distance  $\vec{r}$  from the nucleus and the mean electron density at  $\vec{r}'$  in a mean-field approximation[40]. The mean-field represents the average (mean) field generated by all other electrons.

<sup>3</sup> $E_{xc}$  represents all the interaction energies gathered into one term.

### 5.2.3 The exchange-correlation functional

The last term  $E_{xc}$  is a bit more tricky to define compared to the two others. At this time DFT does not give an absolute definition of the exchange-correlation energy.  $E_{xc}$  covers all quantum effects and cannot be expressed by physical terms for most systems, unlike  $E_H$  and  $E_{kin}^{non}$ . The only situation where the exchange-correlation functional can be derived exactly is for a uniform electron gas[39]. In this case the electron density is constant and the functional can be given as  $E_{xc}^{\text{electron gas}}$  and  $E_{xc}$  can be approximated to:

$$E_{xc} = E_{xc}^{\text{electron gas}}[n(\vec{r})] \quad (5.9)$$

The above equation gives the simplest approximation possible and is called the *local density approximation*, LDA. By using this approximation the Kohn-Sham equations can be completely defined and the Schrödinger equation solved. It is important to note that this is just an approximation and will therefore not solve the true Schrödinger equation. Other approximations have been developed over time to give more accurate descriptions of the exchange correlation functional. The *general gradient approximation*, GGA, takes into consideration both the local electron density and the local gradient in the electron density. For calculations performed in this project a sub-functional of GGA, PBEsol, is used. This functional, presented by Perdew et al. in 2008[46], is developed especially for solids.

### 5.2.4 Result of DFT

To sum up, density functional theory describes energy as a functional of the electron density to turn the unphysical wave functions into something physical and measurable. This makes it possible to find an approximation to the solution of the Schrödinger equation. In principle the Kohn-Sham equations have to be solved to find the electron density, and the electron density has to be known to solve the Kohn-Sham equations. This means an iterative process has to be performed to find the ground-state electron density. The process can be described in four steps[39]:

1. Define an initial electron density,  $n^*(\vec{r})$ , by guessing.

2. Solve the Kohn-Sham equations with  $n^*(\vec{r})$  to find the single-particle wave functions,  $\Psi_i(\vec{r})$ .
3. Find the electron density,  $n_{KS}(\vec{r})$ , by solving equation 5.4 with the value for  $\Psi_i(\vec{r})$  calculated in 2.
4. Compare  $n^*(\vec{r})$  with  $n_{KS}(\vec{r})$ . When these are equal the ground-state electron density is found. If not, start with  $n_{KS}(\vec{r})$  at step 2.

The next section will describe how VASP interpret the principles behind the density functional theory to give a computational tool that can describe properties of all materials.

## 5.3 From theory to calculations

Density functional theory provides a set of basic principles and equations that make it possible to find the ground-state energy and properties for different materials. To convert this information into something useful in the computational world a few concepts and approximations have to be defined.

### 5.3.1 From bulk to k-space

#### Supercell

A material exists of a high semi-finite number of atoms and it would be computational exhausting to include calculations for all these atoms. The first approximation is to reduce the bulk material to periodically duplicated supercells[40]. A supercell is several unit cells put together that efficiently describes the bulk material. It is also big enough to properly describe interactions inside the material. Calculations are done on a single supercell and then copied to all the other supercells to constitute an approximation to the bulk material.

#### Brillouin zone

For DFT calculations the main goal is to be able to calculate the bulk by looking at a small as possible piece of the material. The next step is to take advantage of how periodicity acts in reciprocal space. The Brillouin zone (BZ) is the primitive cell in reciprocal space. It possesses the characteristic that all points outside the first BZ are equivalent to a point inside the first

BZ due to the periodicity of the reciprocal lattice. In mathematical terms this can be written  $\vec{k}' = \vec{k} + \vec{G}$  where  $\vec{k}'$  is a wave vector outside the first BZ. Meaning two  $\vec{k}$ -vectors, wave vectors, that differ from each other by adding or subtracting  $n\vec{G}$  are equal. To solve the Kohn-Sham equations it is therefore only necessary to look at a single BZ. The first BZ can be reduced to the irreducible Brillouin zone (IBZ) by looking at symmetry from inversion and rotation operation. This will reduce the number of  $\vec{k}$ -points further.

### **k-point density**

Reciprocal space is the Fourier transform of real space. The characteristic that something large in real space becomes small in reciprocal space can therefore be used to reduce the calculation size for large cells. Even though any point in the IBZ represents a  $\vec{k}$ -point, giving an infinite number of  $\vec{k}$ -vectors, the properties of a material change smoothly. This means it is only necessary to sample a finite number of  $\vec{k}$ -points that will describe each region[40]. For a large cell fewer k-points are necessary than for a small cell, referring to the fact that a big area in real space is small in reciprocal space.

Mathematically this can be described and verified through Bloch's theorem, equation 5.10:

$$\Psi_{\vec{k}}(\vec{r}) = \exp(i\vec{k} \cdot \vec{r}) u_{\vec{k}}(\vec{r}) \quad (5.10)$$

where  $\vec{r}$  is the position vector in real space and  $u_{\vec{k}}$  is a function with the same periodicity as the supercell. The result of this theorem is that the Schrödinger equation can be solved for each value of  $\vec{k}$  independently, as stated earlier. From a computational point of view it will be a goal to use as few k-points as possible. Choosing this k-value is an important part of DFT-calculations. Therefore all systems should test their k-point-convergence before reliable calculations can be done.

The result of these last three topics is that the bulk material can be described only by calculating a finite number of k-points. The size of the calculations has been drastically reduced, and the computational efficiency is much higher.

### 5.3.2 Cut-off energy

The term  $u_k$  that appears in Bloch's theorem can be defined as the following according to its periodicity[39]:

$$u_{\vec{k}}(\vec{r}) = \sum_{\vec{G}} \exp[i\vec{G} \cdot \vec{r}] \quad (5.11)$$

By including equation 5.11 in Bloch's theorem, equation 5.10 becomes:

$$\Psi_k(\vec{r}) = \sum_{\vec{G}} \exp[i(\vec{G} + \vec{k})\vec{r}] \quad (5.12)$$

The problem with this expression is that solving the equation, even for only one k-point, requires that an infinite number of  $\vec{G}$  has to be taken into consideration. To solve this problem it is efficient to introduce an upper energy limit that confine which solutions that have to be evaluated. Solutions of high energies often represents unbound free electrons[40] that are not relevant for most material properties. As a consequence, solutions with lower energies are the most important for describing a material. The solution of the Schrödinger equation comes in terms of kinetic energy given as[39]:

$$E = \frac{\hbar^2}{2m} |\vec{k} + \vec{G}|^2 \quad (5.13)$$

Applying the cut-off energy gives the following equality:

$$E_{cut} = \frac{\hbar^2}{2m} G_{cut}^2 \quad (5.14)$$

Equation 5.12 will now sum up over a finite number of  $\vec{G}$ -vectors and the problem is again possible to solve. To reduce the computational effort it will be desirable to choose a small as possible cut-off energy. As well as for k-points, choosing the cut-off energy is an important step in applying DFT. A convergence test on the cut-off energy has to be done for all systems before reliable calculations can be performed.

### 5.3.3 Pseudopotentials

The last concept to be introduced is the use of pseudopotentials. To reduce the number of electrons that have to be calculated the nucleus and core electrons are frozen, thus they are

kept constant. In general this can be done because the valence electrons dominate chemical bonding and most physical properties. This approximation will then reduce the complexity of solving the Schrödinger equation, as well as it will lead to an easier computational description of the valence wave functions. A pseudopotential replaces the electron density for the core electrons with a constant density developed to match various physical properties[39]. A pseudopotential is given for an isolated atom of one element and by combining the pseudopotential for different atoms calculations on a compound can be done.

Different pseudopotentials for the same atom will include different numbers of valence electrons. In general the more valence electrons included the higher cut-off energy is necessary. Potentials that require high cut-off energy are often called hard potentials, while potentials that require a low cut-off energy are often called soft potentials. It is obvious that soft potentials are more computational efficient than hard potentials, but they will also give a less accurate solution.

## 5.4 Numerical optimization

As mentioned, it is not possible to find the exact solution of the Schrödinger equation. DFT only provides a numerical approach to the solution by use of different optimization methods[39]. As a consequence, two calculations with the exact same parameters will not result in the exact same answer. When using numerical methods two criteria have to be set to decide when the calculation has converged. For calculations on three-dimensional structures the energy and force criteria are important.

### 5.4.1 Energy criterion

The energy criterion decides when electronic convergence is reached. The energy is calculated by solving the Schrödinger equation as explained above. When the difference between the energy of two iterations becomes smaller than the stated energy criterion the calculation stops and the atoms relax into the new positions. The energy criterion is set close to zero. A smaller value gives a more accurate solution, but also requires more computational effort.

### 5.4.2 Force criterion

The force on an atom  $i$  was defined by Feynman in 1939 as[47]:

$$\vec{F}_i = \frac{\delta E(\vec{r})}{\delta \vec{r}_i} \quad (5.15)$$

where  $\vec{r}_i$  is the position of the  $i$ th atom and  $E(\vec{r})$  is the average energy of the system. In the ground-state the force on all atoms should be zero. The force criterion decides when ionic convergence is reach, meaning when all the forces on the atoms are below a stated value. As for the energy criterion this value is set close to zero, and the smaller number the more accurate solution. However, a smaller value also means more computational effort.

## 5.5 Types of DFT-calculations

DFT can be used to calculate different properties and give valuable information about the material. A brief overview of different areas of application of DFT is given below.

### 5.5.1 Calculation of minimum energy of a structure

The most general use of DFT is to calculate the total energy of a set of atoms prescribed at specific positions in space[39]. By using numerical optimization and the iteration scheme given in section 5.2.4 the Kohn-Sham equations can be solved by approximation, and the ground-state energy for any structure calculated. Calculating the minimum energy of a structure is in fact done every time a DFT-calculation is performed. This type of calculation calculates the ground-state energy when every atom position in the supercell is fixed. The only criterion that has to be obtained is the energy criterion, see section 5.4.1. Static calculation is another name for this type.

Another use of DFT is to optimize structure parameters and find a geometry that minimizes the ground-state energy. This is done by calculating the force on each atom after electronic convergence is reached, meaning the energy criterion is fulfilled. The calculation adjusts the atomic positions in accordance with the forces calculated, and starts over again. This loop continues until the differences in the calculated force are less than the force criterion when



comparing two relaxations. Ionic convergence is reached.

Two different types of ionic relaxations are performed in this project. Both explained below:

**Fixed volume** - The cell is relaxed until ionic and electronic convergence are reached. The atom positions are allowed to change, while the cell shape (lattice parameters) and cell volume are kept constant. In these calculations it is assumed that the defect concentration is low enough (close to the dilute limit) so it does not affect the volume of the cell.

**Relaxed volume** - The cell is relaxed until ionic and electronic convergence are reached. The atom positions, cell shape (lattice parameters) and cell volume are allowed to change. In these calculations it is assumed that the defect concentration is of an order of magnitude so it affect the volume. Chemical expansion therefore needs to be taken into account.

## 5.5.2 Density of states calculations

Density of states, from here on called DOS, is one of the primary quantities to describe the electronic state of a material[39]. The DOS is given as:

$$\rho(E)dE = \text{number of electron states with energies in the interval } E \text{ to } E + dE$$

In section 5.2.1 it was stated that idea behind DFT-calculations is to express the ground state energy by means of the electron density. The electron density is given in the form  $\exp(i\vec{k} \cdot \vec{r})$ . The energy of an electron associated with plane waves have the energy  $E = (\hbar\vec{k})^2/2m$ . That means when a DFT-calculation is performed the electronic density of states can be found by integrating the resulting electron density in  $k$ -space[39]. Since the electronic DOS is found by integrating in  $k$ -space a high  $k$ -point density is required for a detailed electronic DOS.

Local density of states, LDOS, is defined as the number of electronic states at a specific energy weighted by the fraction of the total electron density for those states that appears in a specific volume around a nuclei[39]. LDOS shows the density of state of each atom and its respective orbitals. This is done by assuming a spherical volume and using the radius of each atom to classify what parts of the total DOS belong to each atom and orbital.

### 5.5.3 Calculations of activation energies for transitions

In theoretical chemistry and condensed matter physics it is often of interest to identify a lowest energy path for an arrangement of atoms from one stable configuration to another. This kind of path is in literature referred to as "the minimum energy path" (MEP)[48]. The saddle point along the MEP gives the potential energy maximum, also known as the activation energy barrier for the transition. It exists several methods for finding the MEP. The climbing image nudged elastic band method is the method used in this project. This method is described in further detail below.

#### Plain elastic band method

The plain elastic band method is used to find the MEP. It is a chain-of-states method. A chain-of-state method consists of several states, from here on called images, that are connected to yield a path. The objective function<sup>4</sup> is given for the plain elastic band method as[39]:

$$M^{PEB}(\vec{r}_1, \dots, \vec{r}_P) = \sum_{i=1}^{P-1} E(\vec{r}_i) + \sum_{i=1}^P \frac{k}{2} (\vec{r}_i - \vec{r}_{i-1})^2 \quad (5.16)$$

where  $\vec{r}_i$  is the position of the images,  $P$  the number of images,  $k$  the spring constant that connects adjacent images and  $E(\vec{r}_i)$  the total energy of the  $i$ th image.  $R_0$  and  $R_N$  represent energy minimized start and end points, thus the states where the activation energy barrier should be found. The MEP is found by minimizing the object function given in 5.16 with respect to the intermediate images while keeping the start and end points constant. However, the plain elastic band method has two problems that often result in incorrect MEPs. Both problems connect to the spring constant  $k$ . If the spring constant between the images are too low the images tend to slide down the energy landscape away from the MEP[39]. If the spring constant is too high the calculated MEP cuts the corner of the real MEP, thus overestimating the activation energy for the transition.

---

<sup>4</sup>An objective function is a function which goal is to find a maximum or minimum of the function by using nonlinear programming techniques.

### Nudged elastic band method

The nudged elastic band (NEB) method is derived from the plain elastic band method and designed to solve the problems regarding the spring constant. With DFT the force on each image can be calculated:

$$\vec{F}_i = \Delta E(\vec{r}_i) \quad (5.17)$$

The direction of the path can be estimated as a unit vector,  $\hat{t}_i$ , pointing along the line between two adjacent images[39]. Mathematically, this is expressed as:  $\hat{t}_i = \vec{r}_{i+1} - \vec{r}_{i-1}$ . An image will be at the MEP if all the forces acting on the image, except the force along the direction of the path, are zero. Thus, the following equation must be satisfied:

$$\vec{F}_i^\perp = \vec{F}_i - (\vec{F}_i \cdot \hat{t}_i) \hat{t}_i = 0 \quad (5.18)$$

To adjust the images they can be moved "downhill" along the direction of  $\vec{F}_i^\perp$ . To include the harmonic springs between the images the spring constant has to be added to the expression. The updated downhill direction then becomes:

$$\vec{F}_{i,update} = \vec{F}_i^\perp + \vec{F}_{i,spring} = \vec{F}_i^\perp + k(|\vec{r}_{i+1} - \vec{r}_i| - |\vec{r}_i - \vec{r}_{i-1}|) \quad (5.19)$$

The nudged elastic band method includes one more observation; The only forces of interest defined by the elastic spring are those that point along the direction of the MEP. It is desired that the spring forces only act to keep the images evenly spread out along the images, and not pull the images away from the MEP[39]. This is solved by defining:

$$\vec{F}_{i,spring}^\parallel = (\vec{F}_{i,spring} \cdot \hat{t}_i) \hat{t}_i \quad (5.20)$$

and updating the images with respect to this:

$$\vec{F}_{i,update} = \vec{F}_i^\perp + \vec{F}_{i,spring}^\parallel \quad (5.21)$$

The calculation has converged when  $\vec{F}_{i,update}$  is zero for all images. The images will then lay on the MEP and the energy barrier for a transition can be found by analyzing the minimum energy for the different images.

### Climbing image nudged elastic band method

The climbing image nudged elastic band method (CI-NEB) is a modification of the nudged elastic band method for finding minimum energy paths. The method was developed by Henkelman et al.[49]. In the CI-NEB a rigorous convergence to a saddle point is obtained. This is done without losing information about the shape of the NEB, or causing added computational effort. The method works in the following way. After a few iterations the image with the highest energy is identified. This image is from now on called  $i_{max}$ . The force on  $i_{max}$  is defined independently of the other images, meaning that the maximum energy image is not affected by the spring forces[49]. The force on  $i_{max}$  is the full force along the tangent of the elastic band. This force is inverted such that the image tries to maximize its energy along the elastic band and minimize it in all other directions. The image will climb up along the elastic band and when it has converged the image will be at the exact saddle point. Hence,  $i_{max}$  is the climbing image. Since  $i_{max}$  is not affected by the other images along the elastic band the distance between  $i_{max}$  and the two neighboring images might not be equal.

### 5.5.4 Polarization - Berry-Phase calculations

The modern theory of polarization was presented by King-Smith and Vanderbilt in 1993[50]. This method is often called the "Berry-Phase theory of polarization" since the polarization is expressed in terms of a quantum phase known as the Berry phase[33]. The theory will not be explained in detail here, only a brief introduction is given. The reader is advised to take a look at the following sources for a better view: [50], [33] and [51].

The point charge model looks at each displacement from the non-polar state as a localized dipole, see section 4.2.3. For a crystal this is not possible since the electron charge density is continuous[51]. As mentioned in section 4.2.3 both the ionic and electronic contribution to polarization have to be taken into account. The ionic contribution represents the point charge ions and can be expressed through the point charge model in equation 4.2. The electronic contribution has to be explained in terms of quantum mechanics with the help of Wannier functions[32]. The Wannier function in a unit cell  $\vec{R}$  associated with band  $n$  is defined as:

$$w_n(\vec{r} - \vec{R}) = \frac{V}{2\pi^3} \int_{BZ} d^3\vec{k} e^{-i\vec{k}\vec{R}} \Psi_{n\vec{k}}(\vec{r}) \quad (5.22)$$

where  $V$  is the unit cell volume,  $\Psi$  the Bloch functions and the integral is over the Brillouin zone. The Bloch function, equation 5.10, is inserted and gives the following:

$$w_n(\vec{r} - \vec{R}) = \frac{V}{2\pi^3} \int_{BZ} d^3\vec{k} e^{-i\vec{k}(\vec{r}-\vec{R})} u_{n\vec{k}}(\vec{r}) \quad (5.23)$$

Unlike the Bloch functions the Wannier functions are localized. The Wannier functions can therefore be used to express the electronic charges separately. The centre of the electronic charge is for ferroelectric materials not the same as for point charges. The average position of the electrons in a Wannier function is called the Wannier centre,  $\vec{r}_n$ . To simplify, all the electrons are treated as sitting at that point[32]. The polarization is given as the sum over the contribution from the point charges plus the sum over the electronic charges centred at the Wannier centres of each occupied Wannier function  $n$ [32]. Wave functions, with the approximations from Kohn-Sham, are a direct output of electronic relaxation calculations. This information can therefore be extracted from an electronic relaxation DFT calculation, and be used to calculate the polarization.

### 5.5.5 Limitations of DFT

It is important to be aware that practical DFT calculations are not exact solutions of the Schrödinger equation. Since the exchange-correlation functional is not known exactly the solutions calculated are only approximations of the true solutions. To defend DFT, these assumptions are often good approximations if the user is aware of the limitations of DFT. In the following section some of the most important limitations are addressed[39]:

- Calculations of **electronic excited states** are often inaccurate because the theorems developed by Kohn and Hohenberg only apply to the electron ground-state energy.
- DFT often underestimate the **band gap** for transition metal oxides with unoccupied d-orbitals. This can be solved by applying a potential,  $U$ , to best describe the experimental band gap.
- When using the LDA or GGA functional DFT does not take into account the weak **van der Waals attractions** that exist between molecules and atoms.
- The LDA functional, especially, has a tendency to **overbind**. That means the lattice parameters are typically underestimated while properties as cohesive energies and elastic

moduli are overestimated. The GGA functional tends to **underbind**. The lattice parameters are often overestimated and the cohesive energies underestimated. The PBEsol functional[46] is made for solids and is quite accurate both with respect to lattice parameters and cohesive energies.

## 5.6 Vienna Ab-initio Simulation Package (VASP)

The basis of DFT is presented, and necessary approximations and computational approaches have been explained. The next step is to explain the tool that combines this in a simulating software, VASP. In this project the features of VASP are only described briefly and the reader is advised to read the VASP manual[52] if a more thorough introduction is desired.

### 5.6.1 Features

VASP is a simulating tool that calculates the ground-state properties by doing electronic and ionic relaxations using the Kohn-Sham equations, a plane wave basis set and pseudopotentials. The relaxations are done numerically by use of a self-consistent cycle. The procedure VASP follows can be described by the following four steps[40]:

1. Choose a pseudopotential and an exchange-correlation functional. Guess a trial electron density.
2. Calculate all the energy terms in the Schrödinger equation.
3. Solve the Kohn-Sham equations by iteration.
4. Generate a new electron density from the calculated orbitals and start over.

For a static calculation VASP seek electronic convergence defined by the energy criterion to find the ground-state energy, see section 5.4.1. When electronic convergence is reached VASP print out the required information from the calculations into output-files. If a fixed relaxation is performed VASP calculate the force on the atoms when electronic convergence is reached. The atoms are moved into new position while the cell shape and volume are held constant. The calculations then start over. This continues until the force criterion is reached. For calculation allowed relaxation of volume and cell shape the same procedure is used, except atom positions, lattice parameters and volume are changed between each ionic step. To speed

up calculations it would sometimes be convenient to use symmetry-constrained relaxations, called selective dynamics. With selective dynamics the user can specify which atoms that are allowed to move and which are confined to a specific position.

### 5.6.2 Input-files

To be able to run a simulation in VASP four input-files are required. Appendix A gives a more detailed description of these files.

**INCAR** The INCAR-file gives important parameters/tags that classify how a calculation should be performed. This regards both accuracy and type of relaxation, as well as spin parameters. For the calculations in this project the following tags are of special importance:

- ENCUT: Defines the cut-off energy.
- EDIFF: Defines the accuracy required by the electronic steps, energy criterion.
- EDIFFG: Defines the accuracy required by the ionic steps, force criterion.
- LDAUU: Defines the Coulomb-correction.
- MAGMOM: Defines spin states on atoms in the cell.
- ISIF: Defines type of relaxation by specifying degrees of freedom during one ionic relaxation.
- NSW: Defines the maximum number of ionic steps.

**KPOINTS** The KPOINTS-file defines the k-point density for the calculations and is given in terms of number of k-points that should be used in each direction. For a hexagonal cell the k-mesh is given as  $axaxc$ , where  $a$  refers to number of k-points along the  $a$  lattice parameter and  $c$  to the number of k-points along the  $c$  lattice parameter.

**POTCAR** The POTCAR-file gives information about the pseudopotential used for each atom in the calculations.

**POSCAR** The POSCAR-file gives the position of each atom and length of each lattice vector in the cell (unit cell or supercell).





## Chapter 6

# Computational procedure

The following section presents computational details for the calculations. VASP version 5.3.3 were used on the calculations to find the ground-state energy for non-stoichiometric  $\text{InMnO}_3$ . VASP version 5.3.5 were used when doing calculations on phase transitions and polarization. The exchange-correlation functional used was PBEsol[39], a functional especially developed for solids. All convergence testing and parameter fitting were done on a 30 atoms cell.

## 6.1 Convergence testing

When performing DFT calculations the goal is to keep the computational effort as low as possible, while still producing valuable results. One way to reduce the computational effort is to test which values for different parameters gives convergence of the solution. The solution is given as a complicated set of mathematical equations[39]. Because of this, several numerical approximations have to be used to calculate the ground-state energy. To assure that the solutions calculated with DFT are accurate approximations of the true solution it is important to use parameters that converge. When the parameters used are made stricter the solution becomes more accurate, but the calculation effort increase. Convergence is reached when the change in energy is minimal when making the criteria/parameters stricter. Before performing calculations on a supercell, see section 6.3, several parameters were tested to find the least strict choice that still gave convergence.

### 6.1.1 K-point and cut-off testing

Convergence testing for k-point density and cut-off energy were done in a previous project[1]. Testing on both the  $P\bar{3}c1$ - and  $P6_3cm$ -structure were performed. For convergence testing on k-point density and cut-off energy a perfect 30 atoms unit cell were used. A summary of the

chosen parameters for further calculations are given in Table 6.1. A full overview of the k-point and cut-off testing is given in Appendix B.1.

**Table 6.1:** Summary of chosen values for k-point density and cut-off energy for calculations on  $P\bar{3}c1$  and  $P6_3cm$  for  $\text{InMnO}_3$ . Calculations were performed on a 30 atoms cell.

Parameter	Value
K-point density	4x4x2
Cut-off energy	550eV

### 6.1.2 Force testing

The force criterion that gives convergence has to be found. The meaning and use of the force criterion were discussed in section 5.4.2. Convergence of the force criterion has been tested for both phases,  $P\bar{3}c1$  and  $P6_3cm$ , for  $\text{InMnO}_3$ . Convergence testing on forces were performed on a stoichiometric unit cell and a unit cell with an interstitial oxygen. The most stable interstitial oxygen positions for  $P\bar{3}c1$  and  $P6_3cm$  from calculations done in previous work were used, see Appendix C.2. This was done to investigate the importance of the force criterion on calculations with and without point defects. Calculations were done for the following force criteria: -0.1 eV, -0.05 eV, -0.04 eV, -0.03 eV, -0.02 eV, -0.01 eV, -0.005 eV and -0.001 eV. The calculation details for force testing are given in Table 6.2. The interstitial oxygen positions used are given in Table 6.3 for  $P\bar{3}c1$  and  $P6_3cm$ .

**Table 6.2:** Calculation details for test of convergence on the force criterion. All calculations done with a 30 atoms cell.

	Relaxation	ENCUT [eV]	EDIFF [eV]	EDIFFG [eV]	K-mesh
Force	Constant volume	550	10e-6	Varying	4x4x2

When analyzing the trend in Figure 6.1, 6.2 and 6.3 a convergence pattern is observed. This reflects both testing for  $P\bar{3}c1$ ,  $P6_3cm$  and the energy difference between the two structures. For a non-stoichiometric cell with an interstitial oxygen a convergence pattern is to be found for the  $P6_3cm$  phase, but not for  $P\bar{3}c1$ . The jumping of the ground-state energy for  $P\bar{3}c1$  mount back to unpublished work performed by ph.D student Sandra Helen Skjærvø showing

**Table 6.3:** Interstitial oxygen positions for force testing on the  $P\bar{3}c1$ - and  $P6_3cm$ -structure of  $\text{InMnO}_3$ . The positions are given as fractional coordinates.

Structure	x	y	z
$P\bar{3}c1$	1/3	1/3	3/4
$P6_3cm$	1/3	1/3	0

that three positions for the interstitial oxygen gives a minimum. The oscillation between energies for low force criteria is therefore most likely related to the interstitial oxygen relaxing into different minimums. Because of this the conclusion regarding choice of force criteria is based on the stoichiometric data. In further calculations on defects a force criterion on -0.05 eV is used. It is chosen after evaluating the impact of a stricter force criterion on the accuracy versus the increased computational effort. Since the energy differences obtained by using a stricter force criterion are not much smaller (only an improvement in the range of 1-2 meV) it was concluded that for use in this project -0.05 eV was a sufficient criteria.

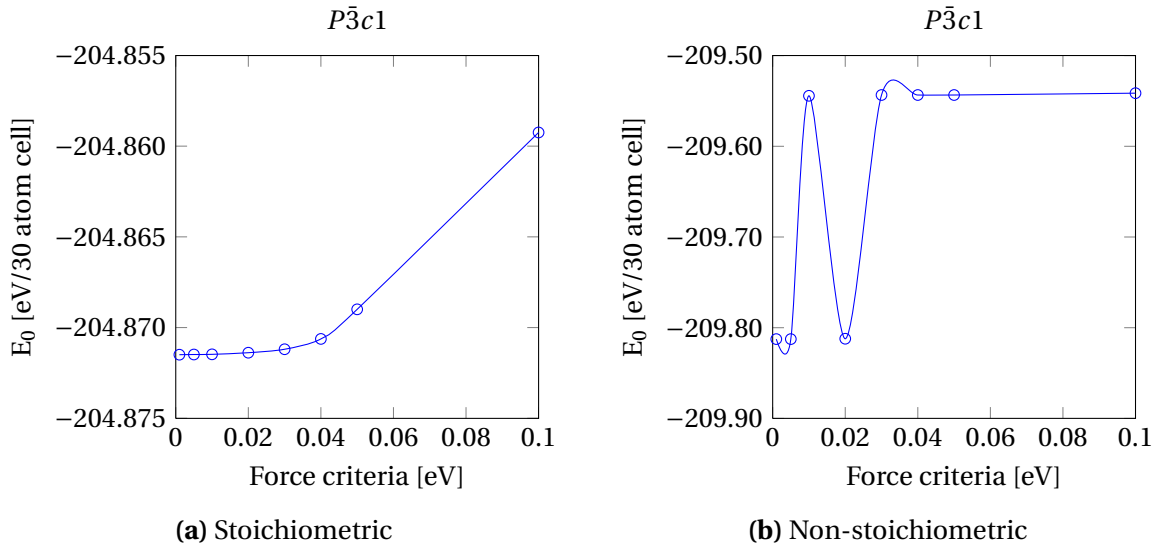


**Figure 6.1:** Convergence of force criterion for the  $P\bar{3}c1$ -structure for a stoichiometric cell and a non-stoichiometric cell with an interstitial oxygen. The interstitial oxygen positions for  $P\bar{3}c1$  and  $P6_3cm$  are given in Table 6.3. All calculations were performed with PBEsol and variables as given in Table 6.2.

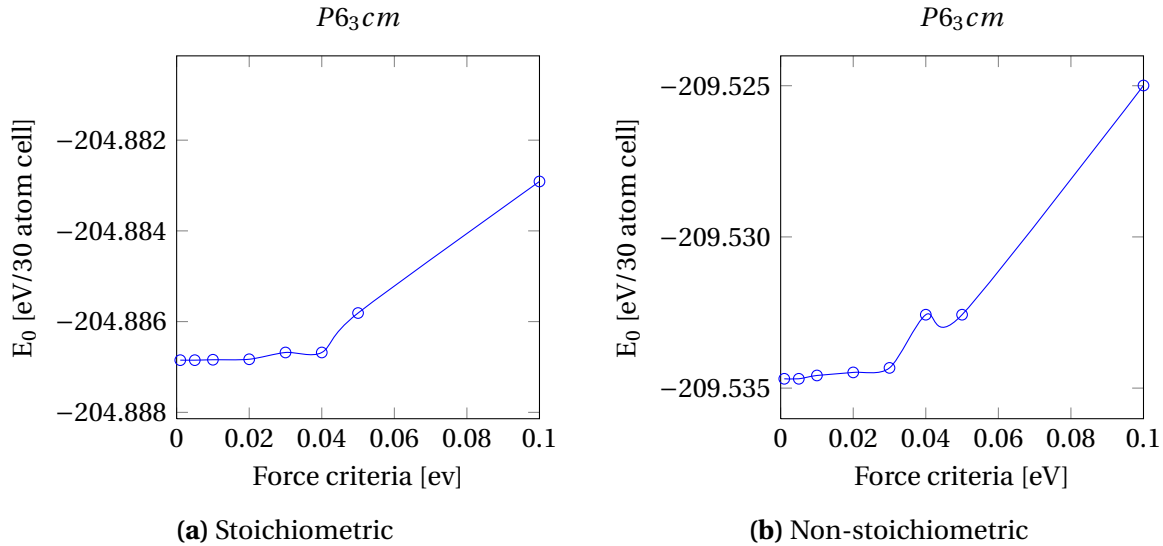


**Figure 6.2:** Convergence of force criterion for the  $P6_3cm$ -structure for a stoichiometric cell and a non-stoichiometric cell with an interstitial oxygen. Interstitial oxygen positions are given in Table 6.3. All calculations were performed with PBEsol and variables as given in Table 6.2.

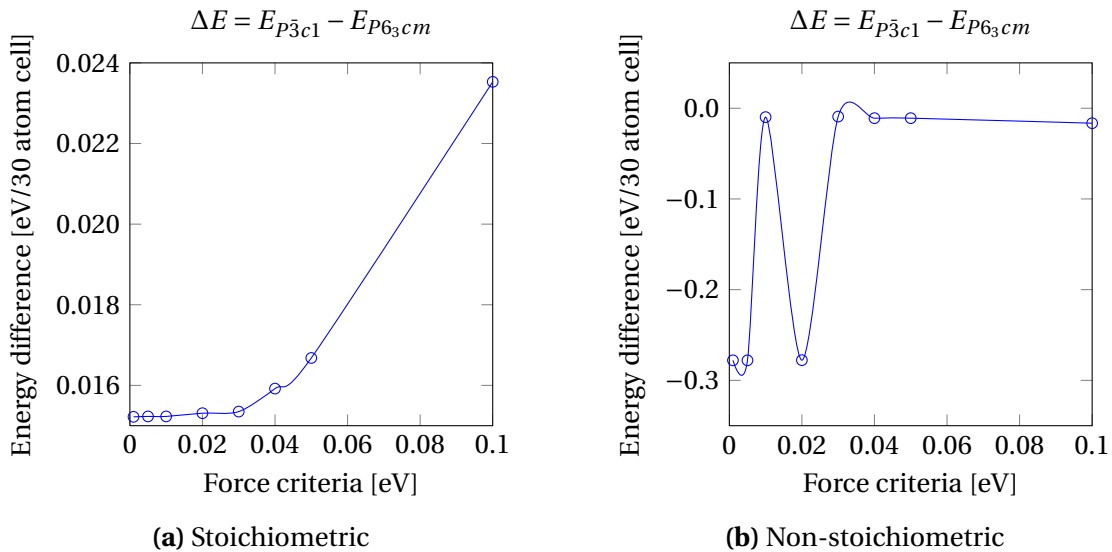


**Figure 6.3:** The energy difference between  $P\bar{3}c1$  and  $P6_3cm$  for the convergence of the force criterion for a stoichiometric cell and a non-stoichiometric cell with an interstitial oxygen. Interstitial oxygen positions are given in Table 6.3. All calculations were performed with PBEsol and variables as given in Table 6.2.

## 6.2 Hubbard U and pseudopotentials

In previous work with DFT on  $\text{InMnO}_3$  testing on suitable choices for Hubbard U and pseudopotentials were tested. Results from all the testing as well as arguments for the chosen parameters are to be found in Appendix B.2. These parameters are used for further calculations in this project. A summary is given in Table 6.4.

**Table 6.4:** Summary of chosen parameters for Hubbard U and pseudopotentials. Detailed description and results given in Appendix B.2.

Parameter	Value/type
Hubbard U	5 eV
Pseudopotentials	In_d, Mn_sv, O

## 6.3 The supercell approach

To give a more realistic description of how a defect affects the structure a supercell was used to minimize the defect-defect interactions, see Section 6.3. Putting together single unit cells makes a supercell. The unit cells used to make the supercell for each structure,  $P\bar{3}c1$  and  $P6_3cm$ , were fully relaxed with respect to atomic positions and volume. In this case it was desired to use a isotropic cell and the supercell was constructed by increasing with another unit cell in x- and y-direction, see Figure 6.4. The result is a supercell with double length in x- and y-direction and same length in z-direction.

When expanding the unit cell into a supercell the k-mesh can be changed. As mentioned in Section 5.3.1 a larger cell requires a less dense k-mesh. The required k-mesh for a single unit cell was  $4 \times 4 \times 2$ , as shown in Figure B.1. Since the supercell leads to a doubling in x- and y-direction it is safe to reduce the k-point density in these directions by dividing by two. The length of the c-axis was not changed when making the supercell and this value is therefore kept constant. The k-mesh used for the supercell calculations was then  $2 \times 2 \times 2$ .

The supercells used in this project were made from single unitcells with the  $P\bar{3}c1$  and  $P6_3cm$  structure. The unit cells were first relaxed w.r.t. atom positions, lattice parameters and vol-

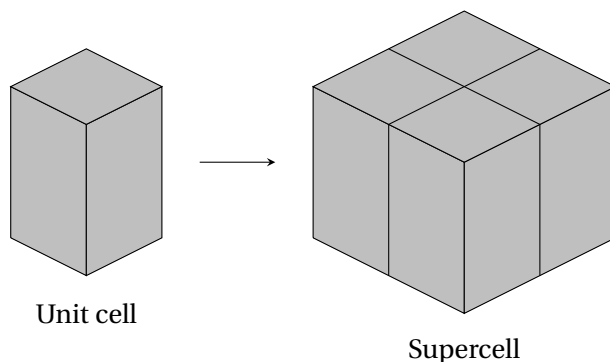


**Figure 6.4:** Schematic representation of the expansion from a single unit cell to a 2x2x1 supercell.

ume with an energy criterion of  $10^{-6}$  eV and force criterion of -0.01 eV. To be able to achieve convergence for supercells with defects the force criterion was adjusted to -0.05 eV.

## 6.4 Ground-state energy calculations

To find the ground-state energy for supercells with different defects the parameters discussed above were used. See also a summary in Table 6.5. Removing an atom from a supercell is significant change in the structure. The relaxation of the structures has proved to be difficult. Therefore the conjugate gradient algorithm for optimization of ions between each ionic step is used. This algorithm is recommended in the VASP tutorial for difficult relaxations[52].

## 6.5 Climbing image nudged elastic band calculations

The climbing image nudged elastic band (CI-NEB) approach was used to calculate the activation energy barrier for transitions between  $P\bar{3}c1$  and  $P6_3cm$ . This is a method developed by Henkelman et al.[49] at the University of Austin. The method is described in more detail in section 5.5.3. CI-NEB calculations were done by making intermediate images between already relaxed initial and end states. The images were made by utilizing a script, *nebmake.pl*, from a script-package called VTST-tools the Henkelman group at the University of Austin[53].

Parameters used for calculations on phase transitions were chosen to be the same as for re-

laxation to find the ground-state energy for defects. This was done to give a better basis for comparison. To be sure the force criterion of -0.05 eV was sufficient to reach convergence also for CI-NEB calculations one control calculation was performed where the criterion was increased to -0.01 eV. This calculation reproduced the same results and -0.05 eV can therefore be used with confidence.

Another point to note is that a different optimization algorithm was used for CI-NEB compared to ground-state energy calculations. This is because the changes in the atom positions for a CI-NEB method are very small, and it is therefore expected that the new structures that shall be relaxed are close to the local minimum. The VASP tutorial then recommends the quasi-Newton algorithm for relaxations[52].

## 6.6 Berry-Phase calculations

For Berry-Phase calculations only static calculations are done where the atom positions, lattice parameters and volume are kept constant. Parameters used to calculate the polarization were chosen to be the same as for relaxation to find the ground-state energy for defects. Berry-Phase calculations were done by utilizing the already relaxed structure of the polar  $P6_3cm$  phase for a stoichiometric and different non-stoichiometric supercells. A centrosymmetric, non-polar, reference structure and intermediate structures between the polar and non-polar state were made. The intermediate structures were made by utilizing a script, *posinterp.pl*, from a script-package called VTST-tools by the Henkelman group at the University of Austin[53].

## 6.7 Summary of parameters

Table 6.5 gives a brief overview of the parameters used for the different types of calculations performed in this project. A description of the parameters were presented in section 5.6.2.

**Table 6.5:** A summary of the chosen parameters for the DFT-calculations performed in this project for 120 atom supercells.

<b>Category</b>	<b>Defects, phase transitions and polarization</b>	<b>Density of states</b>
<i>Convergence criteria</i>		
PREC	Normal	High
ENCUT [eV]	550	550
EDIFFG [eV]	-0.05	-0.05
EDIFF [eV]	1E-08	1E-08
<i>K-mesh</i>		
Type	Gamma	Gamma
Value	2x2x2	4x4x4
<i>Pseudopotentials</i>		
Indium	PAW_PBE In_d 06Sep2000	PAW_PBE In_d 06Sep2000
Manganese	Mn_sv 23Jul2007	Mn_sv 23Jul2007
Oxygen	PAW_PBE O 08Apr2002	PAW_PBE O 08Apr2002



## Chapter 7

# Results

The following section presents results from DFT-calculations done in this project. All calculations were performed by using the modified GGA exchange-correlation functional, PBEsol[46]. As mentioned, PBEsol is an exchange-correlations functional especially developed for calculations on solids.

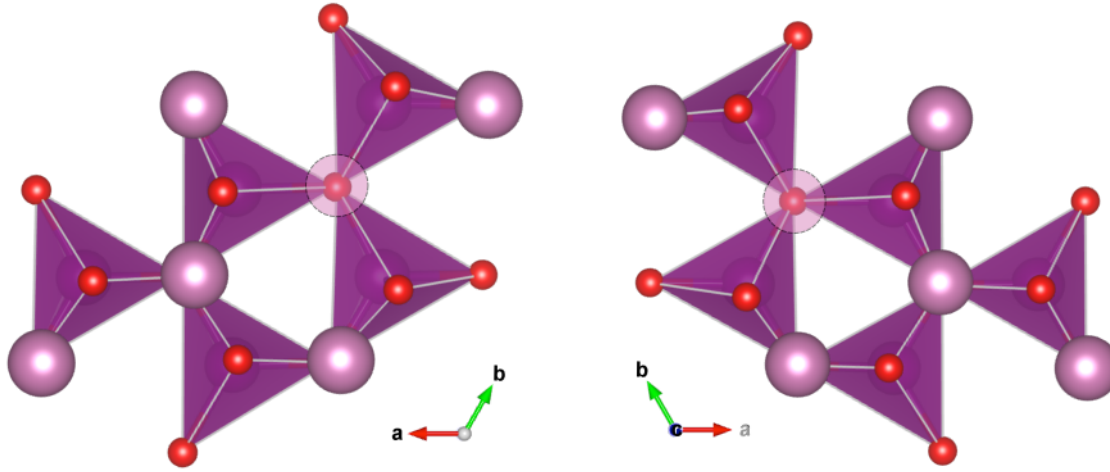
### 7.1 In-vacancies

The calculations were done both with fixed and relaxed volume, see explanation in section 5.5.1 for the difference between these two. The calculations were done with a 2x2x1 supercell with one In-vacancy and one In-O-vacancy pair respectively. The formula for the different cases then becomes:

- Oxidizing conditions:  $\text{In}_{0.958}\text{MnO}_3$
- Middling reducing conditions:  $\text{In}_{0.958}\text{MnO}_{2.986}$

#### 7.1.1 Oxidizing conditions - Only In-vacancy

Table 7.1 and Table 7.2 list the calculated values for the ground-state energy and volume for the different positions of In-vacancies. Figure 7.2 shows a barplot of the calculated ground-state energy and volume. The supercell was created from a unit cell that was first allowed to fully relax its atom positions, lattice parameters and volume, see section 6.3. Figure 7.3 shows the density of states and Figure 7.1 the structure after relaxation for the most stable configuration in  $P\bar{3}c1$  and  $P6_3cm$ .



(a) Relaxed structure of  $P\bar{3}c1$  with an indium vacancy at the In1 position seen along the c-axis. The calculation was done with fixed volume. The diffuse atom is the In-vacancy.

(b) Relaxed structure of  $P6_3cm$  with an indium vacancy at the In2 position seen along the c-axis. The calculation was done with fixed volume. The diffuse atom is the In-vacancy.

**Figure 7.1:** Only In vacancy.

**Table 7.1:** Calculated ground-state energy for a 120 atom supercell with an In-vacancy for  $P\bar{3}c1$  and  $P6_3cm$ . Calculations were done for the different In-vacancy positions given in Table 3.1. Both fixed volume and relaxed volume calculations were performed.

Structure	In-pos.	$E_0$ [eV/120 atom cell] w/ fixed volume	$E_0$ [eV/120 atom cell] w/ relaxed volume
$P\bar{3}c1$	In1	-809.10070	-809.18887
	In2	-809.09702	-809.15608
$P6_3cm$	In1	-808.90009	-808.99524
	In2	-808.96825	-809.03815

**Table 7.2:** Calculated volume and lattice parameters for a 120 atom supercell with an In-vacancy for  $P\bar{3}c1$  and  $P6_3cm$ . The lattice parameters are divided on two and volume on four to ease the comparison with experimental values. Calculations were done for the different In-vacancy positions given in Table 3.1. Both fixed volume and relaxed volume calculations were performed.

Structure	In-pos.	Lattice parameter, a [Å]	Lattice parameter, c [Å]	Volume per unit cell, c [Å <sup>3</sup> ]
$P\bar{3}c1$	In1	5.90640	11.59943	347.01
	In2	5.90483	11.60264	347.17
	Fixed vol.	5.90848	11.49836	347.63
$P6_3cm$	In1	5.87025	11.57802	346.73
	In2	5.87801	11.57499	346.85
	Fixed vol.	5.91403	11.46870	347.39

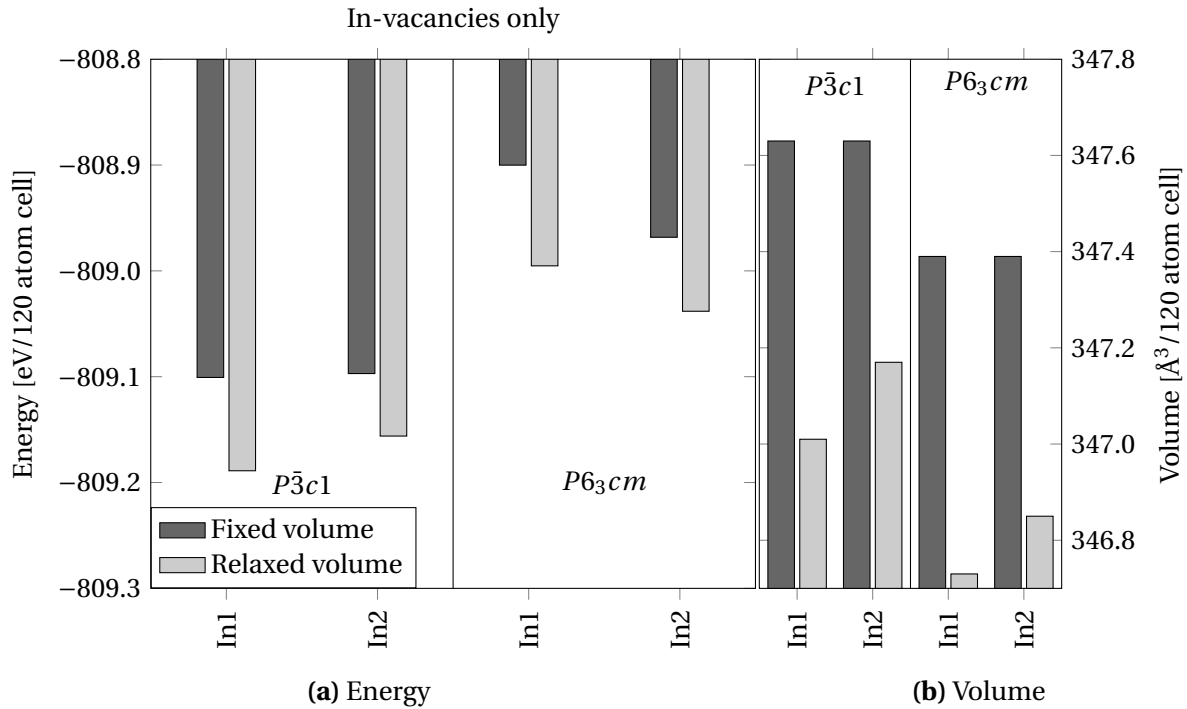


**Figure 7.2:** Barplot showing a) the ground-state energies and b) the volumes calculated for a non-stoichiometric supercell for the  $P\bar{3}c1$  and  $P6_3cm$  phase of  $\text{InMnO}_3$  with an In-vacancy. Structural relaxations were done with fixed and relaxed volume. The In-vacancy positions are given in Table 3.1.

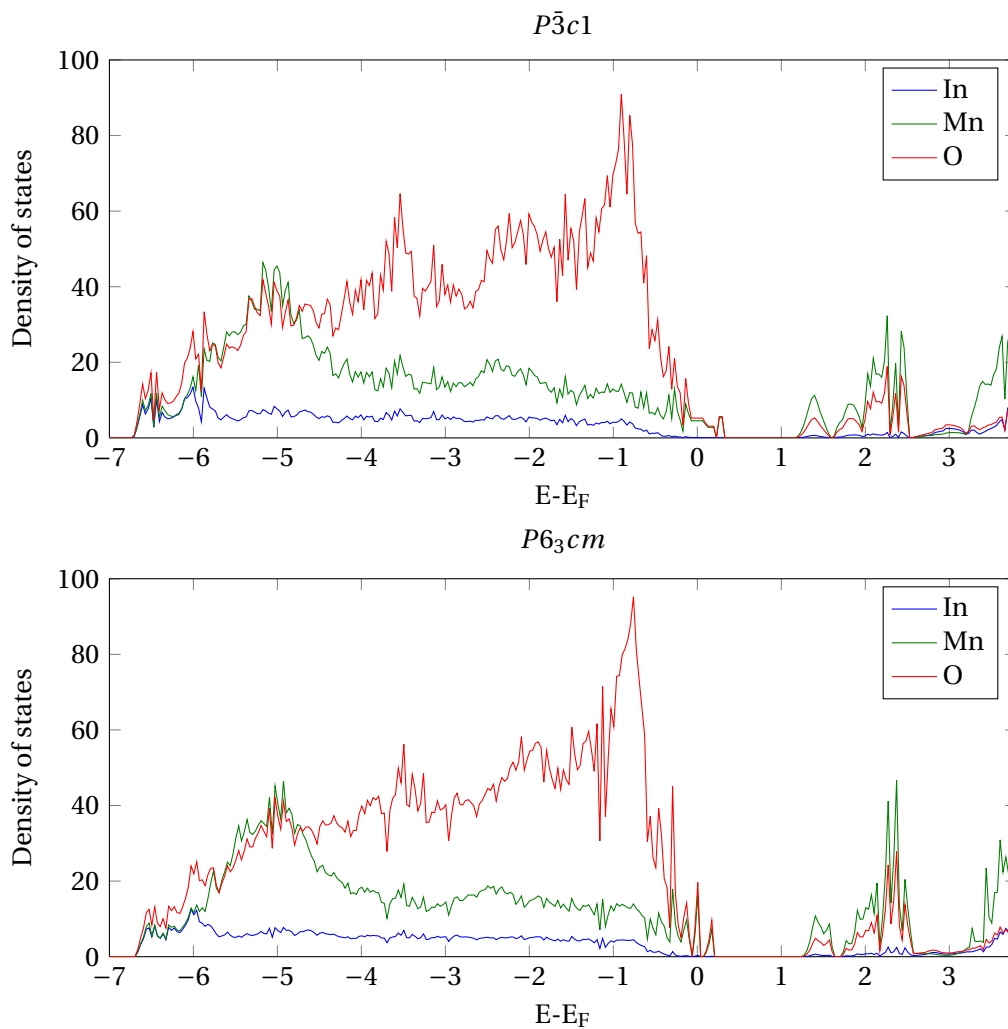


**Figure 7.3:** Plot of the density of states for a non-stoichiometric 120 supercell for the  $P\bar{3}c1$  and  $P6_3cm$  phase of  $\text{InMnO}_3$  with an In-vacancy. For the  $P\bar{3}c1$ -phase the In1-position is shown and for the  $P6_3cm$ -phase the In2-position is shown. Calculations were done with fixed volume.

### 7.1.2 Reducing conditions - In-O vacancy pairs

Table 7.4 and Table 7.3 list the calculated values for the ground-state energy and volume for the different In-O-vacancy pairs for  $P\bar{3}c1$ . Figure 7.4 shows a barplot of the calculated ground-state energy when an In-vacancy and an O-vacancy is present. The supercell was created from a unit cell that was first allowed to fully relax its atom positions, lattice parameters and volume, see section 6.3. Figure 7.5 shows the density of states and Figure 7.8 the relaxed structures for each O-type position for the In1 position in  $P\bar{3}c1$ .

**Table 7.3:** Calculated volume and lattice parameters for a 120 atom supercell with an In-O-vacancy pair for  $P\bar{3}c1$ . The lattice parameters are divided on two and volume on four to ease the comparison with experimental values. Calculations were done for the different In-vacancy positions given in Table 3.1. The oxygen positions for middling reducing conditions are given in Table 3.3.

In- pos.	O- pos.	O.type	Lattice parameter, a [Å]	Lattice parameter, c [Å]	Volume per unit cell, c [Å <sup>3</sup> ]
In1	O1	O-type3	5.90709	11.53889	348.95
	O2	O-type1	5.90543	11.56369	349.53
	O3	O-type2	5.90848	11.49836	347.63
In2	O1	O-type1	5.91407	11.53386	349.40
	O2	O-type3	5.90593	11.54097	349.03
	O3	O-type2	5.90848	11.49836	347.63
Fixed volume case:			5.90848	11.49836	347.63

**Table 7.4:** Calculated ground-state energy for a 120 atom supercell with an In-O-vacancy pair for  $P\bar{3}c1$ . Calculations were done with the different In-vacancy positions given in Table 3.1. The oxygen positions for middling reducing conditions are given in Table 3.3.

In-pos.	O-pos.	O-type	$E_0$ [eV/120 atom cell] w/ fixed volume	$E_0$ [eV/120 atom cell] w/ relaxed volume
In1	O1	O-type3	-802.65713	-802.71843
	O2	O-type1	-803.04141	-803.14190
	O3	O-type2	-803.07944	-803.07944
In2	O1	O-type1	-803.19577	-803.27012
	O2	O-type3	-802.68988	-802.75643
	O3	O-type2	-803.08832	-803.08832

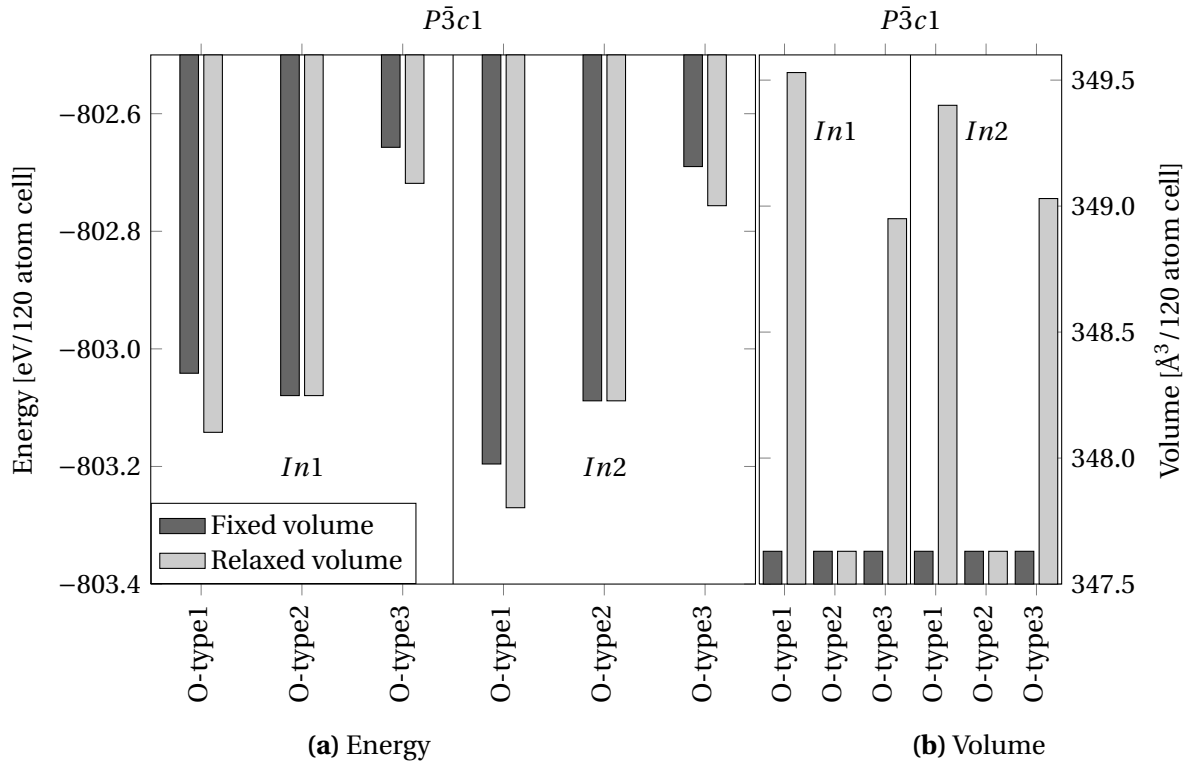


**Figure 7.4:** Barplot showing a) the ground-state energies and b) the volumes calculated for a non-stoichiometric 120 atom supercell for the  $P\bar{3}c1$  phase of  $\text{InMnO}_3$  with an In-O-vacancy pair. Relaxations were done with fixed and relaxed volume. The In-vacancy positions are given in Table 3.1 and O-vacancy positions in Table 3.3.

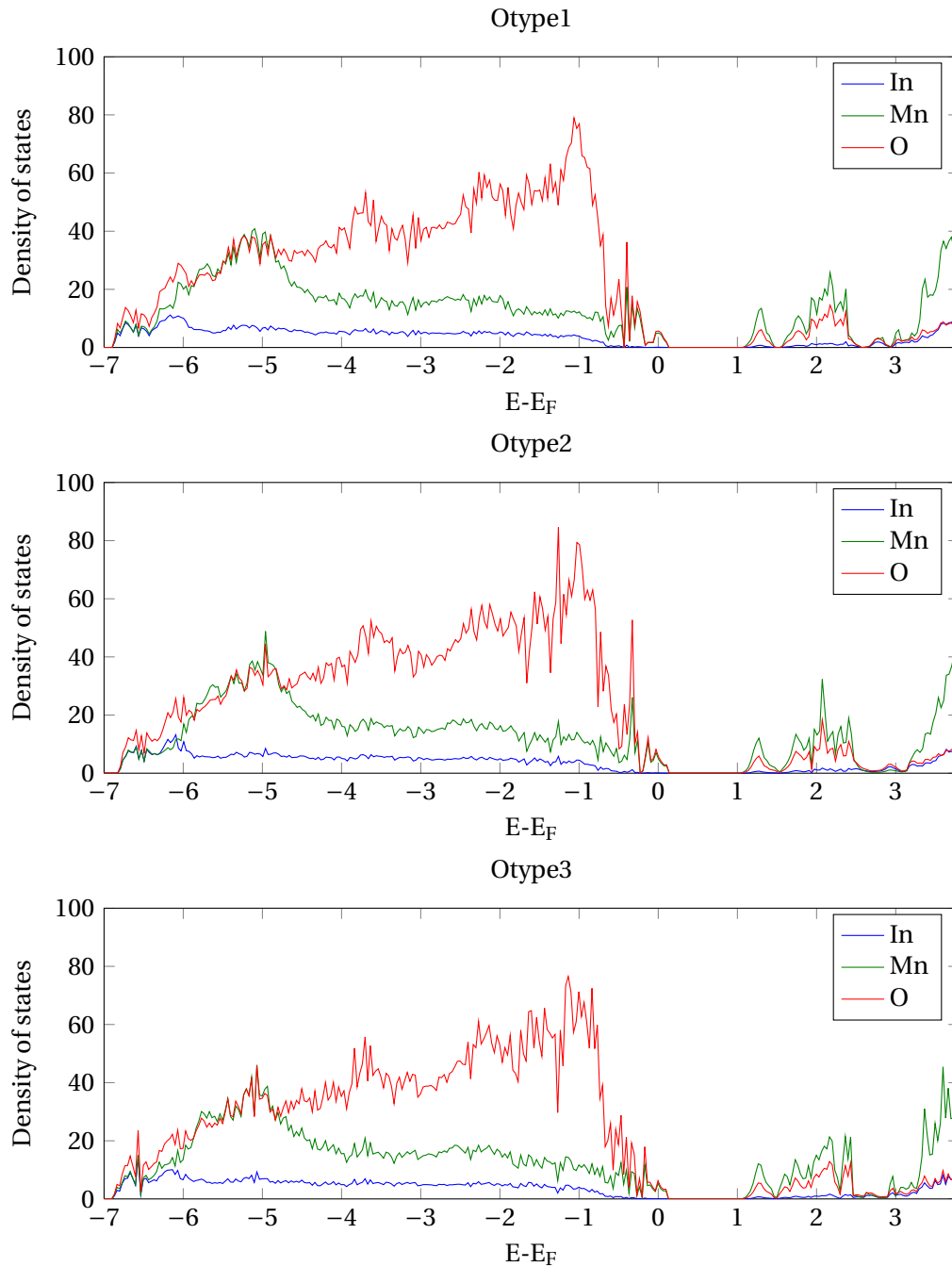


**Figure 7.5:** Plot of the density of states for a non-stoichiometric 120 atom supercell for the  $P\bar{3}c1$  phase of  $\text{InMnO}_3$  with an In-O-vacancy pair. The plot shows the density of state for different oxygen vacancy positions and the In1 position. Calculations were performed with fixed volume.

Table 7.5 and Table 7.6 list the calculated values for the ground-state energy and volume for the different In-O-vacancy pairs for  $P6_3cm$ . Figure 7.6 shows a barplot of the calculated ground-state energy when an In-vacancy and an O-vacancy is present. The supercell was created from a unit cell that was first allowed to fully relax its atom positions, lattice parameters and volume, see section 6.3. Figure 7.7 shows the density of states and Figure 7.8 the relaxed structure for the each O-type position for the In1 position in  $P6_3cm$ .

**Table 7.5:** Calculated ground-state energy for a 120 atom supercell with an In-O-vacancy pair for  $P6_3cm$ . Calculations were done the different In-vacancy positions given in Table 3.1. The oxygen positions for the middling reducing positions are given in Table 3.2 for  $P6_3cm$ .

In-pos.	O-pos.	O-type	$E_0$ [eV/120 atom cell] w/ fixed volume	$E_0$ [eV/120 atom cell] w/ relaxed volume
In1	O1	O-type2	-803.05637	-803.05637
	O3	O-type1	-803.20032	-803.30555
	O4	O-type3	-802.69043	-802.77178
In2	O1	O-type2	-803.01675	-803.06348
	O3	O-type3	-802.57293	-802.67295
	O4	O-type1	-803.28351	-803.37293

**Table 7.6:** Calculated volume and lattice parameters for a 120 atom supercell with an In-O-vacancy pair for  $P6_3cm$ . Calculations were done the different In-vacancy positions given in Table 3.1. The oxygen positions for the middling reducing positions are given in Table 3.2.

In-pos.	O-pos.	O.type	Lattice parameter, a [Å]	Lattice parameter, c [Å]	Volume per unit cell, c [Å <sup>3</sup> ]
In1	O1	O-type2	5.91403	11.46870	347.39
	O3	O-type1	5.89937	11.54533	349.12
	O4	O-type3	5.90315	11.53009	348.81
In2	O1	O-type2	5.89374	11.53310	347.71
	O3	O-type3	5.90941	11.54855	348.88
	O4	O-type1	5.90329	11.53467	349.03
Fixed volume case:			5.91403	11.46870	347.39



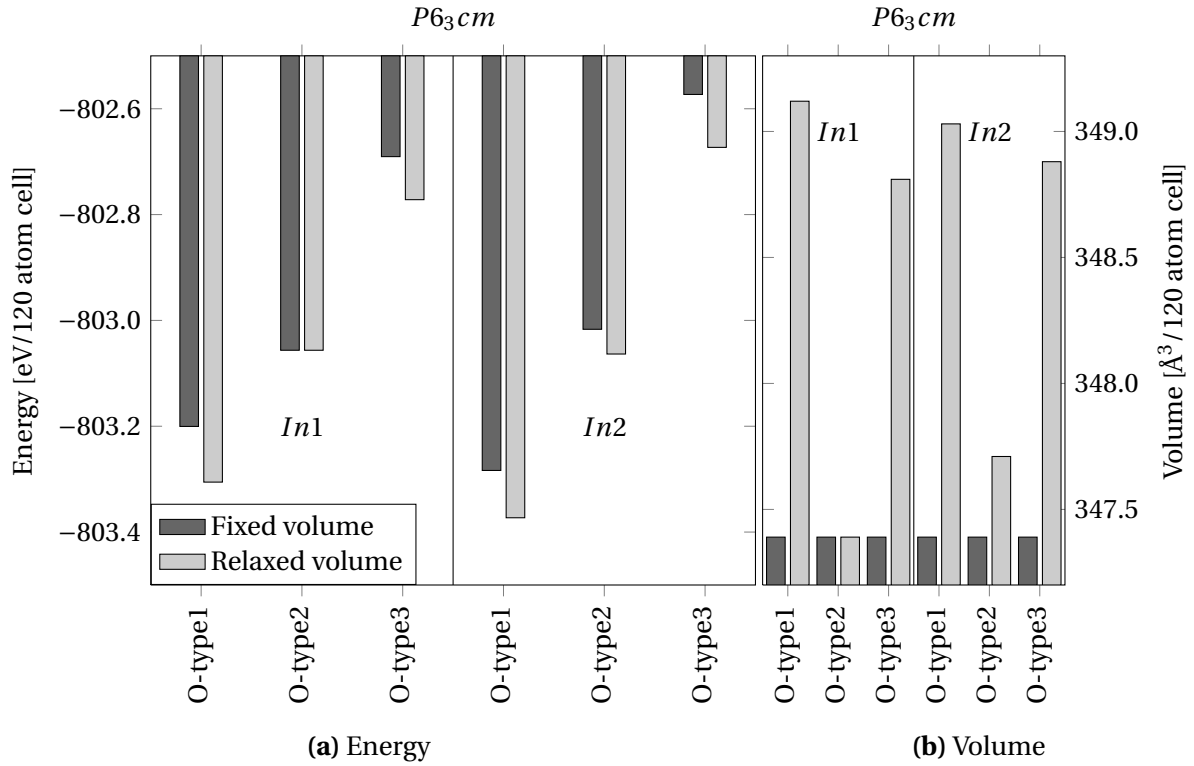


**Figure 7.6:** Barplot showing a) the ground-state energies and b) the volumes calculated for a non-stoichiometric 120 atom supercell for the  $P6_3cm$  phase of  $\text{InMnO}_3$  with an In-O-vacancy pair. Relaxations were done with fixed and relaxed volume. The In-vacancy positions are given in Table 3.1 and O-vacancy positions in Table 3.2.

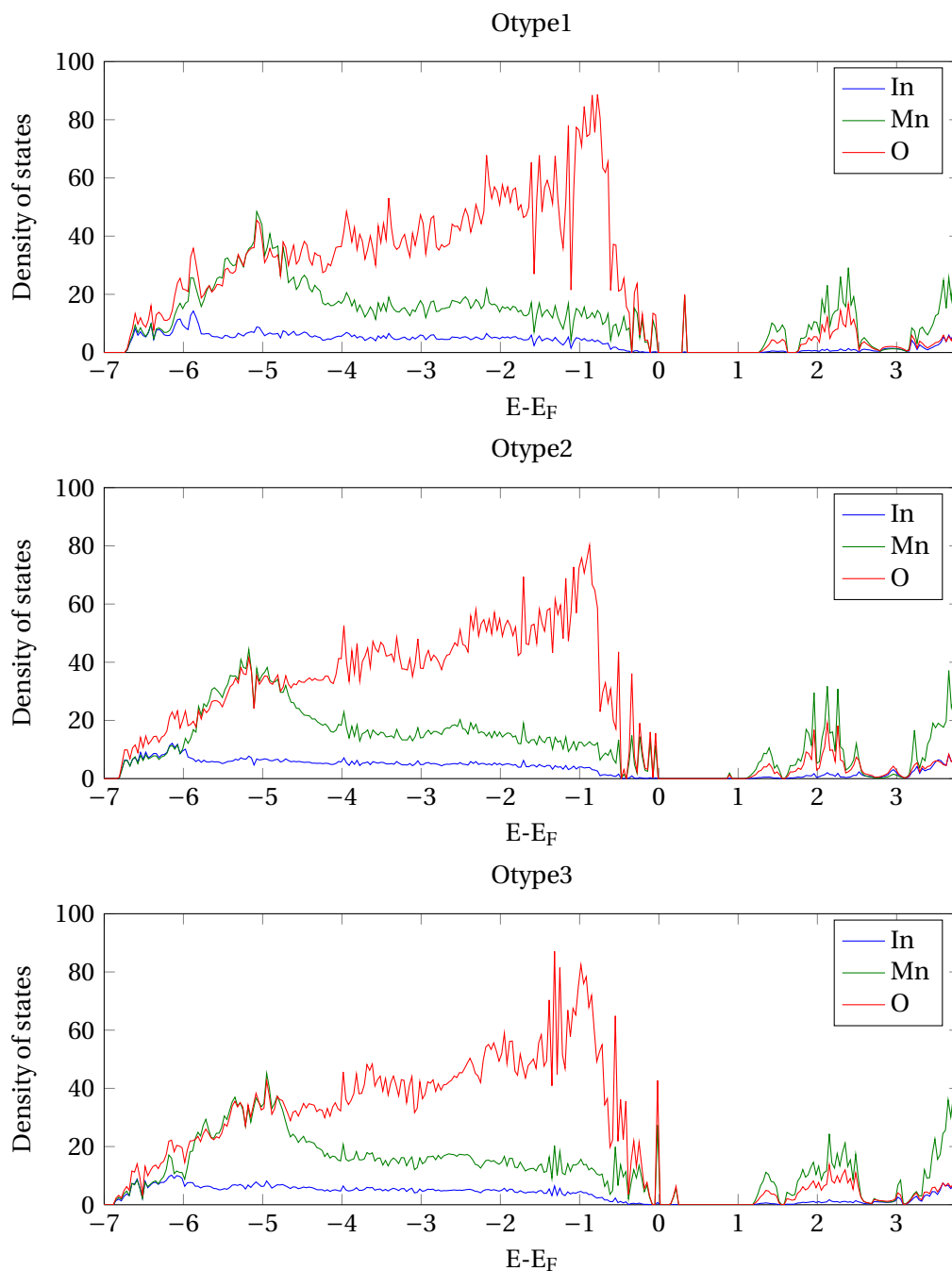


**Figure 7.7:** Plot of the density of states for a non-stoichiometric 120 atom supercell for the  $P6_3cm$  phase of  $\text{InMnO}_3$  with an In-O-vacancy pair. The plot shows the density of state for different oxygen vacancy positions and the In1 position. Calculations were performed with fixed volume.

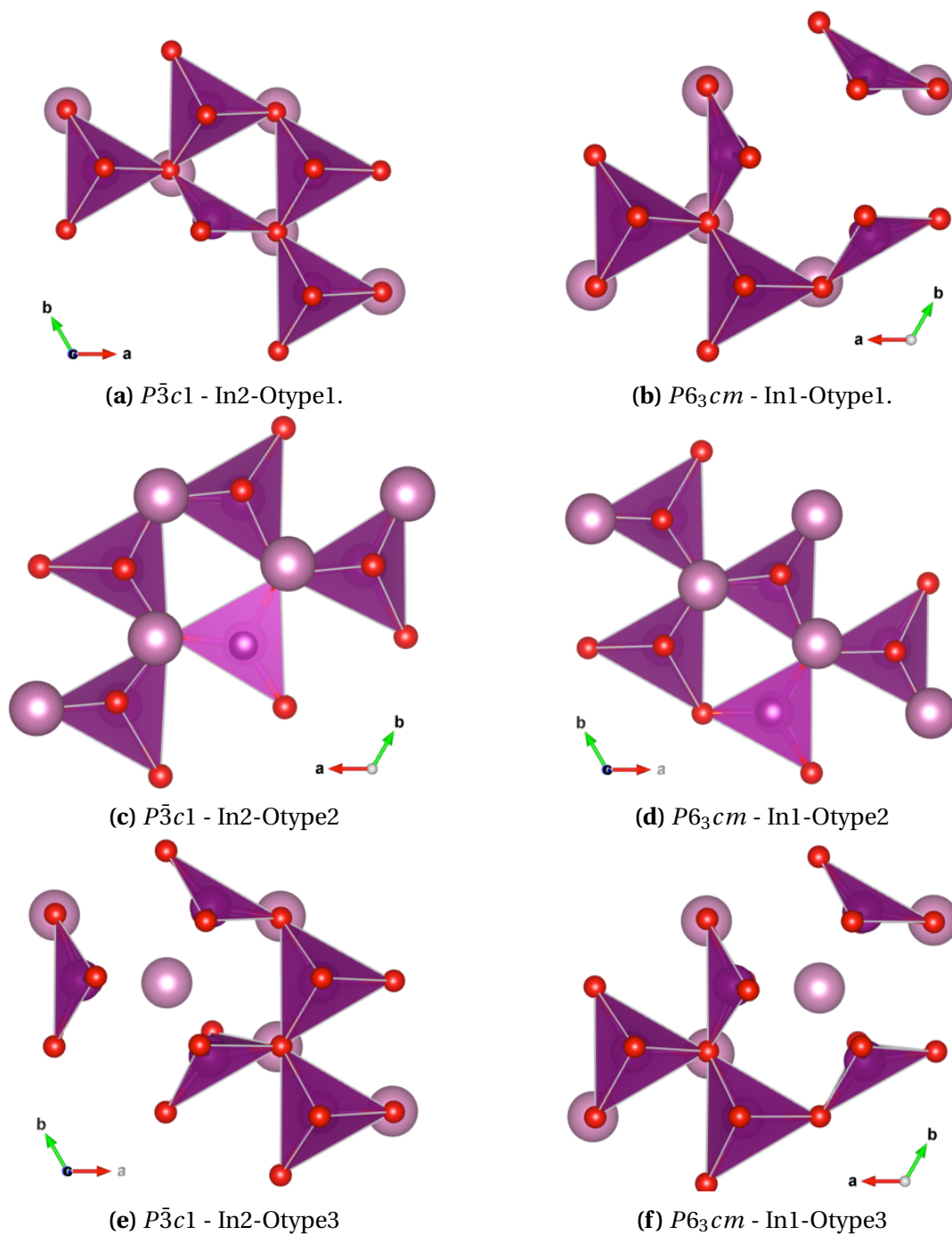


**Figure 7.8:** Relaxed structure of In-O vacancy pairs with different configurations of oxygen and indium position. The positions respective positions can be found in Table 3.1, 3.3 and 3.2. All structures are seen along the c-axis. Calculations were performed with fixed volumes.

### 7.1.3 Energy difference

Figure 7.9 shows the calculated energy difference between  $P\bar{3}c1$  and  $P6_3cm$ ,  $\Delta E = E_{P\bar{3}c1} - E_{P6_3cm}$ . The two first columns represent the case where only an In-vacancy is present. The six last columns represent situations where an In-O-vacancy pair is present. From Table 3.1 it is observed that In1 position of  $P\bar{3}c1$  is equivalent to the In2 position of  $P6_3cm$ . Likewise, the In2 position of  $P\bar{3}c1$  is equivalent to the In1 position of  $P6_3cm$ . When looking at the energy difference between the two structures it is adequate to look at the energy difference between positions that represent the same in each structure. Hence, the energy of the In2 position for the O-type1 configuration in  $P6_3cm$  is subtracted from the energy of the In1 position for the O-type1 configuration in  $P\bar{3}c1$ . The same approach is used for all the other positions.

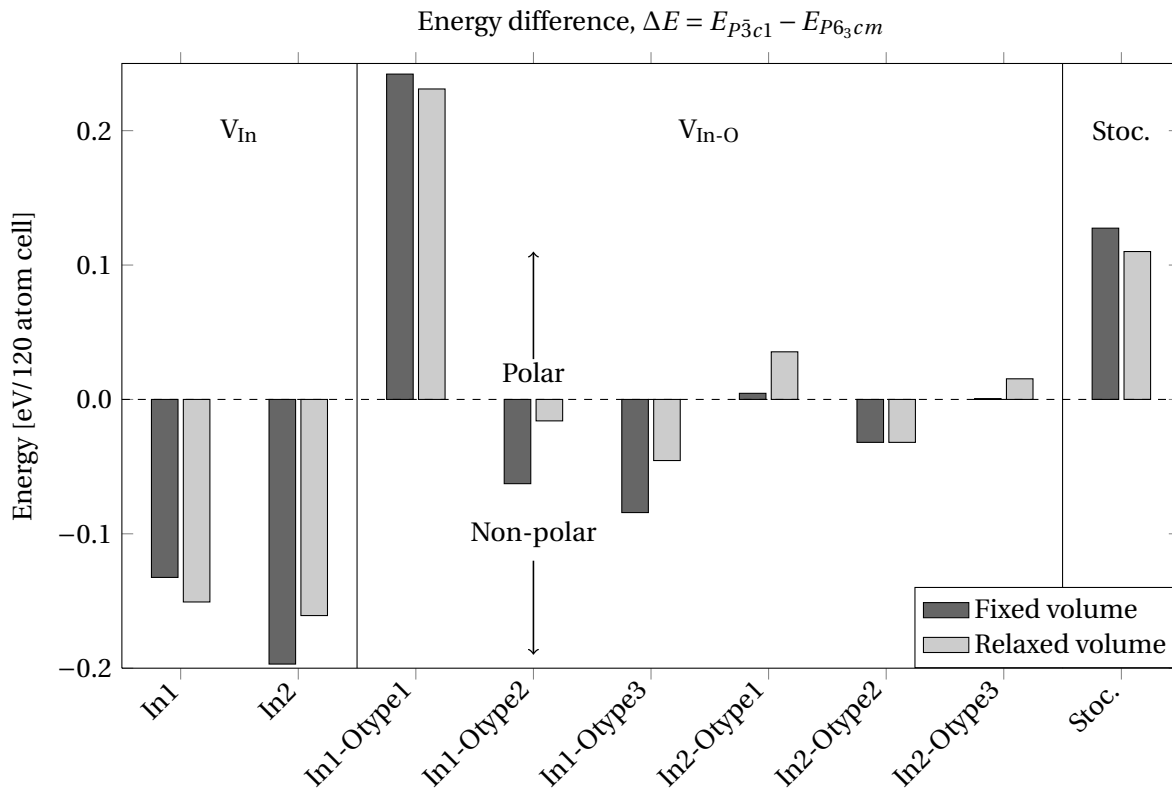


**Figure 7.9:** A barplot of the energy difference,  $\Delta E = E_{P\bar{3}c1} - E_{P6_3cm}$ , between  $P\bar{3}c1$  and  $P6_3cm$  for different In-vacancies. The In-position in the x-axis label represents that of  $P\bar{3}c1$ . The opposite position is equivalent for  $P6_3cm$ . The energy differences for a stoichiometric cell is added for comparison.

### 7.1.4 Calculation of formation energy of defects

To calculate the formation energy for an In-vacancy and an In-O-vacancy pair equation 3.18 and 3.19 were used. The chemical potential of In was calculated by the same method as used by Shigemi et al. for  $\text{KNbO}_3$ [54].  $\text{In}_2\text{O}_3$  was used to find an appropriate chemical potential for In in  $\text{InMnO}_3$ . The following equation was used:

$$\mu_{\text{In}} = \frac{1}{2}E_{\text{In}_2\text{O}_3} - \frac{3}{2}\mu_{\text{O}} \quad (7.1)$$

The ground-state energy for  $\text{In}_2\text{O}_3$  was calculated by DFT with relaxed volume and the same criteria as the defect calculations. The ground-state energy was found to be -29.93 eV/f.u. Figure 7.10 shows the formation energy of the most stable configurations of In-vacancies and In-O-vacancy pairs plotted against the chemical potential of oxygen.

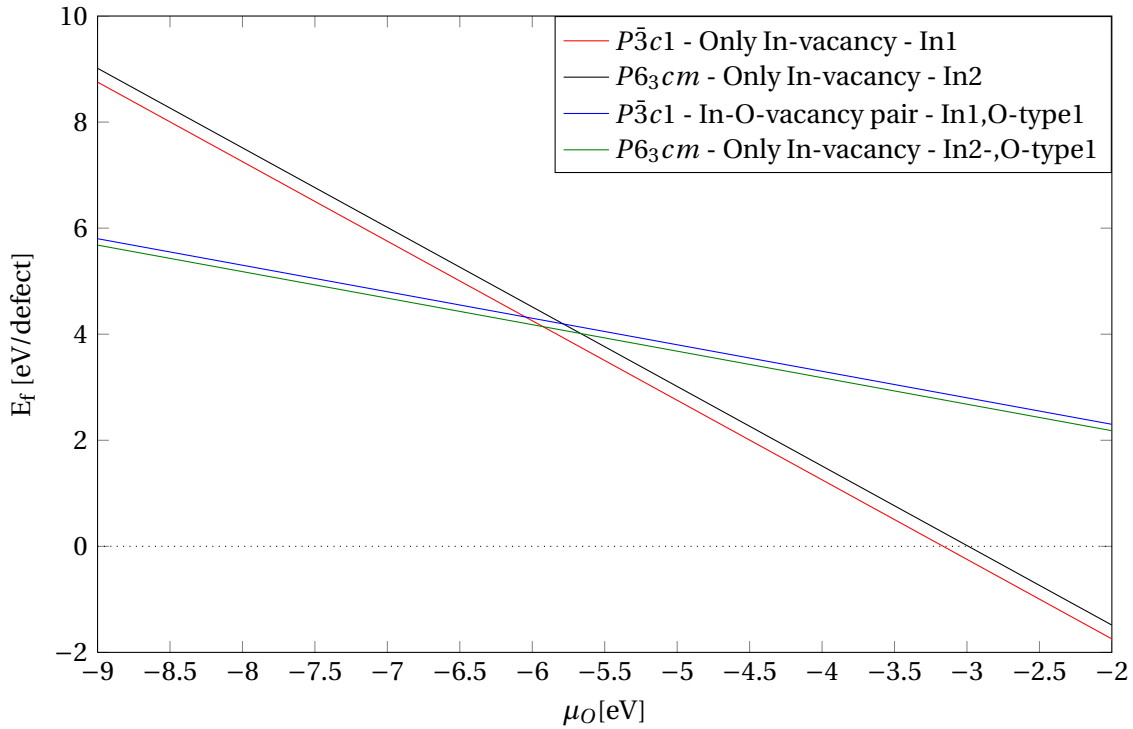


**Figure 7.10:** Plot of the formation energy of In-vacancies as a function of the chemical potential of oxygen. The calculations were performed with relaxed volume.

## 7.2 Phase transition calculations

The activation energy barrier was calculated for a stoichiometric cell and defect cells. All calculations were done two or three times, with one, three and five images. This was done to verify that the correct minimum energy path (MEP) was found. The initial  $P\bar{3}c1$  and  $P6_3cm$  for the different defects and the stoichiometric cell were taken from relaxations done to find the ground-state energy. All calculations were done on a 120 atom supercell, but the energies are scaled down to a 30 atom unit cell.

### 7.2.1 Stoichiometric cell

Table 7.7 and Figure 7.11 shows the minimum energy path (MEP), as well as the calculated activation energy barrier for a phase transition between  $P\bar{3}c1$  (Initial state) and  $P6_3cm$  (Final state) for a stoichiometric cell. Since one and three images did not give the same MEP a calculation with five images were done for confirmation. A software called FINDSYM[55, 56] was used on to identified the space group for each image. The tolerance for the software was set to 0.1.

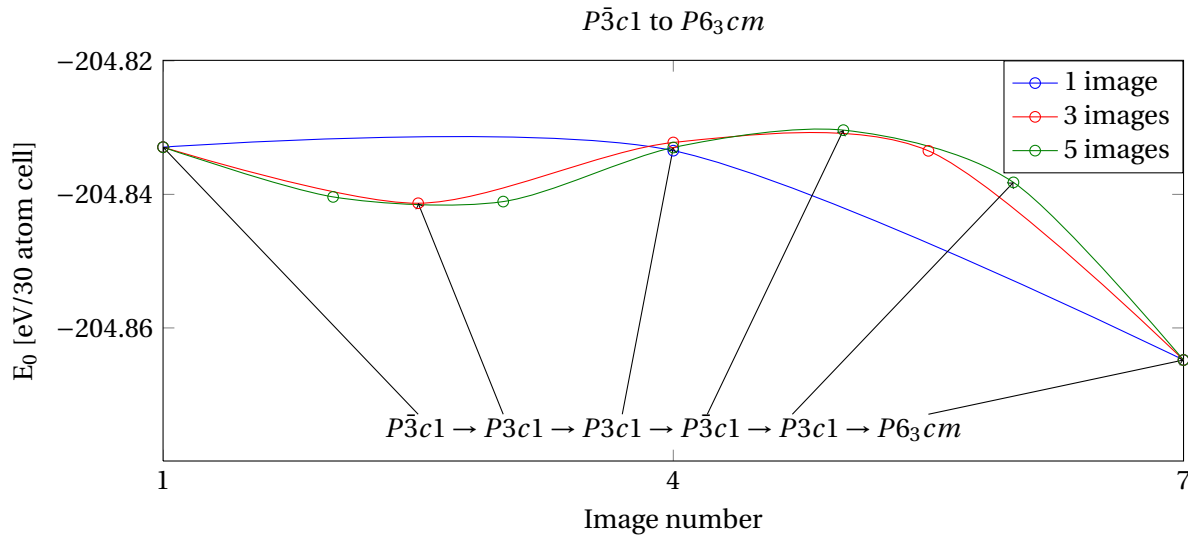


**Figure 7.11:** Plot showing the minimum energy path for the phase transition between stoichiometric  $P\bar{3}c1$  and  $P6_3cm$ . Calculations were performed with fixed volume. FINDSYM[55, 56] was used to identify the space group for each image. The tolerance for the software was set to 0.1.

**Table 7.7:** Calculation of the minimum energy path for the phase transition between stoichiometric  $P\bar{3}c1$  and  $P6_3cm$ . Calculations were performed with fixed volume.

Images	State	$E_0$ [eV/30 atom cell] w/ fixed volume	Energy diff. from $P\bar{3}c1$ [eV/30 atom cell]
1	$P\bar{3}c1$	-204.8330	0
	Image1	-204.8335	-0.0005
	$P6_3cm$	-204.8649	-0.0319
3	$P\bar{3}c1$	-204.8330	0
	Image1	-204.8414	-0.0084
	Image2	-204.8323	0.0007
	Image3	-204.8336	-0.0006
	$P6_3cm$	-204.8649	-0.0319
5	$P\bar{3}c1$	-204.8330	0
	Image1	-204.8405	-0.0075
	Image2	-204.8412	-0.0082
	Image3	-204.8331	-0.00005
	Image4	-204.8304	0.0026
	Image5	-204.8382	-0.0053
	$P6_3cm$	-204.8649	-0.0319

### 7.2.2 Defect cells

The defect positions listed in Table 7.8 were used. These represent the most stable defect positions of interstitial oxygens and In-O vacancy pairs presented in this master thesis and in previous project work. The oxygen vacancy position and In-vacancy position was chosen out of convenience since both  $P\bar{3}c1$  and  $P6_3cm$  were relaxed at these positions. To do calculations on phase transitions every atom in the  $P\bar{3}c1$ -structure have to represent an atom in the  $P6_3cm$ -structure. Therefore the unit cell of  $P6_3cm$  was transposed with  $3/4$  in z-direction to be similar to  $P\bar{3}c1$ . For all calculations on defect cells a  $2 \times 2 \times 1$  supercell were used. However, the results from the calculations are presented in terms of a unit cell. In theory the top-most point should be the same for both one, three and five images. This is not the case for a cell with an interstitial oxygen and an In-O-vacancy pair. It seems that more images are necessary to find the true MEP. The results are still useful for qualitative comparison.

**Table 7.8:** Defect positions used for calculation on the activation energy barrier for different non-stoichiometric cells when going from  $P\bar{3}c1$  to  $P6_3cm$  for  $\text{InMnO}_3$ .

Defect type	Position in $P\bar{3}c1$	Position in $P6_3cm$	Fractional coordinates
$V_{\text{In-red.}}$	In2+Otype1	In1+Otype1	In(0,0,0) and O(0,0,1/4)
$V_{\text{In-ox.}}$	In2	In1	In(0,0,0)
$O_i$	Oi1	Oi1	(1/3,1/3,3/4)
$V_O$	O1-planar	O3-planar	(0,0,1/4)

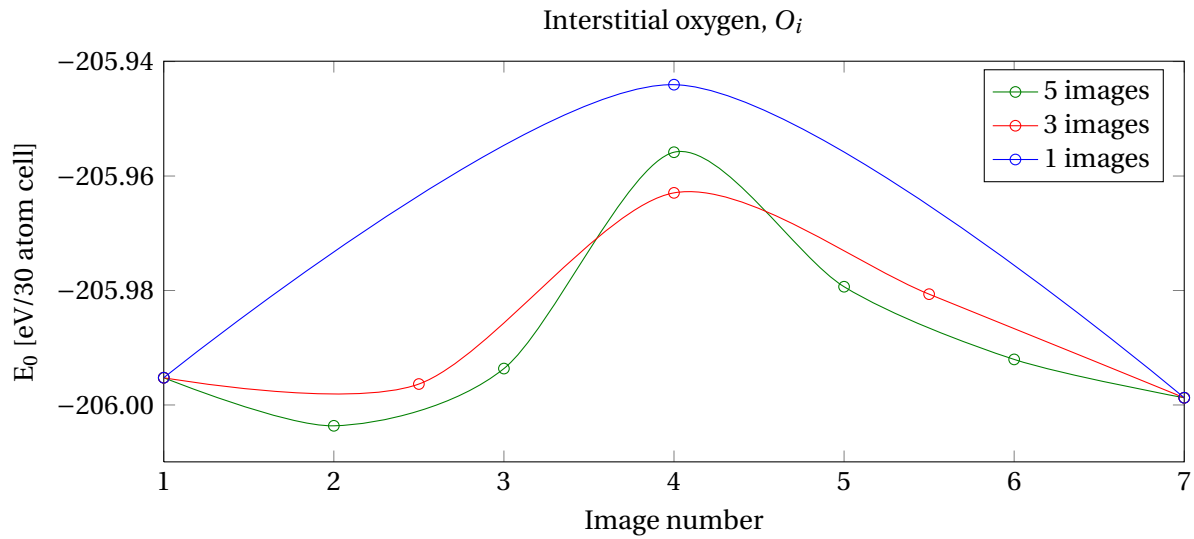
### Interstitial oxygen

Table 7.9 and Figure 7.12 show the minimum energy path (MEP), as well as the calculated activation energy barrier. Since one and three images did not give the same MEP a calculation with five images were done for confirmation.

**Table 7.9:** Calculation of the minimum energy path for the phase transition between non-stoichiometric  $P\bar{3}c1$  and  $P6_3cm$  with an interstitials oxygen at the position given in Table 7.8. Calculations were performed with fixed volume.

Images	State	$E_0$ [eV/30 atom cell] w/ fixed volume	Energy diff. from $P\bar{3}c1$ [eV/30 atom cell]
1	$P\bar{3}c1$	-205.9953	0
	Image1	-205.9442	0.0512
	$P6_3cm$	-205.9988	-0.0035
3	$P\bar{3}c1$	-205.9953	0
	Image1	-205.9964	-0.0011
	Image2	-205.9631	0.0323
	Image3	-205.9807	0.0146
	$P6_3cm$	-205.9988	-0.0035
5	$P\bar{3}c1$	-205.9953	0
	Image1	-206.0037	-0.0084
	Image1	-205.9937	0.0016
	Image1	-205.9559	0.0395
	Image1	-205.9794	0.0160
	Image1	-205.9921	0.0033
	$P6_3cm$	-205.9988	-0.0035





**Figure 7.12:** Plot showing the minimum energy path for the phase transition between non-stoichiometric  $P\bar{3}c1$  and  $P6_3cm$  with an interstitial oxygen at the position given in Table 7.8. Calculations were performed with fixed volume.

### Vacant oxygen

Table 7.10 and Figure 7.13 show the minimum energy path (MEP), as well as the calculated activation energy barrier.

**Table 7.10:** Calculation of the minimum energy path for the phase transition between non-stoichiometric  $P\bar{3}c1$  and  $P6_3cm$  with a vacant oxygen at the position given in Table 7.8. Calculations were performed with fixed volume.

Images	State	$E_0$ [eV/30 atom cell] w/ fixed volume	Energy diff. from $P\bar{3}c1$ [eV/30 atom cell]
1	$P\bar{3}c1$	-202.6631	0
	Image1	-202.6076	0.0555
	$P6_3cm$	-202.6976	-0.0345
3	$P\bar{3}c1$	-202.6631	0
	Image1	-202.6441	0.019
	Image2	-202.6075	0.0556
	Image3	-202.6473	0.0159
	$P6_3cm$	-202.6976	-0.0345

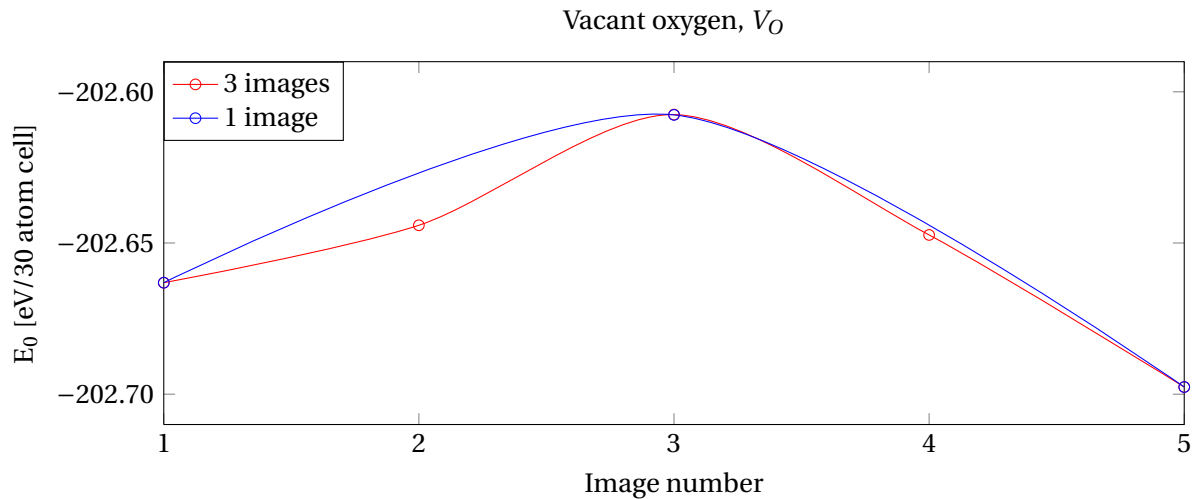


**Figure 7.13:** Plot showing the minimum energy path for the phase transition between non-stoichiometric  $P\bar{3}c1$  and  $P6_3cm$  with an oxygen vacancy at the position given in Table 7.8. Calculations were performed with fixed volume.

### Vacant indium

Table 7.11 and Figure 7.14 shows the calculated energy for the saddlepoint, as well as the calculated activation energy barrier. This NEB calculation was also performed with a stricter force criterion of -0.01 eV producing the same results. This indicates that the chosen force criterion of -0.05 eV is sufficient for NEB calculations.

**Table 7.11:** Calculation of the minimum energy path for the phase transition between non-stoichiometric  $P\bar{3}c1$  and  $P6_3cm$  with an In-vacancy at the position given in Table 7.8. Calculations were performed with fixed volume.

Images	State	$E_0$ [eV/30 atom cell] w/ fixed volume	Energy diff. from $P\bar{3}c1$ [eV/30 atom cell]
1	$P\bar{3}c1$	-202.2743	0
	Image1	-202.2631	0.0112
	$P6_3cm$	-202.2250	0.0493
3	$P\bar{3}c1$	-202.2743	0
	Image1	-202.2717	0.0026
	Image2	-202.2646	0.0097
	Image3	-202.2584	0.0159
	$P6_3cm$	-202.2250	0.0493

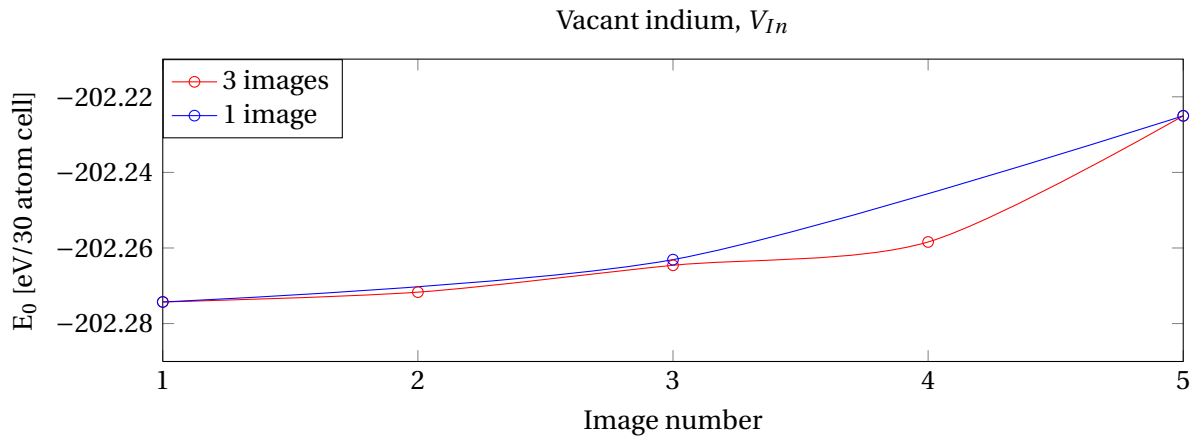


**Figure 7.14:** Plot showing the minimum energy path for the phase transition between non-stoichiometric  $P\bar{3}c1$  and  $P6_3cm$  with an In-vacancy at the position given in Table 7.8. Calculations were performed with fixed volume.

### Vacant indium-oxygen pair

Table 7.12 and Figure 7.15 show the minimum energy path (MEP), as well as the calculated activation energy barrier. Since one and three images did not give the same MEP a calculation with five images were done for confirmation.

**Table 7.12:** Calculation of the minimum energy path for the phase transition between non-stoichiometric  $P\bar{3}c1$  and  $P6_3cm$  with an In-O-vacancy pair at the position given in Table 7.8. Calculations were performed with fixed volume.

Images	State	$E_0$ [eV/30 atom cell] w/ fixed volume	Energy diff. from $P\bar{3}c1$ [eV/30 atom cell]
1	$P\bar{3}c1$	-200.7989	0
	Image1	-200.7990	-0.00003
	$P6_3cm$	-200.8001	-0.0012
3	$P\bar{3}c1$	-200.7989	0
	Image1	-200.8024	-0.0035
	Image2	-200.7999	-0.0010
	Image3	-200.8000	-0.0011
	$P6_3cm$	-200.8001	-0.0012
5	$P\bar{3}c1$	-200.7989	0
	Image1	-200.8032	-0.0043
	Image2	-200.8014	-0.0024
	Image3	-200.7996	-0.0007
	Image4	-200.7986	0.0003
	Image5	-200.8008	-0.0019
	$P6_3cm$	-200.8001	-0.0012

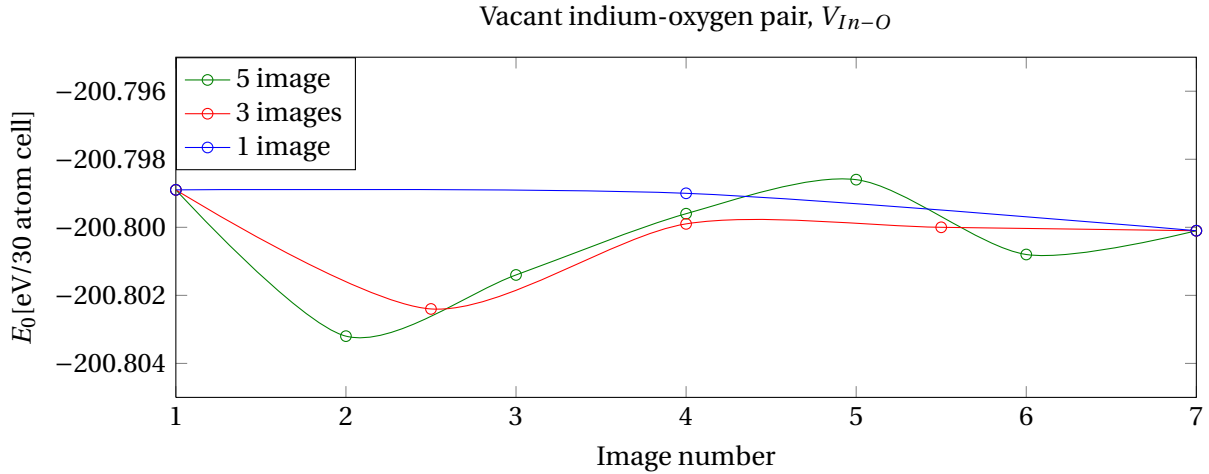


**Figure 7.15:** Plot showing the minimum energy path for the phase transition between non-stoichiometric  $P\bar{3}c1$  and  $P6_3cm$  with an In-O-vacancy pair at the position given in Table 7.8. Calculations were performed with fixed volume.

### 7.2.3 Summary - activation energy barriers

Table 7.13 gives an overview of the calculated activation energy barriers for the transition between  $P\bar{3}c1$  and  $P6_3cm$  in  $\text{InMnO}_3$ . The table includes values for both a stoichiometric cell and a cell with different types of defects. The activation energy barrier is in each case measured as the energy difference between  $P\bar{3}c1$  and the highest point on the MEP.

**Table 7.13:** Summary of the calculated activation energy barriers for a transition between  $P\bar{3}c1$  and  $P6_3cm$  for a stoichiometric cell and different non-stoichiometric cells. The activation energy barrier is in each case measured as the energy difference between  $P\bar{3}c1$  and the highest point on the MEP.

Defect type	Position $P\bar{3}c1$	Position $P6_3cm$	Activation energy barrier [eV/30 atom cell]
Stoichiometric cell			0.026
$V_{In}$ -red.	In2+Otype1	In1+Otype1	0.040
$V_{In}$ -ox.	In2	In1	0.056
$O_i$	Oi1	Oi1	0.003
$V_O$	O1-planar	O3-planar	None

### 7.3 Calculations of polarization

To investigate the effect of point defects on the polarization of the ferroelectric  $P6_3cm$ -phase two methods were used, the point charge model and Berry-Phase calculations with DFT. In both cases the structure with the relevant point defect relaxed with fixed volume were used. An artificial non-polar structure was made for each case and used as a reference state. The positions of the point defects investigated were the same as for the calculations on phase transitions, see Table 7.8. Table 7.14 shows the calculated values of the polarization in  $P6_3cm$  with different types of defects. The polarization was calculated with the point charge model and the Berry-Phase-method for a stoichiometric cell, a cell with an interstitial oxygen, a cell with an oxygen vacancy and a cell with an In-O-vacancy pair. For the case with an In-vacancy under oxidizing conditions only the point charge model was used. This because the polar phase of  $\text{InMnO}_3$  with an In-vacancy turns metallic making it impossible to do Berry-Phase-calculations. This is elaborated in the discussion. Figure 7.16 shows the calculated polarization from Berry-Phase calculations for the polar  $P6_3cm$ -phase for  $\text{InMnO}_3$ . The spontaneous polarization is given as the value at 100%.

**Table 7.14:** Calculated polarization of  $P6_3cm$  with different defects by use of the point charge model and Berry-Phase-model. The positions of the different defects are given in Table 7.8. All calculations were based on structures relaxed with fixed volume.

Type	Defect position	Point charge model [ $\mu\text{C}/\text{cm}^2$ ]	Berry-Phase [ $\mu\text{C}/\text{cm}^2$ ]	Property
Stoc.	None	0.4370	3.7211	Insulator
Vacant O	(0,0,1/4)	2.5781	4.8405	Insulator
Interstitial O	(1/3,1/3,0)	1.5085	3.3106	Insulator
Vacant In	In1	0.0687	-	Metal
Vacant In-O-pair	In1 + Otype1	0.9859	3.7878	Insulator

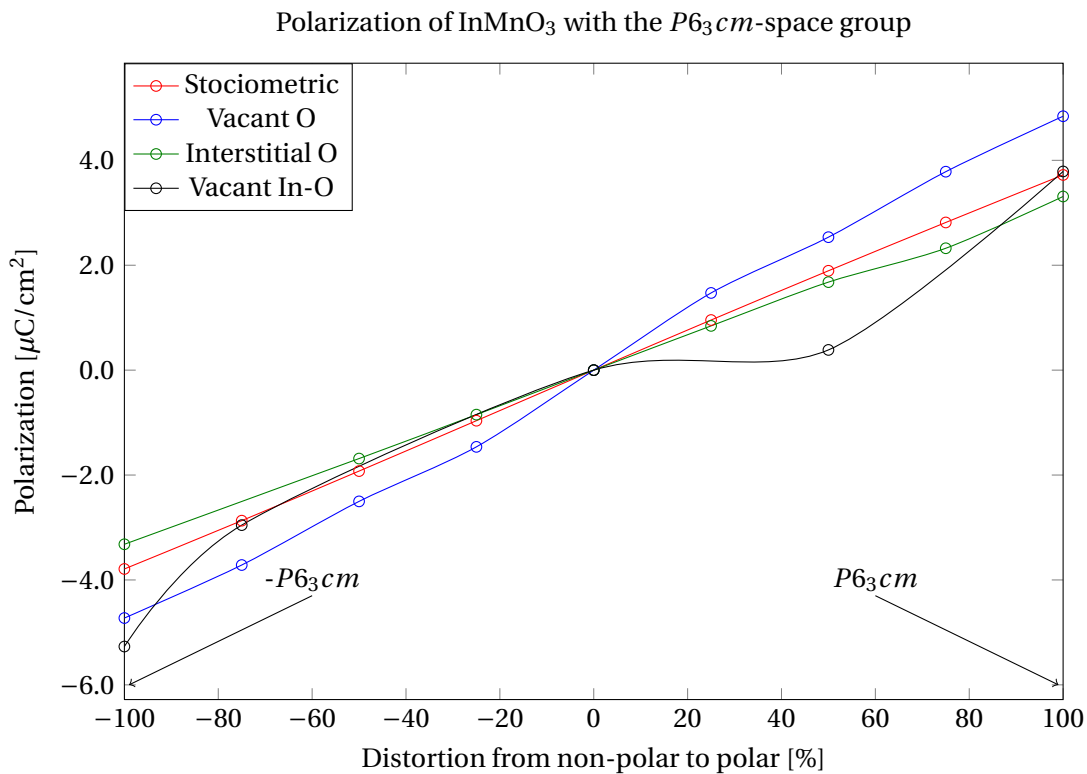


**Figure 7.16:** Plot showing the calculated polarization of the polar  $P6_3cm$ -phase for  $\text{InMnO}_3$ . The calculations were performed for a stoichiometric cell and cells with different defects. All calculations were based on  $2 \times 2 \times 1$  supercells relaxed with fixed volume. The defect positions can be found in Table 7.8.





## Chapter 8

# Discussion

### 8.1 In-vacancies

From calculations performed in earlier work, see Figure C.1 in Appendix C, it is shown that the ferroelectric  $P6_3cm$  phase is vaguely favoured over the paraelectric  $P\bar{3}c1$  phase in stoichiometric  $\text{InMnO}_3$ . This is in agreement with similar results published by Lee et al.[12] and Kumagai et al.[7]. It also supports the similarity to other hexagonal manganites that crystallize into the  $P6_3cm$  structure. Previous work[1] showed that point defects of interstitial and vacant oxygen decreased the energy difference between the two phases, but kept the  $P6_3cm$  phase as the most stable. From Figure 7.4, 7.6 and 7.2 it is observed that different In-vacancies have a dramatic effect on the stability of the ferroelectric versus the paraelectric phase. The two different cases of In-vacancies, only In-vacancies and In-O vacancy pairs, are discussed further below.

Vacancy formation of cations is not easy to control. The formation of oxygen vacancies and interstitial oxygen is a reversible process, while formation of In-vacancies can be irreversible. In-vacancies occurring early in the preparation of the material can therefore be hard to remove later on. Recently it has been shown that a large Y deficiency is possible for  $\text{YMnO}_3$ [16]. Although not verified experimentally this might also be the case for  $\text{InMnO}_3$  since both are hexagonal manganites. In other words, the presence of In-vacancies are not unlikely and can for instance be created by synthesizing  $\text{InMnO}_3$  with less In than the stoichiometric amount.

#### 8.1.1 Oxidizing conditions - Favouring the non-polar phase

As mentioned in section 3.2 oxidizing condition will prevent the formation of oxygen vacancies. In such environment In-vacancies will be charge compensated by manganese, see section 3.2.1. Oxidizing condition can be obtained by performing the synthesis in an oxygen rich environment (e.g. use high partial pressure of oxygen).

### Favourable vacant In-position

From Figure 7.9 it is observed that the energy difference between  $P\bar{3}c1$  and  $P6_3cm$  for a cell with an In-vacancy is negative. Consequently, for this configuration the  $P\bar{3}c1$ -phase is more stable than the  $P6_3cm$ -phase. This means the non-polar phase is favoured over the polar phase. In1 for the non-polar state is equal to In2 for the polar phase, and opposite. To ease the discussion In1 in  $P\bar{3}c1$  and In2 in  $P6_3cm$  are referred to as In-2 (since they have a multiplicity of 2 in the unit cell). By use of the same approach, In2 in  $P\bar{3}c1$  and In1 in  $P6_3cm$  are referred to as In-8 (8 in multiplicity in the unit cell). See Figure 3.3 for a sketch. Vacant In-2 gives the lowest energy for both phases, which means that due to energetics removal of an In-2 is favoured over an In-8. Zhang et al.[57] performed molecular dynamics (MD) calculations<sup>1</sup> on different Y substitutions in  $YMnO_3$ . It was shown that the Y-2 position (Y2) in the  $P6_3cm$  structure for  $YMnO_3$  was the preferred position for substitution. Although MD calculations are not as accurate as DFT calculations these results still indicate that what observed in  $InMnO_3$  can be found in other hexagonal manganites as well. Table 8.3 shows the distance between an In atom and three different surrounding oxygen atoms. It is observed that the In-2 in general is placed further away from the oxygen atoms than the In-8. When creating an In-vacancy by removing an In-atom a negative charge arises at the position. Since oxygen is placed further away from the In-vacancy for In-2 compared to In-8 the negative repulsion between oxygen and vacant In will be smaller. Accordingly the In-2 position will give a more stable structure both for  $P\bar{3}c1$  and  $P6_3cm$ .

### Change in volume

All calculations were done with both fixed volume and relaxed volume in order to observe the change in volume and lattice parameters when defects were introduced. Table 8.1 gives the %-change in lattice parameters and volume when the structure is fully relaxed. From the proposed Kröger-Vink equation, see equation 3.2, it is observed that three Mn-atoms are oxidized from  $Mn^{3+}$  to  $Mn^{4+}$  to compensate for the three electrons left by the In-vacancy<sup>2</sup>. When atoms increase their valence state the atomic radius is reduced, because the core has fewer electrons to attract. Hence, high-spin  $Mn^{3+}$  (0.645 Å) is larger than  $Mn^{4+}$  (0.53 Å)[59]. From Table 8.1 a volume decrease is observed for In-vacancies in both structures. This is in conclu-

<sup>1</sup>The molecular dynamics method was developed by Alder and Wainwright in 1959[58] to calculate the behaviour of several interacting classical particles.

<sup>2</sup>In section 8.3 it is shown that only one Mn-atom is oxidized.

sion with the reduced atom size. However, by taking a closer look at the change in the lattice parameter it is evident that the total contraction in volume is actually a result of a decrease in the  $a$  lattice parameter and an increase in the  $c$  lattice parameter.

The contraction in the Mn-layer (given by the  $a$  lattice parameter) is most likely caused by what stated above, the decrease in size when Mn is oxidized. By studying Figure 7.1 it is observed that the trigonal bipyramids tilt away from the In-vacancy. The increased tilting will contribute to the contraction in the Mn-layer since the pyramids can move closer together. When an indium is removed from the structure the positive shielding of the "electron cloud" between apical oxygen atoms in the layer above and below the In-vacancy is removed. This will result in repulsive forces between the oxygen atoms and make them move further apart, hence increase the  $c$  lattice parameter.

**Table 8.1:** Summary of change in volume when full relaxations were allowed for an In-vacancy. The change is found by comparing with volume and lattice parameters given in fixed volume calculations.

Structure	Type	Change in lattice parameter, $a$ [%]	Change in lattice parameter, $c$ [%]	Change in volume [%]
$P\bar{3}c1$	In1	-0.93	0.88	-0.82
	In2	-0.94	0.91	-0.87
$P6_3cm$	In1	-0.26	0.95	-0.81
	In2	-0.39	0.93	-0.84

### 8.1.2 Middling reducing conditions - In-O vacancy pairs

#### Small energy differences between polar and non-polar

From Figure 7.9 it is observed that three positions have positive energy differences and favour the polar phase  $P6_3cm$ . The other three positions have negative energy differences and favour the non-polar phase  $P\bar{3}c1$ . The configuration where the vacant oxygen is placed right above or below the vacant indium, i.e. O-type1 described in Table 3.6.2, gives the most negative ground-state energies and therefore the most stable structure, see Figure 7.4 and 7.6. This

is evident for both  $P\bar{3}c1$  and  $P6_3cm$ . The O-type1 configuration gives a positive energy difference between  $P\bar{3}c1$  and  $P6_3cm$ , see Figure 7.9, meaning vacant In-O-pairs will favour the polar  $P6_3cm$  structure.

For five out of six positions for In-O-vacancy pairs the energy difference between  $P\bar{3}c1$  and  $P6_3cm$  is substantially smaller compared to the cases with only an In-vacancy. An In-vacancy combined with an oxygen vacancy makes the polar and non-polar structures almost equally stable. In previous work[1] it has been shown that oxygen vacancies favour the polar structure, see Appendix C.3. It seems like the combination of In- and O-vacancies counteract each other, in contrast to the clear favouring of the  $P\bar{3}c1$ -phase when only an In-vacancy is present.

### Change in volume

From Table 8.2 it is observed that the volume increases when In-O-vacancy pairs are introduced into the structure. This is opposite of what is observed for only an In-vacancy, see Table 8.1. In previous project work[1] it was shown that the volume of the cell increased for oxygen vacancies. This is most likely related to the fact that the oxygen vacancy is coupled with a reduction of manganese from  $Mn^{3+}$  to  $Mn^{2+}$ . When the Mn-ion acquires one extra electron it increases in size and hence the total volume increases. The suggested mechanism for an In-O-vacancy pair formation does not include a reduction of manganese, but rather an oxidation. One Mn-atom is oxidized from  $Mn^{3+}$  to  $Mn^{4+}$ . Therefore an expansion instead of a contraction of the volume would be expected. The  $a$  lattice parameter decreases in all cases except one. The decrease in the  $a$  lattice parameter can be connected to the decrease in the size of the Mn-atom when it is oxidized, as stated above. The total decrease in the  $a$  lattice parameter is more significant when a In-vacancy is present than for an In-O-vacancy pair, see Table 8.1. In section 8.3 it is shown that for  $P\bar{3}c1$  the charge compensation is delocalized and no Mn-atoms are oxidized. This can explain the minimal decrease of the  $a$  lattice parameter in this case. For  $P6_3cm$  the reduction in the  $a$  lattice parameter can still be explained by oxidation on Mn. When an oxygen is removed from the  $MnO_5$ -trigonal bipyramid the symmetric stabilization of the bipyramid is removed and a positive charge is left at the vacancy position. The Mn- and In-atoms around the oxygen vacancy are positively charged and repulsive forces between these atoms and the vacant oxygen will form. The expansion due to these forces can counteract the effect of the reduced size of the Mn-atom and result in a smaller decrease of the  $a$  lattice parameter for  $P6_3cm$ . The  $c$  lattice parameter increases in size in all

cases. This can be connected to the same as for only In-vacancies, repulsive forces that arise when an In-vacancy is created. For In-O-vacancy pairs the decrease in the  $c$  lattice parameter is larger than for only In-vacancies. The lost oxygen might cause even less shielding resulting in large repulsive forces in the  $c$ -direction. The positive charge left by the oxygen vacancy can increase this effect. From the above reasoning it is found that the total decrease in volume is a result of a smaller contraction of the  $a$  lattice parameter compared to the expansion of the  $c$  lattice parameter.

Note that three of the configurations (i.e.  $P\bar{3}c1$ -In1-Otype2,  $P\bar{3}c1$ -In2-Otype2 and  $P6_3cm$ -In1-Otype2) give no change in volume or lattice parameters when the cell is fully relaxed. This indicates that the cases with the respective In- and O-vacancy changed the structure to a small degree and a geometry optimization was not necessary to reach the force and energy criteria. The result is that the combination of an In-vacancy and an O-type2 vacancy (slanting right above/below the In-vacancy) has no effect on the size and shape of the cell.

**Table 8.2:** Summary of change in volume when full relaxations were allowed for an In-vacancy. The change is found by comparing with volume and lattice parameters given in fixed volume calculations.

Structure	Type	Change in lattice parameter, a [%]	Change in lattice parameter, c [%]	Change in volume [%]
$P\bar{3}c1$	In1, Otype1	-0.95	0.57	0.55
	In1, Otype2	0	0	0
	In1, Otype3	-0.98	0.35	0.38
	In2, Otype1	0.09	0.31	0.51
	In2, Otype2	0	0	0
	In2, Otype3	-0.96	0.37	0.40
$P6_3cm$	In1, Otype1	-0.75	0.67	0.50
	In1, Otype2	0	0	0
	In1, Otype3	-0.82	0.54	0.41
	In2, Otype1	-0.82	0.58	0.47
	In2, Otype2	-0.66	0.56	0.09
	In2, Otype3	-0.92	0.70	0.43

### In-O distance

To examine which oxygen positions give the most stable structure, i.e. the structure with the lowest ground-state energy,  $E_0$  is plotted against the distance between the In- and O-vacancy. To find this distances the coordinates for both In- and O-vacancies were converted from hexagonal to Cartesian, and subsequently inserted into the following equation:

$$d = \sqrt{(x_2 - x_1)^2 + (y_2 - y_1)^2 + (z_2 - z_1)^2} \quad (8.1)$$

where  $d$  is the distance,  $(x_1, y_1, z_1)$  the In-vacancy position and  $(x_2, y_2, z_2)$  the O-vacancy position in Cartesian coordinates given in Ångström, Å. Table 8.3 and Figure 8.1 show the calculated relationship between energy and In-O distance.

The most stable configuration is, as mentioned above, when the O-vacancy is of O-type1. It seems like the structure is most stable when the oxygen vacancy is close to the In-vacancy and in the Mn-plane. This is however not the configuration that gives the smallest distance between In-O-vacancy pairs. In previous work[1] it was shown that apical and planar oxygen vacancies are equally favoured for  $\text{InMnO}_3$ . Because of this it was expected that the In-O-distance would be more relevant for stabilization than the oxygen position relative to the Mn-atom.

**Table 8.3:** Calculation of the distance between In and O for the different In-O vacancy pairs. Data taken from calculations performed with fixed volume.

Structure	In-pos.	O-pos.	In-O distance [Å]	$E_0$ [eV/120 atom cell] w/ fixed volume
$P\bar{3}c1$	In1	O-type3	4.5727	-802.65713
		O-type1	3.2757	-803.04141
		O-type2	2.2079	-803.07944
	In2	O-type1	2.8713	-803.19577
		O-type3	4.3125	-802.68988
		O-type2	2.1767	-803.08832
$P6_3cm$	In1	O-type2	2.1164	-802.71843
		O-type1	2.3793	-803.14190
		O-type3	4.5213	-803.07944
	In2	O-type2	2.1573	-803.27012
		O-type3	4.3481	-802.75643
		O-type1	2.6490	-803.08832

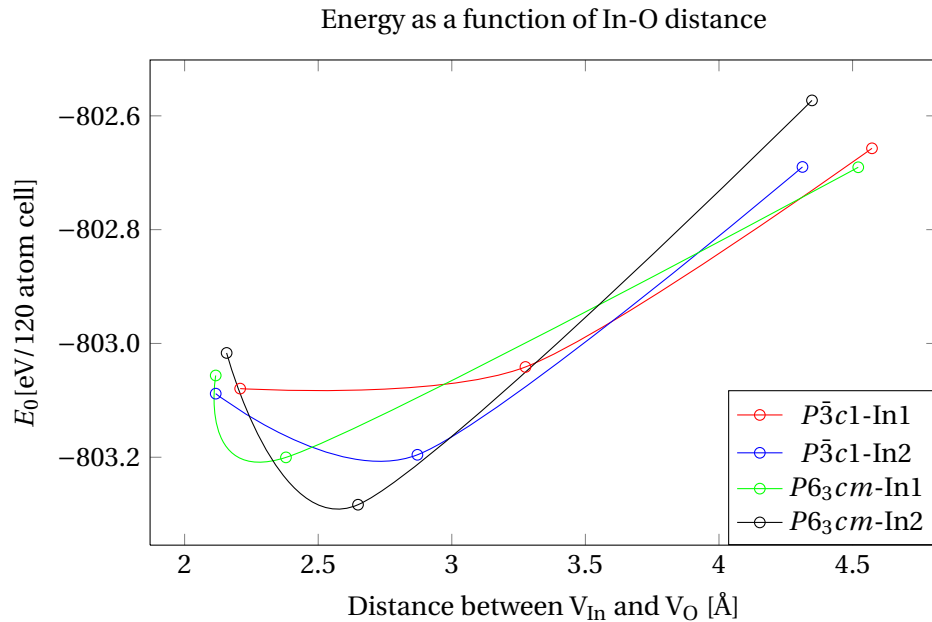


**Figure 8.1:** Plot of the ground-state energy for  $\text{InMnO}_3$  with an In-O vacancy pair against the accompanying distance between the  $V_{\text{In}}$  and  $V_{\text{O}}$ . Data taken from calculations done with fixed volume.

### 8.1.3 Energy differences for In-vacancies

Figure 7.9 shows the energy difference,  $\Delta E$ , between the polar and non-polar structure for different In-vacancies calculated by the following equation:

$$\Delta E = E_{P\bar{3}c1} - E_{P6_3cm} \quad (8.2)$$

From this figure it is observed that under oxidizing conditions the non-polar  $P\bar{3}c1$  phase is clearly favoured over the polar  $P6_3cm$  phase. This is a very interesting observation as it is the first result pointing towards the non-polar phase as the most stable structure. The compound forming with one In-vacancy is  $\text{In}_{0.958}\text{MnO}_3$ . As mentioned earlier it has been showed that  $\text{YMnO}_3$  allows high Y-deficiency, up to 15-20%[16]. In is more volatile than Y, see Table D.2, meaning In will evaporate easier than Y. This can lead to even more vacancies for  $\text{InMnO}_3$ . Both of these observations indicate that the presence of In-vacancies in  $\text{InMnO}_3$  is likely. The paraelectric behaviour in  $\text{InMnO}_3$  observed by Belik et al.[9] and Kumagai et al.[7] could therefore be a result of the formation of In-vacancies under the synthesis, making the non-polar space group the most stable structure. Belik et al.[9] synthesized  $\text{InMnO}_3$  at 1100° C. By comparing with the vapour pressure for In at 1000° C, see Table D.2, it is noted that the vapour pressure is quite high (above  $10^{-4}$ ). This means at 1100° C evaporation of In will occur, which again substantiate the paraelectric behaviour observed. In this project only one vacancy concentration of In was tested. This vacancy concentration was quite small, only 4.2%, compared to what is showed possible for  $\text{YMnO}_3$ . It would be interesting to investigate the effect of increased vacancy concentration on the stability of the polar versus the non-polar phase.

Under reducing conditions the polar structure is favoured since the most stable configuration (O-type1 oxygen vacancy) gives a positive energy difference, see Figure 7.9. This means reducing the oxygen pressure when synthesizing  $\text{InMnO}_3$  can stabilize the polar structure since possible In-O-vacancies created prefer the  $P6_3cm$ -phase. An approach would then be to control the ferroelectric versus paraelectric behaviour by changing the partial pressure of oxygen. At high  $p_{\text{O}_2}$  In-vacancies will be charge compensated by three Mn-atoms<sup>3</sup> and result in a non-polar structure. At low  $p_{\text{O}_2}$  In-vacancies will be charge compensated by one Mn-atom and a vacant oxygen leading to a polar structure.

<sup>3</sup>In section 8.3 it is shown that only one Mn-atom is oxidized.



### 8.1.4 Formation energy of defects

Figure 7.10 shows the formation energy of the most stable In-vacancy configurations plotted against the chemical potential of oxygen. An oxidizing atmosphere with high oxygen partial pressure,  $p_{O_2}$ , will favour the formation of In-vacancies. This because high  $p_{O_2}$  will move the equilibrium in equation 3.2 to the right according to Le Chatelier's principle. By looking at equation 3.6 it is noted that oxygen gas is present on the left side of the equation also for In-O-vacancy pairs. However, the amount is 1/3 of the In-vacancy case and reducing atmosphere with low oxygen partial pressure will favour In-O-vacancy pairs. It is therefore expected a higher formation energy for In-vacancies than for In-O-vacancy pairs under reducing conditions and opposite at oxidizing conditions. Figure 7.10 confirms this.

When having a mechanism designed for reducing conditions, as the formation of In-O-vacancies, it is normal to expect the formation energy to increase with increasing chemical potential of oxygen. This is not the case when observing Figure 7.10. Remember that the reducing conditions in this project are named middling reducing since the reducing conditions were too computational challenging. The middling reducing case presented requires some oxygen gas to form the In-O-vacancy pair. The slope for the formation energy of In-O-vacancy pairs is therefore slightly negative when increasing the chemical potential of oxygen. The formation energy of In-O-vacancy pairs does not turn negative in the plotted range of the chemical potential of oxygen. However, the formation energy of In-vacancies turns negative with  $\mu_O$  above -3eV. This means that under oxidizing conditions In-vacancies form spontaneously making the stoichiometric compound unstable. By looking at thermodynamic data[60] Sunde et al.[61] found that the sublimation of  $In_2O_3$  will mainly occur through the following reaction:



This means by decreasing the partial pressure of oxygen the evaporation will increase. A similar process will be present for  $InMnO_3$  and increased evaporation of In can be expected at lower  $p_{O_2(g)}$ . Since the mechanisms for the formation of In-vacancies in this project are under oxidizing and middling reducing conditions the exact connection to equation 8.3 cannot be found by comparing with Figure 7.10. However, if the mechanism for creation of In-vacancies under very reducing conditions, see equation 3.4, were used the formation energy would de-

crease with a decrease in  $\mu_O$  and  $p_{O_2(g)}$  in connection with more evaporation of In and more vacancies created.

## 8.2 Stability of the polar and non-polar phase with point defects

Figure 8.2 shows a comparison of the energy differences for different types of point defects compared to the stoichiometric energy difference between the polar and non-polar structure. In addition to data obtained in this project, data from previous work on interstitial and vacant oxygen are included[1]. The red rectangles highlight the most stable configuration of the different defects.

By observation of Figure 8.2 it is evident that different defects have different effects on the relative stability between the polar and non-polar phase of  $\text{InMnO}_3$ . Both In-vacancies in an oxidizing environment and interstitial oxygen show negative energy differences, leading to the non-polar  $P\bar{3}c1$ -structure being the most stable. For oxygen vacancies the most stable configuration leads to a small decrease of the energy difference, which indicates a disfavouring of the polar structure. For In-O vacancy pairs under reducing conditions the polar structure is clearly favoured due to almost a doubling of the energy difference between  $P\bar{3}c1$  and  $P6_3cm$ . The main conclusion drawn from this is that defect chemistry play a substantial role when looking at the stability between the two space group for  $\text{InMnO}_3$ .

### 8.2.1 Energy differences compared to experimental

Few experimental studies on  $\text{InMnO}_3$  can be found in literature, and it is therefore hard to draw exact conclusions regarding what cause the deviating properties of  $\text{InMnO}_3$ . On the other hand, a few trends are observed that root back to what are found computationally. These trends are discussed below.

As presented in Table 2.1 Huang et al. [10] showed that different cooling schemes resulted in detection of different dielectric properties for  $\text{InMnO}_3$ . The following discussion used the names listed in Table 2.1 to distinguish the different cooling paths. By slow cooling the sam-

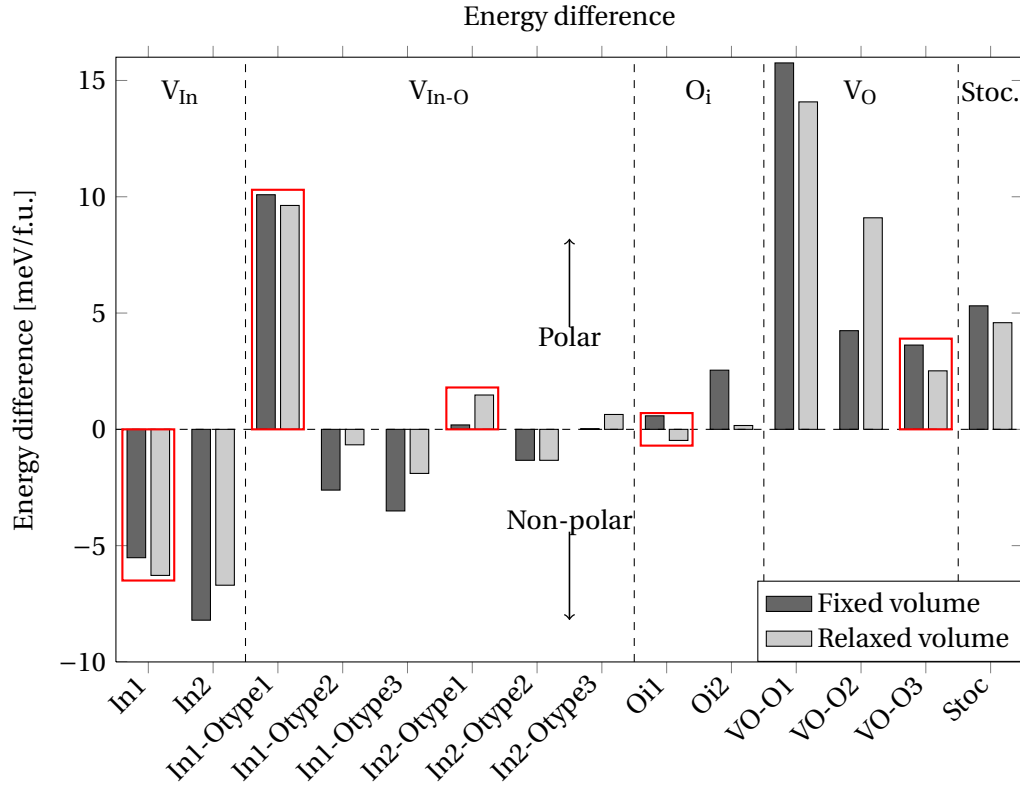


**Figure 8.2:** Comparison of the energy difference,  $\Delta E = E_{P\bar{3}c1} - E_{P6_3cm}$ , between the  $P\bar{3}c1$  and  $P6_3cm$  phase of  $\text{InMnO}_3$  for a non-stoichiometric cell with different defects and a stoichiometric cell. The red rectangles highlight the most stable configuration for each defect type. Data show calculations done with both fixed and relaxed volume.

ple, IMO-a, investigating by DF-TEM and HAADF-STEM demonstrated clear presence of ferroelectricity. Conversely, when the sample was furnace cooled<sup>4</sup> DF-TEM and HAADF-TEM showed non-polar regions embedded in a polar matrix. Compared to slow cooling furnace cooling is a much more rapid process, resembling e.g. quenching. To clarify the origin of the non-polar domains Huang et al. prepared two new samples, IMO-c and IMO-d. These were quenched from 950°C and 650°C, respectively. The sample quenched from 650°C, IMO-d, showed small vortex-antivortex domains that indicated ferroelectricity. In contrast, when the sample quenched from 950°C, IMO-c, was observed by DF-TEM no hint of vortex-type domains were found. In addition, HAADF-TEM of the IMO-c sample demonstrated down-

<sup>4</sup>Oven turned off after heating and sample was cooled inside.

no-up distortion of In, a characteristic of the non-polar  $P\bar{3}c1$ -phase, see Figure 2.3. Belik et al. [9] published a study where the samples of  $\text{InMnO}_3$  were prepared with a similar synthesis route as for Huang's experiments. However, these samples were heated to  $1100^\circ\text{C}$  and then quenched to room temperature. Ferroelectric hysteresis loop measurements at various temperatures revealed no hysteresis loops, indicating paraelectric behaviour.

When a material is quenched from a high to a low temperature, defects formed at higher temperatures are not able to diffuse out of the material during cooling. Instead they are frozen into the matrix. This can be connected to the findings by Huang et al. and Belik et al. When the samples are quenched from higher temperatures a high concentration of defects will most likely be present in the final material. Figure 8.2 shows that the most stable configuration of interstitial oxygen, vacant oxygen and In-O-vacancy pairs (not In1-Otype1) decrease the energy difference. Hence disfavours the polar phase compared to a stoichiometric sample. In addition, the presence of In-vacancies makes the non-polar phase most stable. The presence of point defects in the final sample can therefore be the explanation for the final properties of  $\text{InMnO}_3$  in Huang et al. and Belik et al. experiments. The discovery of the connection between point defects and relative stability of  $\text{InMnO}_3$  can then be used to find an appropriate synthesis route to either form paraelectric or ferroelectric  $\text{InMnO}_3$ .

### 8.2.2 Energy differences compared to temperature

The following equation describes the relationship between energy,  $E$ , and temperature,  $T$  [26]:

$$E = k_B T \quad (8.4)$$

where  $k_B$  is the Boltzmann constant (i.e.  $1.38 \cdot 10^{-23}$  J/K). Figure 8.3 shows the temperature that corresponds to the energy difference between the polar and non-polar phase. The negative temperatures are not real values. They resemble a negative energy difference favouring the non-polar structure, confer Figure 8.2. When the energy difference is equal to a temperature below 40K the energy difference is considered too small to be able to distinguish the two phases experimentally. This is the case for several of the different defect types and makes it very hard to distinguish the two phases by experimental techniques (e.g. Rietveld analysis).

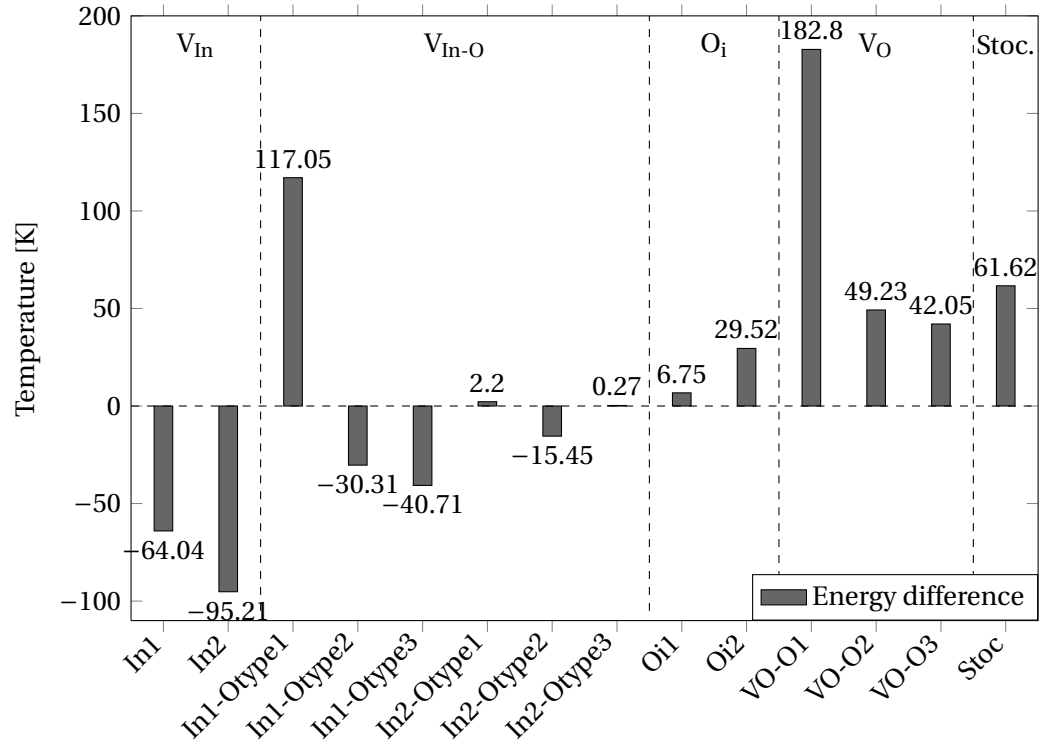
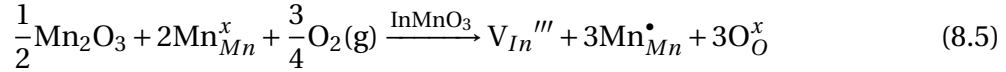


**Figure 8.3:** The equivalent temperature to the energy difference,  $\Delta E = E_{P\bar{3}c1} - E_{P6_3cm}$ , in Figure 8.2 between non-polar  $P\bar{3}c1$  and polar  $P6_3cm$  for stoichiometric and non-stoichiometric cells. The negative temperatures are not real values, but resemble a negative energy difference favouring the non-polar structure, confer Figure 8.2.

## 8.3 In-vacancies alter the insulating properties of $\text{InMnO}_3$

### 8.3.1 In-vacancies under ox. conditions lead to metallic properties

The Kröger-Vink equation was given in section 3.2.1 as the following:



The proposed equation suggest that three Mn-atoms are oxidized from  $\text{Mn}^{3+}$  to  $\text{Mn}^{4+}$ . In previous work[1] it was shown that charge compensation for oxygen vacancies and interstitial oxygen were localized on the respective Mn-atoms. Conversely, the same is not identified for In-vacancies. Listing 8.1 and 8.2 show an extract of the total charge and magnetization of each Mn-atom for different orbitals with an In-vacancy for  $P\bar{3}c1$  and  $P6_3cm$ , respectively. For  $P\bar{3}c1$  it is only atom 28 that differs significantly from the other both by looking at charge and magnetization. The same can be observed for atom 40 for  $P6_3cm$ . It seems like it is only one Mn-atom prior to three that demonstrate a clear change. A reason for this can be that the remaining charge compensation is delocalized instead of localized on the Mn-atoms. The Kröger-Vink equation should in that case be reformulated to the following:



Delocalization of electrons or holes is a characteristic of metallic behaviour. It is therefore logical to think that In-vacancies will lead to  $\text{InMnO}_3$  becoming a p-metal. This is confirmed by looking at the density of states plots for In-vacancies in  $P\bar{3}c1$  and  $P6_3cm$  under oxidizing conditions. Figure 8.4 shows an enhanced view of the density of states around the Fermi-level. The stoichiometric compound of  $\text{InMnO}_3$  is an insulator, which means it has a wide bandgap with the Fermi level placed at the top of the valence band. However, with an In-vacancy it is observed that the Fermi level lies in the valence band, making this a p-metal, see Figure 8.4. The transition between a metal and an insulator is called a Mott transition named after the researcher Sir Neville Mott[35]. Metallic behaviour of a material that from band theory is believed to be an insulator can be explained by a competition between potential and kinetic energies of the electrons. In summary, the electrons kinetic energy is lowered by delocalization and the potential energy is lowered by localization[35].

Figure 8.4 shows a comparison of the density of states plotted for a stoichiometric cell and a cell with an In-vacancy under oxidizing conditions. From this it is clear that for stoichiometric  $\text{InMnO}_3$  the Fermi level lies at the top of the valence band, which is a characteristic of an insulator. However, for a cell with an In-vacancy the Fermi level lies inside the valence band making it a p-metal. Accordingly, this supports the hypothesis that charge compensation happens by delocalized holes as suggested above. The phenomena is evident for both the polar  $P6_3cm$ -phase and the non-polar  $P\bar{3}c1$ -phase.

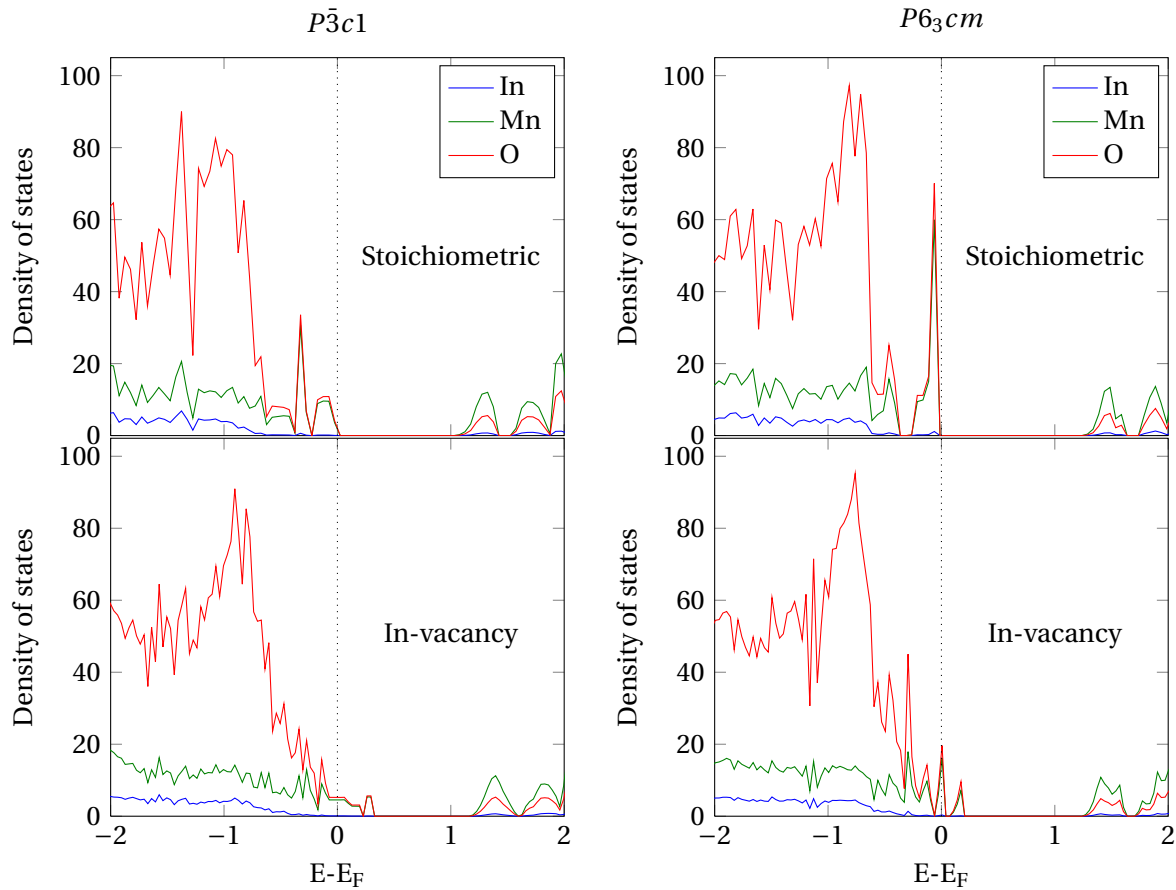


**Figure 8.4:** A comparison of the density of states around the bandgap for a stoichiometric cell and a cell with an In-vacancy for  $P\bar{3}c1$  and  $P6_3cm$ . Data taken from calculation with fixed volume.

**Listing 8.1:** Vacant indium  $P\bar{3}c1$ -In1

total charge				
# of ion	s	p	d	tot
24	2.176	6.076	4.486	12.738
25	2.176	6.077	4.493	12.746
26	2.178	6.077	4.485	12.740
27	2.174	6.074	4.493	12.741
28	2.188	6.086	4.453	12.727
29	2.176	6.076	4.485	12.738
30	2.176	6.076	4.494	12.747
31	2.174	6.073	4.494	12.741
32	2.177	6.078	4.486	12.741
33	2.178	6.078	4.489	12.745
34	2.176	6.074	4.492	12.741
35	2.179	6.076	4.486	12.740
36	2.174	6.074	4.490	12.738
37	2.176	6.077	4.481	12.734
38	2.176	6.076	4.497	12.749
39	2.174	6.073	4.492	12.739
40	2.173	6.073	4.501	12.747
41	2.175	6.074	4.493	12.741
42	2.182	6.082	4.476	12.740
43	2.177	6.076	4.486	12.738
44	2.173	6.073	4.492	12.737
45	2.177	6.076	4.493	12.747
46	2.176	6.076	4.487	12.738
47	2.175	6.075	4.487	12.737
magnetization (x)				
# of ion	s	p	d	tot
24	0.018	0.022	3.645	3.685
25	-0.018	-0.021	-3.659	-3.698
26	0.018	0.019	3.593	3.629
27	-0.018	-0.021	-3.674	-3.713
28	-0.018	-0.020	-3.435	-3.473
29	0.019	0.022	3.657	3.698
30	0.018	0.021	3.660	3.699
31	-0.017	-0.021	-3.680	-3.718
32	0.017	0.020	3.608	3.646
33	-0.018	-0.021	-3.640	-3.679
34	-0.019	-0.021	-3.679	-3.719
35	0.020	0.019	3.637	3.676
36	0.018	0.021	3.672	3.711
37	-0.017	-0.020	-3.597	-3.634
38	0.018	0.021	3.670	3.709
39	-0.018	-0.020	-3.673	-3.711
40	-0.018	-0.019	-3.669	-3.706
41	0.017	0.020	3.663	3.700
42	0.019	0.022	3.584	3.625
43	-0.019	-0.022	-3.654	-3.695
44	0.018	0.020	3.654	3.692
45	-0.019	-0.021	-3.669	-3.709
46	-0.018	-0.021	-3.646	-3.685
47	0.018	0.021	3.660	3.700

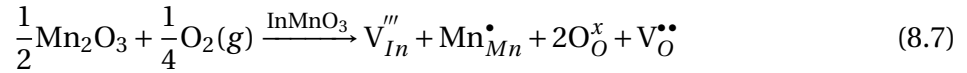
**Listing 8.2:** Vacant indium  $P6_3cm$ -In2

total charge				
# of ion	s	p	d	tot
24	2.181	6.080	4.477	12.738
25	2.173	6.074	4.493	12.740
26	2.176	6.077	4.492	12.745
27	2.176	6.075	4.492	12.742
28	2.179	6.078	4.477	12.734
29	2.182	6.081	4.473	12.737
30	2.176	6.077	4.495	12.748
31	2.174	6.074	4.494	12.742
32	2.170	6.072	4.500	12.742
33	2.177	6.078	4.492	12.747
34	2.174	6.074	4.491	12.739
35	2.176	6.074	4.488	12.738
36	2.173	6.073	4.496	12.741
37	2.175	6.075	4.501	12.750
38	2.177	6.078	4.484	12.739
39	2.176	6.075	4.489	12.741
40	2.193	6.090	4.447	12.730
41	2.173	6.075	4.499	12.747
42	2.173	6.074	4.496	12.744
43	2.173	6.073	4.498	12.744
44	2.175	6.076	4.496	12.747
45	2.175	6.076	4.489	12.740
46	2.178	6.079	4.489	12.747
47	2.172	6.073	4.495	12.740
magnetization (x)				
# of ion	s	p	d	tot
24	0.018	0.019	3.555	3.592
25	0.017	0.021	3.679	3.718
26	-0.017	-0.021	-3.651	-3.690
27	-0.018	-0.020	-3.652	-3.690
28	-0.020	-0.021	-3.633	-3.674
29	0.017	0.018	3.508	3.543
30	0.017	0.021	3.661	3.700
31	0.018	0.021	3.677	3.716
32	-0.016	-0.020	-3.674	-3.709
33	-0.016	-0.021	-3.634	-3.671
34	-0.018	-0.021	-3.667	-3.706
35	0.020	0.021	3.676	3.717
36	0.018	0.021	3.702	3.742
37	0.018	0.021	3.694	3.733
38	-0.018	-0.020	-3.591	-3.629
39	-0.017	-0.020	-3.632	-3.669
40	-0.020	-0.019	-3.400	-3.439
41	0.016	0.021	3.679	3.716
42	0.017	0.021	3.686	3.725
43	0.018	0.021	3.702	3.741
44	-0.016	-0.019	-3.614	-3.649
45	-0.017	-0.020	-3.636	-3.673
46	-0.018	-0.021	-3.623	-3.662
47	0.019	0.022	3.718	3.759



### 8.3.2 In-O vacancy pairs leads to different behaviour of polar and non-polar phase

The Kröger-Vink equation was given in section 3.2.2 as the following:



The proposed equation suggests that charge neutrality is maintained by oxidizing one Mn-atom from Mn<sup>3+</sup> to Mn<sup>4+</sup> and creating an oxygen vacancy. Listing 8.3 and 8.4 show an extract of the total charge and magnetization of each Mn-atom for different orbitals with an In-O-vacancy pair with an O-type1 oxygen position. Under oxidizing conditions the same trend was observed for  $P\bar{3}c1$  and  $P6_3cm$ . For middling reducing conditions this is not the case. Neither magnetization nor charge for  $P\bar{3}c1$  show a significant difference for the Mn-atoms, see Listing 8.3. As for oxidizing conditions delocalized holes can be expected as charge compensation instead of localized on an Mn-atom. Conversely, when looking at  $P6_3cm$  atom 40 differs considerably from the others, see Listing 8.4. This is the same atom that was affected under oxidizing conditions. It seems like the mechanism for stabilization for the polar and non-polar phase of InMnO<sub>3</sub> is not the same when both In and oxygen vacancies are present. The mechanism for  $P6_3cm$  will be as stated in section 3.2.2, but for  $P\bar{3}c1$  it will change to:

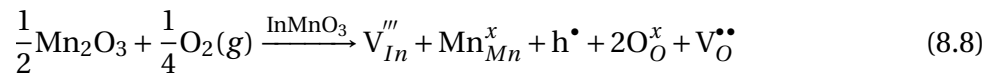


Figure 8.5 shows a comparison of the density of states around the bandgap for the different O-vacancy positions around the In-vacancy. For all O-vacancy positions in  $P\bar{3}c1$  the Fermi level lies inside the valence band, giving metallic properties. This means charge compensation has happened by delocalized holes and the Kröger-Vink equation suggested above, equation 8.8 will better describe the mechanism. By studying the density of states for different O-vacancy positions for  $P6_3cm$  it is noted that the Fermi level lies at the top of the valence band. However, for O-type1 and O-type3 it seems that an In-O-vacancy pair has induced a shallow acceptor state in the bandgap right above the valence band. The density of states plot in Figure 8.5 shows that this acceptor state has moved to below the bottom of the conduction band for O-type2 becoming a donor state. Introducing an In-O-vacancy pair in the polar InMnO<sub>3</sub> can be compared to doping the material with an impurity atom and InMnO<sub>3</sub> becomes a poor semiconductor.

**Listing 8.3:** Vacant In-O  $P\bar{3}c1$ -In1-Oypel

total charge				
# of ion	s	p	d	tot
24	2.176	6.078	4.502	12.756
25	2.176	6.078	4.504	12.758
26	2.194	6.079	4.538	12.812
27	2.176	6.077	4.502	12.754
28	2.177	6.077	4.487	12.741
29	2.177	6.077	4.486	12.740
30	2.178	6.076	4.493	12.747
31	2.176	6.075	4.494	12.744
32	2.195	6.080	4.537	12.813
33	2.177	6.079	4.502	12.758
34	2.176	6.076	4.502	12.755
35	2.176	6.077	4.502	12.755
36	2.175	6.075	4.492	12.743
37	2.175	6.076	4.491	12.742
38	2.176	6.075	4.494	12.745
39	2.175	6.073	4.496	12.744
40	2.195	6.080	4.537	12.812
41	2.177	6.077	4.502	12.756
42	2.176	6.079	4.500	12.755
43	2.176	6.077	4.500	12.752
44	2.175	6.074	4.494	12.743
45	2.177	6.075	4.494	12.746
46	2.177	6.077	4.489	12.743
47	2.177	6.077	4.487	12.741
magnetization (x)				
# of ion	s	p	d	tot
24	0.018	0.022	3.673	3.713
25	-0.017	-0.022	-3.673	-3.712
26	0.032	0.019	3.642	3.693
27	-0.018	-0.022	-3.679	-3.719
28	-0.019	-0.021	-3.624	-3.663
29	0.019	0.022	3.657	3.698
30	0.018	0.021	3.651	3.690
31	-0.018	-0.021	-3.668	-3.707
32	0.032	0.019	3.637	3.688
33	-0.017	-0.022	-3.663	-3.702
34	-0.018	-0.022	-3.687	-3.727
35	0.018	0.022	3.682	3.722
36	0.018	0.021	3.670	3.709
37	-0.017	-0.020	-3.632	-3.669
38	0.018	0.021	3.672	3.711
39	-0.018	-0.021	-3.688	-3.728
40	-0.034	-0.020	-3.664	-3.718
41	0.017	0.022	3.666	3.704
42	0.019	0.023	3.685	3.727
43	-0.019	-0.023	-3.691	-3.732
44	0.018	0.020	3.648	3.686
45	-0.019	-0.021	-3.678	-3.719
46	-0.018	-0.021	-3.649	-3.688
47	0.018	0.021	3.640	3.679

**Listing 8.4:** Vacant In-O  $P6_3cm$ -In2-Otype1

total charge				
# of ion	s	p	d	tot
24	2.194	6.080	4.535	12.810
25	2.176	6.077	4.503	12.755
26	2.176	6.077	4.503	12.756
27	2.176	6.077	4.501	12.754
28	2.176	6.077	4.502	12.754
29	2.193	6.079	4.536	12.808
30	2.176	6.079	4.503	12.758
31	2.177	6.077	4.505	12.758
32	2.193	6.079	4.536	12.808
33	2.176	6.078	4.504	12.757
34	2.176	6.077	4.501	12.754
35	2.176	6.077	4.504	12.757
36	2.174	6.074	4.498	12.745
37	2.175	6.075	4.501	12.752
38	2.174	6.076	4.493	12.743
39	2.176	6.075	4.492	12.744
40	2.192	6.089	4.452	12.732
41	2.174	6.075	4.499	12.747
42	2.174	6.075	4.497	12.747
43	2.174	6.074	4.499	12.747
44	2.173	6.074	4.501	12.748
45	2.175	6.075	4.492	12.742
46	2.177	6.078	4.495	12.750
47	2.173	6.074	4.497	12.745
magnetization (x)				
# of ion	s	p	d	tot
24	0.032	0.019	3.638	3.689
25	0.018	0.022	3.677	3.717
26	-0.018	-0.022	-3.684	-3.723
27	-0.018	-0.022	-3.672	-3.711
28	-0.019	-0.022	-3.697	-3.738
29	0.030	0.018	3.615	3.663
30	0.017	0.022	3.666	3.704
31	0.017	0.021	3.669	3.708
32	-0.032	-0.019	-3.651	-3.703
33	-0.015	-0.021	-3.659	-3.695
34	-0.017	-0.022	-3.673	-3.712
35	0.019	0.022	3.690	3.730
36	0.018	0.021	3.697	3.736
37	0.018	0.021	3.689	3.728
38	-0.017	-0.020	-3.634	-3.671
39	-0.017	-0.020	-3.641	-3.678
40	-0.020	-0.019	-3.421	-3.460
41	0.017	0.021	3.677	3.715
42	0.017	0.021	3.684	3.723
43	0.018	0.021	3.693	3.732
44	-0.016	-0.019	-3.643	-3.678
45	-0.017	-0.020	-3.646	-3.683
46	-0.018	-0.022	-3.650	-3.690
47	0.019	0.022	3.714	3.755

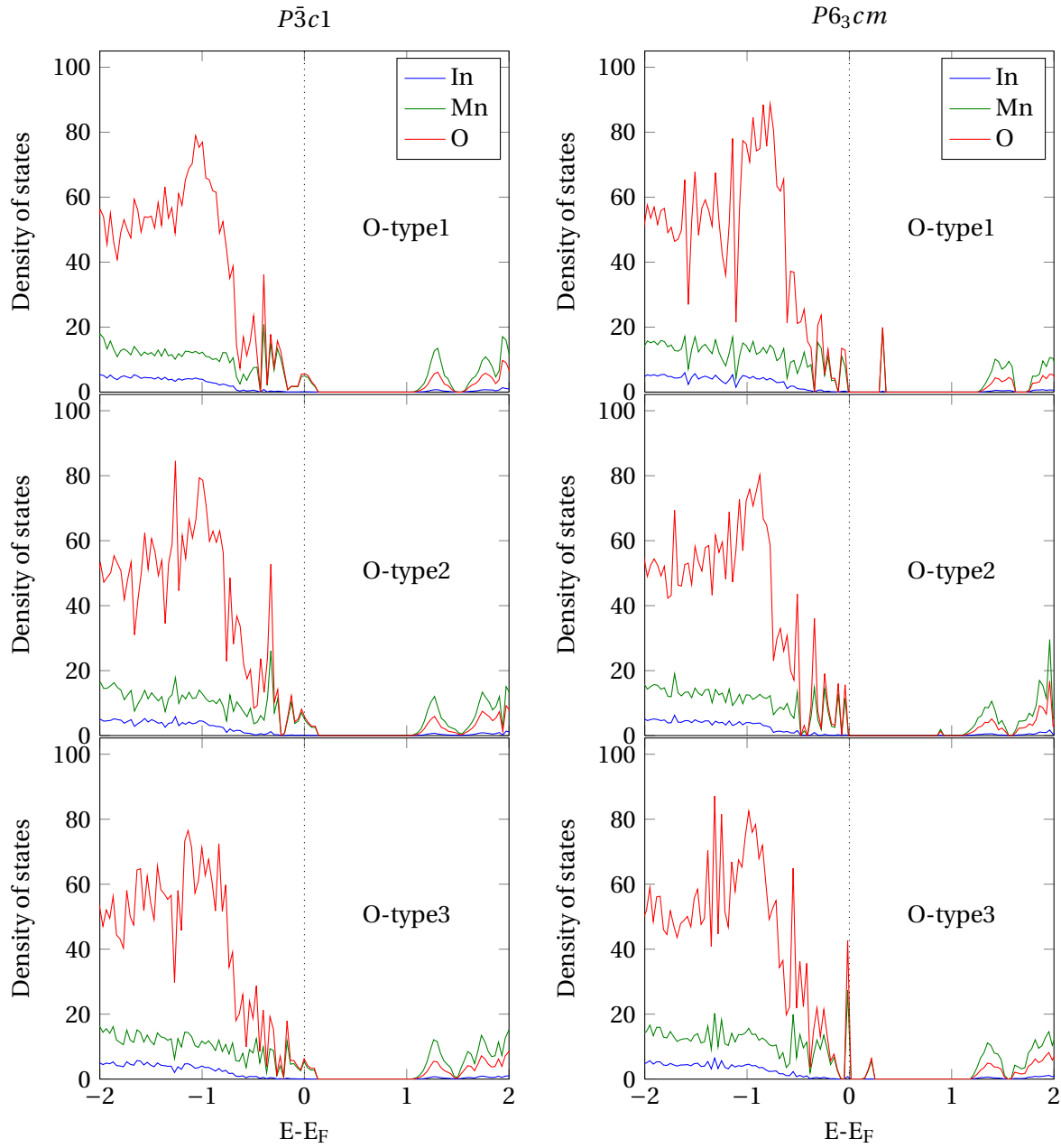


**Figure 8.5:** A comparison of the density of states around the bandgap for a cell with an In-O-vacancy pair with different O-vacancy positions for  $P\bar{3}c1$  and  $P6_3cm$ . Data taken from calculation with fixed volume.

### 8.3.3 Commercial approach and possible error

The above discussion shows that introducing In-vacancies in  $\text{InMnO}_3$  does not only affect the stability of the polar and non-polar state, but also change the metallic properties of the material. This discovery has an interesting technological area of application. By synthesizing In-deficient  $\text{InMnO}_3$  with the polar  $P6_3cm$  space group under oxidizing conditions a metallic behaviour is created. If  $\text{InMnO}_3$  with  $P6_3cm$  is synthesized under reducing condition an insulator (poor semiconductor) forms. By utilizing this thin films with conducting (metallic) and non-conducting (insulating) channels can be made. This effect can be compared to a very important technological discovery made by Albert Fert and Peter Grünberg in 1988[62], giant magnetoresistance. In brief giant magnetoresistance is when a material can switch between high and low electrical resistance by applying a magnetic field. This is used in magnetic recording systems, e.g. for data storage and retrieval in hard disk drives[63]. In theory the  $\text{InMnO}_3$  prepared with the criteria described above can be used for the same application if a sensor shifts between the conducting and non-conducting regions depending on reading zeroes or ones.

When calculations to find the ground-state energy of  $\text{InMnO}_3$  with defects were performed the criteria set, e.g. k-point density, were adjusted to an insulator. Since  $\text{InMnO}_3$  in some cases turned metallic when In-vacancies were introduced the criteria set might not be sufficient to reach convergence. To test this, one calculation was re-done with a higher k-point density ( $4 \times 4 \times 4$  for a supercell). Also, the value describing how the partial occupancies are set for each wave function was changed to an appropriate value for a metal, see the VASP manual section 7.33[52]. The calculation gave approximately the same ground-state energy and showed the same properties regarding charge compensation. This indicates that the error is most likely small. For greater accuracy the cases where  $\text{InMnO}_3$  turned into a metal should be re-calculated with higher k-point density and a different algorithm that sets the partial occupancy for each wave function.

## 8.4 Phase transition between $P\bar{3}c1$ and $P6_3cm$

To calculate the activation energy barrier between  $P\bar{3}c1$  and  $P6_3cm$  for a stoichiometric cell, a cell with an interstitial oxygen and a cell with an In-O-vacancy pair one image was not enough

to show the true energy landscape. An extra calculation with five images was therefore used to confirm the minimum energy path (MEP) in each case. Some of the results from nudge elastic band (NEB) calculations on the phase transition between the non-polar and polar phase still raise questions. No literature is published where the NEB is used on as subtle transitions as in this project. This method is usually used to calculate the MEP for e.g. diffusion of atoms. Therefore the calculations performed are also a test of NEB as a tool for calculating the phase transition between to phases, and more experience might be necessary to produce consistent results. In addition, the lattice parameters for the initial ( $P\bar{3}c1$ ) and final ( $P6_3cm$ ) state are not the same. This is also a deviation from standard use of NEB. Possible limitations connected to the use of NEB for the purpose in this project are not addressed and may clarify the unanswered questions. However, the results can be used as a tool to qualitatively analyse what happens to the activation energy barrier when defects are introduced, and then indicate how stable the different structures are against perturbations as electric fields, magnetic fields and change in stoichiometry.

#### 8.4.1 Phase transition path for a stoichiometric cell

A small activation energy barrier for the phase transition between the non-polar  $P\bar{3}c1$ -phase and polar  $P6_3cm$ -phase were detected, see Figure 7.11. A software to identify the space group (FINDSYM[55, 56]) was used on the different images. With a tolerance of 0.1 the following transition between space groups was found:  $P\bar{3}c1 \rightarrow P3c1 \rightarrow P\bar{3}c1 \rightarrow P3c1 \rightarrow P6_3cm$ , also see Figure 7.11. This is in agreement with the proposed phase transition route suggested by Cano et al.[38] and explained in section 4.4. The least energy demanding path from non-polar  $P\bar{3}c1$  to polar  $P6_3cm$  goes through the polar  $P3c1$ -structure. It is hard to explain why the  $P\bar{3}c1$  structure change into a lower energy  $P3c1$  structure before it turns back to a higher-energy  $P\bar{3}c1$  structure and lastly into the  $P6_3cm$  via the  $P3c1$  structure. As explained by Griffin[64] the tilting of the  $MnO_5$ -trigonal bipyramids characterize the different space groups.  $P6_3cm$  can have a tilt of  $30^\circ \cdot n$  where  $n$  is even,  $P\bar{3}c1$  can have a tilt of  $30^\circ \cdot n$  where  $n$  is odd and  $P3c1$  can have any tilt angle except those for  $P\bar{3}c1$  and  $P6_3cm$ , see Figure 8.6. The intermediate images made for the phase transition calculation can then meet the different tilting criteria when tilting the trigonal bipyramids from the angle in  $P\bar{3}c1$  to that of  $P6_3cm$ . Hence, lead to the transition to  $P3c1$  and back to  $P\bar{3}c1$  before reaching the final point.

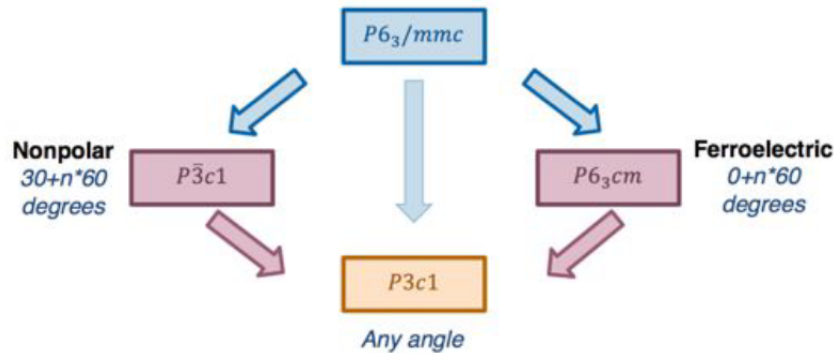


**Figure 8.6:** Graph of possible tilting options for the MnO<sub>5</sub>-trigonal bipyramids in the different subgroups of  $P6_3/mmc$ . Figure taken from the Ph.d thesis of Sinead Griffin[64].

### 8.4.2 The effect of point defects

With point defects of interstitial and vacant oxygen it is noted that the activation energy barrier increases compared to that of a stoichiometric cell, see Table 7.13. As stated, both cells with interstitial and vacant oxygen favour the polar phase. When the activation energy barrier increases with a point defect more energy is required to transform from the polar to the non-polar phase. The transition is therefore less likely to happen. In Table 8.4 the corresponding temperature to the different activation energy barriers are calculated with equation 8.4. The temperature equal to the phase transition is 62.42 K and 107.53 K for interstitial and vacant oxygen respectively. These temperatures are considered significant in terms of energy and means that InMnO<sub>3</sub> will be relative stable in the structure it has crystallized into. When an In-O-vacancy pair is introduced the activation energy barrier decreases significantly and the corresponding temperature is very low, see Table 8.4. In this case the energy required for the phase transition from polar to non-polar is relatively small and small energy contributions from the surroundings can lead to a phase transition between the polar and non-polar phase.

Figure 7.14 display a very interesting effect on the activation energy barrier when an In-vacancy is introduced into the structures. The activation energy barrier disappears with this type of defect present. This means the structure will be unstable in the polar phase, slide down the energy landscape and transform into the non-polar phase. It seems like point defects involving In-vacancies leads to a more significant change than for point defects of oxygen as it completely remove the energy barrier.

**Table 8.4:** The temperature that equals the activation energy barrier for a the transition between  $P\bar{3}c1$  and  $P6_3cm$  for a stoichiometric cell and cells with different defects.

Defect type	Position $P\bar{3}c1$	Position $P6_3cm$	Activation energy barrier [meV/f.u.]	Temp. [K]
Stoichiometric			1.783	20.69
$O_i$	In2+Otype1	In1+Otype1	5.379	62.42
$V_O$	In2	In1	9.267	107.53
$V_{In}$ -red.	Oi1	Oi1	0.771	8.94
$V_{In}$ -ox.	O1-planar	O3-planar	None	None

## 8.5 Polarization

### 8.5.1 Comparison with experimental values

The experimental values of the spontaneous polarization of  $InMnO_3$  and  $YMnO_3$  are given in Table 8.5. Belik et al.[9] reported no hysteresis loop for their measurements on polarization, indicating that  $InMnO_3$  has a net zero spontaneous polarization. Huang et al.[10] prepared different samples, see Table 2.1, and reported observation of spontaneous polarization from some of the samples, but not all. The value given in Table 8.5 is from Huang et al. studies. It is important to bear in mind that the existence of spontaneous polarization in  $InMnO_3$  is the main question in this project and the value given should therefore be taken as a tool for comparison instead of a fact.

**Table 8.5:** Experimental values for the polarization of  $YMnO_3$ [65] and  $InMnO_3$ [10].

Material	Spontaneous polarization [ $\mu C/cm^2$ ]
$YMnO_3$	5.5
$InMnO_3$	1.4

The experimental value for the polarization in  $InMnO_3$  lies in between the calculated values for a stoichiometric cell with the point charge model and Berry-Phase-model. As men-

tioned, the point charge model does not take into account the electronic contribution. The Berry-Phase-method will therefore give a more plausible result. It is important to remember that some of the samples made by Huang et al.[10] did not detect ferroelectricity. From a thermodynamic point of view a certain defect concentration will be present in the prepared  $\text{InMnO}_3$ . In addition to this Huang et al. can not be certain that their sample has not interpreted additional defects due to the preparation route. This could therefore be a reason for lower polarization. By comparing the experimental value for the polarization of  $\text{YMnO}_3$  with the calculated stoichiometric value for  $\text{InMnO}_3$  with the Berry-Phase method it lies within a reasonable range. Also the differences are quite small since polarization generally is a hard quantity to measure accurately.

### 8.5.2 Change in polarization with non-stoichiometric $\text{InMnO}_3$

The calculated polarization of  $\text{InMnO}_3$  with an In-vacancy is very low. As mentioned, see section 4.2.2, the tilting of the trigonal bipyramids is what leads to polarization and ferroelectricity in  $\text{InMnO}_3$ . It is therefore reasonable to believe that reduced tilting will also reduce the polarization. Figure 8.7 shows the structure with and without an In-vacancy. For the non-stoichiometric structure the angle between the Mn- and O-atoms (see highlighted rectangles) becomes zero. This indicates that the tilting of the  $\text{MnO}_5$ -trigonal bipyramids decreases when an In-vacancy is introduced. This is in agreement with the theory stated above. Since  $\text{InMnO}_3$  has showed to turn into a metal with an In-vacancy present it would in theory be expected to find zero net polarization[66]. Since the point charge model gives an inaccurate approximation to the polarization by excluding the electronic contributions it might be that the polarization should have been zero. However, in 1965 Anderson et al.[67] predicted that in theory a ferroelectric metal can exist. The ferroelectricity arises from a ferroelectric-like structural transition that occur in the metal[66]. If  $\text{InMnO}_3$  turns into a ferroelectric metal it means that a net polarization can be found. Further investigations have to be carried out to answer this question with certainty.

When an oxygen vacancy is introduced in the structure the polarization increases. This is shown by calculation done by both the point charge model and the Berry-Phase model. The framed part of Figure 8.8 shows that with an oxygen vacancy an increased shift along the c-



axis in the In-layer occur. As explained with Figure 2.3 the displacement of In in the In-layer contributes to the total dipole moment in the  $P\bar{3}c1$ -phase. Therefore the increased displacement caused by an oxygen vacancy is most likely the reason for increased polarization.

The presence of interstitial oxygen increases the polarization when calculated by the point charge model, but decreases the polarization with the Berry-Phase model. Berry-Phase calculations are the most accurate and therefore considered further. The change in polarization compared to the stoichiometric case is quite small and clear evidence on structural changes are not detected when investigating the structure. The topic is therefore not elaborated more in this project. With In-O-vacancy pairs the polarization increases compared to the stoichiometric compound. The increase is quite small compared to for instance the change in polarization with an oxygen vacancy present. A possible explanation for this is that the effect of removing oxygen exceeds that of creating an In-vacancy resulting in a net increase of the polarization.

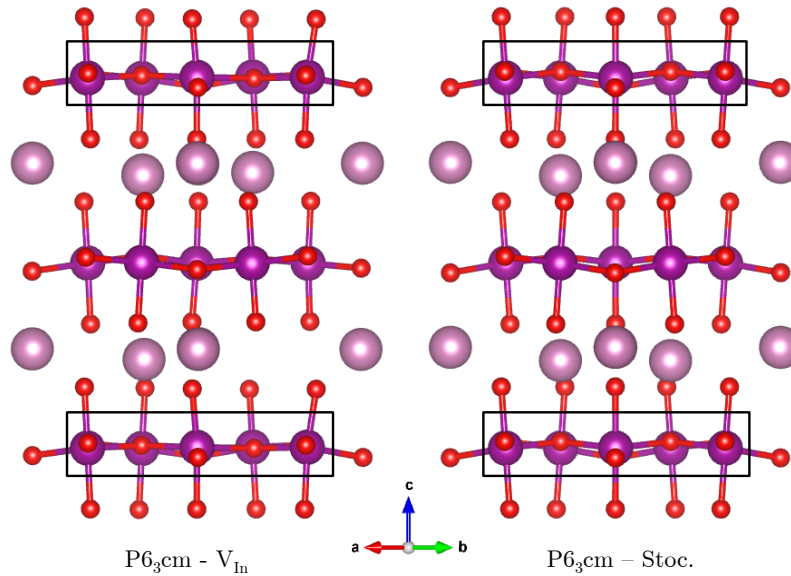


**Figure 8.7:** Comparison of a relaxed  $P6_3cm$ -cell (fixed volume) with an In-vacancy and a stoichiometric cell. The highlighted areas inside the rectangles emphasize the change in bond angle from a few degrees to zero degrees, showing that the tilting decreases with an In-vacancy.

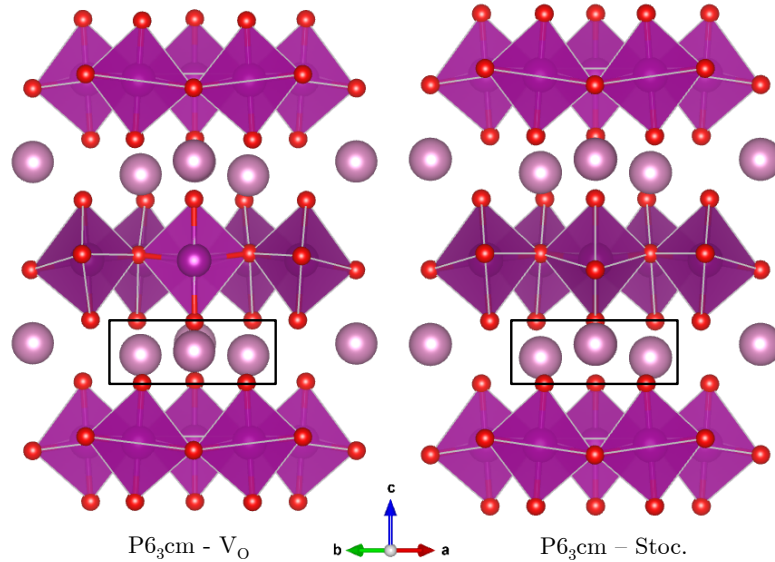


**Figure 8.8:** Comparison of a relaxed  $P6_3cm$ -cell (fixed volume) with an oxygen vacancy and a stoichiometric cell. The highlighted areas inside the rectangles emphasize the change in the In-displacement along the c-axis, showing that the polarization increase with an oxygen vacancy.

### 8.5.3 Effect of volume on polarization

When using DFT it is hard to reproduce the exact experimental value for volume. By convergence testing, parameter fitting and the use of PBEsol as the exchange correlation functional the calculations are optimized to get as close to the "real" volume as possible. Research have showed that pressure can change the ferroelectric property of a material. Sani et al.[68] showed that the spontaneous polarization decreased with increasing pressure for the ferroelectric perovskite  $\text{PbTiO}_3$ . Increased pressure will result in a volume contraction for the unit cell. The question is then if the artificial cell volume from DFT calculations can give a wrong interpretation of the polarization and relative phase stability. To give an indication on this a 30 atom unit cell of  $P\bar{3}c1$  and  $P6_3cm$  were fully relaxed (relaxed volume) with experimental positions and lattice parameters from Kumagai et al.[7]. Then the lattice parameters of  $P\bar{3}c1$  and  $P6_3cm$  were switched and fully relaxed again. The energy differences between relaxing with correct and switched lattice parameters were 1.83 meV/f.u. and 2.5 meV/f.u for  $P\bar{3}c1$  and  $P6_3cm$  respectively. Compared to the other energy differences discussed throughout this project the energy differences due to volume are quite significant, and could affect

the result in a larger extent than expected. Regarding the influence of volume on polarization for  $\text{InMnO}_3$  it is important to mark the difference between a hexagonal manganite and a perovskite. Sani et al. observed that the polar c-axis experienced a larger contraction with increasing pressure than the ab-plane, while the opposite was found by Gao et al.[69] for  $\text{YMnO}_3$ . Polarization in perovskites and hexagonal manganites are driven by different mechanisms and cannot be directly compared, but rather give an indication of a problem that can be relevant for  $\text{InMnO}_3$  as well.

## 8.6 Further work

Throughout this project it has been shown that point defects have an important effect on the stability between the polar and non-polar phase of  $\text{InMnO}_3$ . Point defects affect the activation energy barrier between the polar and non-polar state, the dielectric properties as well as the polarization of  $\text{InMnO}_3$ . It is clear that point defects have a significant impact on the properties of  $\text{InMnO}_3$ , and can probably resolve some of the confusion in literature. However, this project only takes a computational approach to the problem. As a consequence, a few topics for further work are suggested:

- Experimental verification
- Computational verification
- Study magnetism and phonon spectre
- Mn-atom on In-position

### 8.6.1 Experimental verification

It would be of great interest to investigate the effect of point defects on the phase stability in  $\text{InMnO}_3$  experimentally. In section 3.8 several arguments against an experimental approach are listed. Since a computational study is an approximation of the real world experimental verification is important. The experimental techniques listed below are examples of what could be used:

**SHG** Secondary harmonic generator measurements can be used to measure the polarization in  $\text{InMnO}_3$ . By making non-stoichiometric samples of  $\text{InMnO}_3$  the effect of point defects on the polarization can be studied.

**PFM** Piezoresponse force microscopy can be used for imaging ferroelectric domain patterns[70]. PFM reveals the direction of the polarization in each domain and can be used for the same purpose as SHG, i.e. verify the change in polarization with the presence of point defects. In addition it can be used to study domains and domain walls.

**TEM** Transmission electron microscopy of a polished single crystal with controlled cation stoichiometry could give interesting information. However, as mentioned in section 3.8 TEM only detects periodicity and the periodicity of defects might be too small to detect. In addition it is important to remember that TEM is based on shooting electrons onto the sample. This might destroy the sample, especially when small variations such as point defects are studied.

### 8.6.2 Computational verification

The criteria and parameters in this project are chosen to give convergence of a stoichiometric cell with as low computational effort as possible. From testing of the force criterion, section 6.1.2, interstitial oxygen in  $P\bar{3}c1$  showed an oscillating trend. It could be that with defects the force criterion should be stricter than for a stoichiometric cell in order to reach complete convergence. Also when testing the force criterion the difference between a force criterion of -0.05 eV and -0.01 eV was 1-2 meV/30 atom cell (0.17-0.33meV/f.u.), see section 6.1.2. This energy difference was considered negligible and a force criterion of -0.05 eV was chosen to be sufficient. However, some of the activation energy barriers and energy differences between polar and non-polar are in close proximity to the force criterion energy difference and is a possible source of error. Calculations with a smaller force criterion should therefore be performed to assure that the calculations are fully converged. A lower force criterion will give a substantial increase in the computational time for one relaxation. As a consequence only one configuration of each defect should be tested to verify.

Since  $\text{InMnO}_3$  turned into a metal when In-vacancies were introduced calculations with increased k-point density and different algorithm to set the partial occupancy for each wave

function, as discussed in Section 8.3.3, should be performed. New density of states calculations should also be performed. In this project a In-deficiency of only 4.2% is tested. However, it has been shown that a substantial larger Y-deficiency for  $\text{YMnO}_3$  is possible[16]. A study of the effect on the stability of the polar and non-polar phase for  $\text{InMnO}_3$  with increased In-deficiency will therefore be interesting.

### 8.6.3 Phonon spectra and magnetism

A study on phonons can reveal if the material has relaxed into a ground-state or if it is unstable with regards to displacements of ions. Figure 8.9 shows the phonons connecting the different space groups in  $\text{InMnO}_3$ [64]. Calculations of the phonon spectre for  $\text{InMnO}_3$  will give more information on the stability of the polar and non-polar phase. To do the calculations  $2 \times 2 \times 2$  supercells have to be made from the original cell. Also the convergence of the force criterion has to be very strict for phonon calculation. Therefore a 240 atom cells from a  $2 \times 2 \times 2$  supercell based on a 30-atom unit cell is the only realistic considering the computational effort.

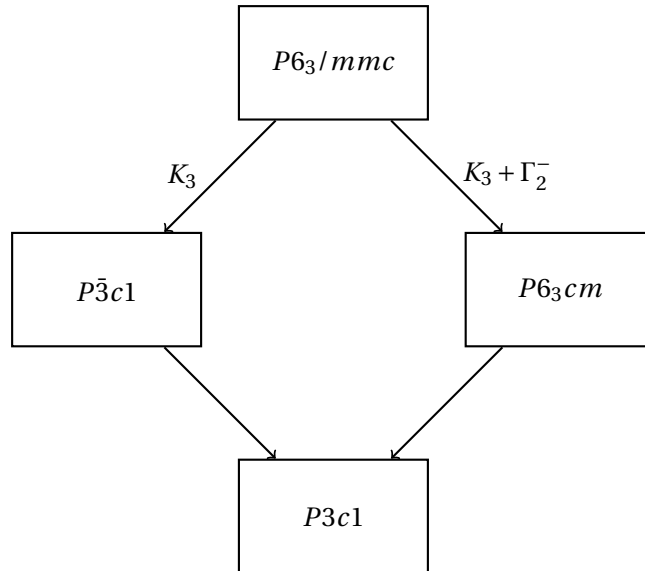


**Figure 8.9:** Representation of the relationship and phonon modes between the space groups  $P\bar{3}c1$ ,  $P6_3cm$  and  $P3c1$ .  $P3c1$  is a subgroup of  $P\bar{3}c1$  and  $P6_3cm$ . The relationships are found from Bilbao Crystallographic Server[37] and phonon modes from work by Griffin et al.[64].

It would be of interest to investigate the effect of different point defects on the magnetic property of the polar and non-polar phase of  $\text{InMnO}_3$ . In the research community the findings of

a ferromagnetic and ferroelectric material is of great interest for use in technological applications. InMnO<sub>3</sub> is found to be antiferromagnetic. However, this project has shown that point defects can dramatically alter the dielectric properties of InMnO<sub>3</sub>. This indicates that point defects have an important impact on the functional properties of InMnO<sub>3</sub> and might also alter the magnetic property. A DFT-study of the effect of point defect on the magnetization may reveal other properties of InMnO<sub>3</sub>.

#### 8.6.4 Mn-vacancies and other point defects

One other type of point defect that is likely to occur is substitution of Mn at an In-position. Table 8.6 shows the Shannon radii for different valence state of In and Mn. By comparing the ionic radii of trivalent In and Mn with coordination number six it is noted that Mn<sup>3+</sup> is smaller than In<sup>3+</sup>. Mn<sup>3+</sup> will therefore fit at a vacant In-position. The difference in radii for divalent Mn and trivalent In is small and substitution of Mn on In-position will also be likely in this case. Different intrinsic point defects have through this project showed to be very important when discussing the relative stability of the polar versus non-polar phase of InMnO<sub>3</sub>. Griffin et al.[64] were able to tune between the ferroelectric and non-polar state through Ga doping at Mn-position in a hexagonal manganite. This indicates that substitution or doping also is important. It would therefore be of interest to see if also defects from substitution of Mn at an In-position will explain the deviating properties found in literature to a larger extent.

**Table 8.6:** Shannon radii for different valence state of In and Mn[59].

Atom	Coordination number	Ionic radii [Å]
In <sup>3+</sup>	6	0.8
Mn <sup>2+</sup> -HS <sup>5</sup>	6	0.83
Mn <sup>3+</sup> -HS	6	0.645

## Chapter 9

# Conclusion

The purpose of this project was to investigate the effect of point defects on the stability of the ferroelectric,  $P6_3cm$ , versus the paraelectric,  $P\bar{3}c1$ , phase of  $\text{InMnO}_3$  through a first-principles study using density functional theory. The ground-state energy for both space groups with defects are found, the phase transition between non-polar  $P\bar{3}c1$  and polar  $P6_3cm$  was investigated and the effect of point defects on the polarization of  $P6_3cm$  was studied.

In-vacancies under oxidizing conditions were found to favour the non-polar  $P\bar{3}c1$ -phase over the polar  $P6_3cm$ -phase. This is the first result of non-stoichiometry leading to favouritism of the paraelectric phase. The study showed that In-vacancies under oxidizing conditions alter the dielectric property of  $\text{InMnO}_3$  and turns insulating  $\text{InMnO}_3$  into a metal. Charge compensation was found to not obey the suggested Kröger-Vink equation. Instead charge compensation happened by delocalized holes, supporting the observation of metallic properties. In-vacancies created in a reducing environment showed favouritism of the polar  $P6_3cm$  structure. However, the energy difference between the polar and non-polar phase was subtle for several positions, and the two phases were almost equally stable in these cases. For polar  $P6_3cm$  the charge compensation was as expected and the material stayed insulating. In contrast, In-vacancies under red. conditions lead to charge compensation by holes and non-polar  $P\bar{3}c1$  turned into a metal.

The phase transition study revealed an activation energy barrier between stoichiometric  $P\bar{3}c1$  and  $P6_3cm$ . This energy barrier increased with point defects of interstitial and vacant oxygen present. Conversely, In-vacancies at reducing conditions decreased the energy barrier and for In-vacancies at oxidizing conditions it disappeared. The polarization of  $P6_3cm$  increased with point defects of vacant oxygen and decreased substantially with In-vacancies present. The study has shown the great importance of point defects for the stability of the two phases in  $\text{InMnO}_3$ , and increased the understanding of the deviating properties of  $\text{InMnO}_3$  found in literature.





# Bibliography

- [1] M. Reidulff. The effect of point defects on the polar and non-polar phases of hexagonal InMnO<sub>3</sub>. Technical report, Norwegian University of Science and Technology, 2014.
- [2] W. Eerenstein, N. D. Mathur, and J. F. Scott. Multiferroic and magnetoelectric materials. *Nature*, 442(7104):759–65, 2006.
- [3] S. Remsen and B. Dabrowski. Synthesis and Oxygen Storage Capacities of Hexagonal Dy(1-x)Y(x)MnO(3+δ). *Chemistry of Materials*, 23(17):3818–3827, 2011.
- [4] S. M. Griffin, M. Lilienblum, K. T. Delaney, Y. Kumagai, M. Fiebig, and N. A. Spaldin. Scaling Behavior and Beyond Equilibrium in the Hexagonal Manganites. *Phys. Rev. X*, 2(4), 2012.
- [5] H. L. Yakel Jnr, W. C. Koehler, E. F. Bertaut, and E. F. Forrat. On the crystal structure of the manganese(III) trioxides of the heavy lanthanides and yttrium. *Acta. Cryst.*, 16(10):957–962, 1963.
- [6] G. a. Smolenskii and V. a. Bokov. Coexistence of Magnetic and Electric Ordering in Crystals. *J. Appl. Phys.*, 35(3):915, 1964.
- [7] Y. Kumagai, A. A. Belik, M. Lilienblum, N. Leo, M. Fiebig, and N. A. Spaldin. Observation of persistent centrosymmetry in the hexagonal manganite family. *Phys. Rev. B*, 85(17), 2012.
- [8] J. E. Greedan, M. Bieringer, J. F. Britten, D. M. Giaquinta, and H. C. Zurloye. Synthesis, crystal-structure, and unusual magnetic-properties of InMnO<sub>3</sub>. *Jour. of Solid State Chemistry*, 116(1):118–130, 1995.
- [9] A. Belik, S. Kamba, M. Savinov, D. Nuzhnyy, M. Tachibana, E. Takayama-Muromachi, and V. Goian. Magnetic and dielectric properties of hexagonal InMnO<sub>3</sub>. *Phys. Rev. B*, 79(5), 2009.
- [10] F. T. Huang, X. Wang, Y. S. Oh, K. Kurushima, S. Mori, Y. Horibe, and S. W. Cheong. Delicate balance between ferroelectricity and antiferroelectricity in hexagonal InMnO<sub>3</sub>. *Phys. Rev. B*, 87(18), 2013.

- [11] K. Momma and F. Izumi. VESTA 3 for three-dimensional visualization of crystal, volumetric and morphology data. *J. Appl. Cryst.*, 44:1272–1276, 2011.
- [12] J.-H. Lee, S. Song, M.-A. Oak, and H. M. Jang. Polar P63cm phase as a marginally stable ground-state structure of InMnO<sub>3</sub>: First-principles study. *EPL (Europhysics Letters)*, 104(5):57001, 2013.
- [13] A. Kelly and K.M Knowles. *Crystallography and Crystal Defects*. Wiley, 2nd edition, 2012.
- [14] P. Atkins, T. Overton, J. Rourke, M. Weller, and F. Armstrong. *Shriver & Atkins' Inorganic Chemistry*. Oxford, 5th edition, 2010.
- [15] A. R. West. *Basic Solid State Chemistry*. Wiley, 2nd edition, 2000.
- [16] M. M. Frydenlund. Development of a new class of oxygen ion mixed conductors. Technical report, Norwegian University of Science and Technology, 2014.
- [17] G. Aylward and T. Findlay. *SI Chemical Data*. Wiley, 6th edition, 2008.
- [18] C. Freysoldt, B. Grabowski, T. Hickel, J. Neugebauer, G. Kresse, A. Janotti, and C. G. Van de Walle. First-principles calculations for point defects in solids. *Rev. of Modern Physics*, 86(1):253–305, 2014.
- [19] Y. Kumagai and F. Oba. Electrostatics-based finite-size corrections for first-principles point defect calculations. *Phys. Rev. B*, 89(19):15, 2014.
- [20] P. Papon, S. L. Schnur, J. Leblond, and P. H. E. Meijer. *The Physics of Phase Transitions: Concepts and Applications*. Springer-Verlag, 2007.
- [21] S. Stoelen and T. Grande. *Chemical Thermodynamics of Materials - Macroscopic and Microscopic Aspects*. Wiley, 1st edition, 2005.
- [22] C. Fennie and K. Rabe. Ferroelectric transition in YMnO<sub>3</sub> from first principles. *Phys. Rev. B*, 72(10):100103, 2005.
- [23] Y. Kumagai and N. A. Spaldin. Structural domain walls in polar hexagonal manganites. *Nature Communication*, 4:1540, 2013.

- [24] M. De Graef and M. E. McHenry. *Structure of Materials - An introduction to crystallography, diffraction, and symmetry*. Cambridge, 1st edition, 2007.
- [25] E. J. Williams W. L. Bragg. The Effect of Thermal Agitation on Atomic Arrangement in Alloys. II. *Proceedings of The Royal Society A: Mathematical, Physical and Engineering Sciences*, 151:540 – 566, 1935.
- [26] P. Atkins and J. Paula. *Atkins' Physical Chemistry*. Oxford, 9th edition, 2010.
- [27] J. Kim, Y. M Koo, K.-S. Sohn, and N. Shin. Symmetry-mode analysis of the ferroelectric transition in YMnO<sub>3</sub>. *Appl. Phys. Lett.*, 97(9):092902, 2010.
- [28] A. S. Gibbs, K. S. Knight, and P. Lightfoot. High-temperature phase transitions of hexagonal YMnO<sub>3</sub>. *Phys. Rev. B*, 83(9):094111, 2011.
- [29] S. Artyukhin, K. T. Delaney, N. A. Spaldin, and M. Mostovoy. Landau theory of topological defects in multiferroic hexagonal manganites. *Nat. Matr.*, 13(1):42–49, 2014.
- [30] A. P. Levanyuk and D. G. Sannikov. Improper ferroelectrics, 1974.
- [31] M. Stengel, C. J. Fennie, and P. Ghosez. Electrical properties of improper ferroelectrics from first principles. *Phys. Rev. B*, 86(9):094112, 2012.
- [32] N. A. Spaldin. A beginner's guide to the modern theory of polarization. *Jour. of Solid State Chemistry*, 195:2–10, 2012.
- [33] R. Resta and D. Vanderbilt. Theory of Polarization : A Modern Approach. *Physics of ferroelectrics: A modern perspective*, 105:31–68, 2007.
- [34] R. Tilley. *Understanding Solids - The Science of Materials*. Wiley, 2004.
- [35] S. Elliot. *The Physics and Chemistry of Solids*. Wiley, 2nd edition, 2000.
- [36] A. Stevenson. Oxford Dictionary of English Press, 2010.
- [37] S. Ivantchev and E. Kroumova. SUBGROUPGRAPH: a computer program for analysis of group-subgroup relations between space groups. *J. Appl. Cryst.*, (33):1190–1191, 2000.
- [38] A. Cano. Hidden order in hexagonal RMnO<sub>3</sub> multiferroics. *Phys. Rev. B*, 89(21), 2014.

- [39] D. Sholl and J. A. Steckel. *Density functional theory: a practical introduction*. John Wiley & Sons, 2011.
- [40] J. G. Lee. *Computational Materials Science - An Introduction*. CRC Press, 1st edition, 2012.
- [41] J. Pade. *Quantum Mechanics for Pedestrians 1: Fundamentals*. Springer International Publishing, 2013.
- [42] M. Born and R. Oppenheimer. On the Quantum Theory of Molecules. *Annalen der Physik*, 84:457, 1927.
- [43] See [http://www.ulb.ac.be/cpm/people/scientists/bsutclif/bornopn\\_corr.pdf](http://www.ulb.ac.be/cpm/people/scientists/bsutclif/bornopn_corr.pdf) for an English translation language translation of the original paper.
- [44] P. Hohenberg. Inhomogeneous Electron Gas. *Phys. Rev.*, 136(3B):B864–B871, 1964.
- [45] W. Kohn and L. J. Sham. Self-Consistent Equations Including Exchange and Correlation Effects. *Phys. Rev.*, 140(4A):A1133–A1138, 1965.
- [46] J. Perdew, A. Ruzsinszky, G. Csonka, O. Vydrov, G. Scuseria, L. Constantin, X. Zhou, and K. Burke. Restoring the Density-Gradient Expansion for Exchange in Solids and Surfaces. *Phys. Rev. Lett.*, 100(13):136406, 2008.
- [47] R. P. Feynman. Forces in Molecules. *Phys. Rev.*, 56(4):340–343, 1939.
- [48] H. Jonsson, G. Mills, and K. W. Jacobsen. *Classical and Quantum Dynamics in Condensed Phased Simulations: Proceedings of the International School of Physics "Computer Simulation of Rare Events and Dynamics of Classical and Quantum Condensed-Phased Systems": Lerici, Villa Marigola, 7 July-18 July*. World Scientific, 1998.
- [49] G. Henkelman, B. P. Uberuaga, and H. Jonsson. A climbing image nudged elastic band method for finding saddle points and minimum energy paths. *Jour. of Chem. Phys.*, 113(22):9901, 2000.
- [50] R. D. King-Smith and D. Vanderbilt. Theory of polarization of crystalline solids. *Phys. Rev. B*, 47(3):1651–1654, 1993.

- [51] R. M. Martin. *Electronic Structure: Basic Theory and Practical Methods*. Cambridge University Press, 2004.
- [52] G. Kresse, M. Marsman, and J. Furthmüller - <http://cms.mpi.univie.ac.at/vasp/vasp/vasp.html>. VASP the GUIDE (VASP manual).
- [53] Henkelman - <http://theory.cm.utexas.edu/vtsttools/index.html>. VTST-Tools.
- [54] A. Shigemi and T. Wada. Evaluations of Phases and Vacancy Formation Energies in KNbO<sub>3</sub> by First-Principles Calculation. *Japanese Journal of Applied Physics*, 44(11):8048–8054, 2005.
- [55] H. T. Stokes and D. M. Hatch. FINDSYM: Program for identifying the space-group symmetry of a crystal. *J. Appl. Cryst.*, 38(1):237–238, 2005.
- [56] Iso.byu.edu. ISOTROPY Software Suite.
- [57] C. Zhang, X. Zhang, Y. Sun, and S. Liu. Atomistic simulation of Y-site substitution in multiferroic h-YMnO<sub>3</sub>. *Phys. Rev. B*, 83(5), 2011.
- [58] B. J. Alder and T. E. Wainwright. Studies in Molecular Dynamics. I. General Method. *Jour. of Chem. Phys.*, 31(2):459, 1959.
- [59] R. D. Shannon. Revised Effective Ionic Radii and Systematic Studies of Interatomic Distances in Halides and Chalcogenides. *Acta. Cryst.*, 32:751, 1976.
- [60] R. H. Lamoreaux, D. L. Hildenbrand, and L. Brewer. High-Temperature Vaporization Behavior of Oxides II. Oxides of Be, Mg, Ca, Sr, Ba, B, Al, Ga, In, Tl, Si, Ge, Sn, Pb, Zn, Cd and Hg. *Jour. of Chem. Phys.*, 16:419–43, 1987.
- [61] T. Sunde, M.-A. Einarsrud, and T. Grande. Solid state sintering of nano-crystalline indium tin oxide. *Jour. of the European Ceramic Society*, 33(3):565–574, 2013.
- [62] M.N. Baibich, J.M. Broto, A. Fert, N. Dau, F. Petroff, P. Eitenne, G. Creuzet, A. Friederich, and J. Chazalas. Giant Magnetoresistance of (001)Fe/(001)Cr Magnetic Superlattices. *Phys. Rev. Lett.*, 61(21):2472–2475, 1988.

- [63] C.H. Tsang, R. E. Fontana, T. Lin, and D.E. Heim. Design, fabrication and performance of spin-valve read heads for magnetic recording applications. *IBM Journal of Research and Development*, 42:103, 1998.
- [64] S. M. Griffin. *From the early universe to the Hubbard Hamiltonian in the hexagonal manganites*. PhD thesis, ETH Zurich, 2014.
- [65] Bas B Van Aken, Thomas T M Palstra, Alessio Filippetti, and Nicola a Spaldin. The origin of ferroelectricity in magnetoelectric YMnO<sub>3</sub>. *Nat. Mater.*, 3(3):164–70, 2004.
- [66] Y. Shi, Y. Guo, X. Wang, A. J. Princep, D. Khalyavin, P. Manuel, Y. Michiue, A. Sato, K. Tsuda, S. Yu, M. Arai, Y. Shirako, M. Akaogi, N. Wang, K. Yamaura, and A. T. Boothroyd. A ferroelectric-like structural transition in a metal. *Nat. Mater.*, 12(11):1024–7, 2013.
- [67] P. W. Anderson and E. I. Blount. Symmetry Considerations on Martensitic Transformations: Ferroelectric metals? *Phys. Rev. Lett.*, 14(7):217–219, 1965.
- [68] A. Sani, M. Hanfland, and D. Levy. Pressure and Temperature Dependence of the Ferroelectric–Paraelectric Phase Transition in PbTiO<sub>3</sub>. *Jour. Solid State Chemistry*, 167(2):446–452, 2002.
- [69] P. Gao, Z. Chen, T. A. Tyson, T. Wu, K. H. Ahn, Z. Liu, R. Tappero, S. B. Kim, and S.-W. Cheong. High-pressure structural stability of multiferroic hexagonal RMnO<sub>3</sub> (R=Y, Ho, Lu). *Phys. Rev. B*, 83(22):224113, 2011.
- [70] E. Soergel. Piezoresponse force microscopy (PFM). *Jour. of Phys. D: Applied Physics*, 44(46):464003, 2011.
- [71] A. M. Kalashnikova and R. V. Pisarev. Electronic structure of hexagonal rare-earth manganites RMnO<sub>3</sub>. *Jetp Letters*, 78(3):143–147, 2003.
- [72] D. R. Lide. *CRC Handbook of Chemistry and Physics*, 85th Edition, 2005.

# Appendix A

## VASP

### A.1 Input-files

This section displays and explains important input files for VASP.

#### A.1.1 INCAR

Listing A.1 displays an INCAR file used for relaxation of a supercell with one In-vacancy under oxidizing conditions. The important tags that distinguish calculations for InMnO<sub>3</sub> with defects from general calculations are:

**Spin-polarization:** It is necessary to define the spin state for each Mn-atom. This is done in the tag MAGMOM. (+) is spin up and (-) is spin down.

**Band gap:** To better represent the experimental value of the band gap the LDAU tag is set.

#### Listing A.1: INCAR file

```
system      = InMnO3
%Cut-off energy
PREC        = Normal
ENCUT       = 550
%Convergence criteria
NSW         = 80
NELMIN      = 6
NELM        = 120
EDIFFG      = -0.05
EDIFF       = 1E-08
%How to relax the cell
ISIF        = 2
IBRION      = 2
%INPUT- and OUTPUT-files
LCHARG      = .FALSE.
LORBIT      = 10
%Spin-polarization
ISPIN       = 2
MAGMOM      = 23*0 5 -5 5 -5 -5 5 5 -5 5 -5 -5 5 5 -5 5 -5 -5 5 5 -5 5 -5 5 72*0
```

```

%L(S)DA+U
LDAU      = .TRUE.
LDAUTYPE  = 2
LDAUL     = -1 2 -1
LDAUU     = 0 5 0
LDAUJ     = 0 0 0
LDAUPRINT = 2
%Calculation parameters
GGA       = PS
LREAL     = Auto
ISMEAR    = 0
SIGMA     = 0.01
LASPH     = .TRUE.
LMAXMIX   = 4
NPAR      = 4
NSIM      = 4

```

### A.1.2 POSCAR

The file shown in A.2 shows some of the first rows of the POSCAR-file for a supercell. Line 2-4 gives the length of the a, b and c-vectors, line 5-6 gives the atoms involved and how many there exist for each type. The lines from 8 and down give the position for each atom in the cell (this part continues until the positions of all the 120 atoms are listed). The POSCAR-files are made by building the desired structure in VESTA (Visualization for Electronic Structural Analysis[11]) and exporting the structure to POSCAR format.

**Listing A.2:** POSCAR file. Only the first 11 lines are shown. The file continues until the positions of all the atom in the cell are given.

```

InMnO3      1.0
  11.8280528369505000    0.0000000000000000    0.0000000000000000
  -5.9140264184752500   10.2433942341037000    0.0000000000000000
   0.0000000000000000    0.0000000000000000   11.4686954886538732
In  Mn  O
24  24  71
Direct
  0.0000000000000000    0.0000000000000000    0.2724904225926252
  0.5000000000000000    0.0000000000000000    0.2724904225926252

```

### A.1.3 KPOINTS

The KPOINTS-file describes the k-mesh for the calculation. For calculations on unit cells a 4x4x2 k-mesh are used, see Listing A.3. For calculations on 2x2x1 supercells a 2x2x2 k-mesh



are used, see Listing A.4.

**Listing A.3:** KPOINTS file for unit cell calculations

```
Automatic mesh
0
Gamma
  4  4  2
  0. 0. 0.
```

**Listing A.4:** KPOINTS file for supercell calculations

```
Automatic mesh
0
Gamma
  2  2  2
  0. 0. 0.
```

### A.1.4 Job script

The job script is the script that is executed for running a simulation.

**Listing A.5:** Script for running a simulation

```
#!/bin/bash
# Job name:
#SBATCH --job-name="Name of job"
#
# Project:
#SBATCH --account=nn9264k
#
# Wall clock limit:
#SBATCH --time=24:00:00
#
# Max memory usage per task:
#SBATCH --mem-per-cpu=3800M
#
# Number of tasks (cores):
#SBATCH --nodes=2 --ntasks-per-node=16
##SBATCH --ntasks=16
#
## Set up job environment
source /cluster/bin/jobsetup
module load vasp/5.3.3
#
## Set up input/output files:
infile="INCAR KPOINTS POSCAR POTCAR CHGCAR WAVECAR"
outfile="CHG CHGCAR CONTCAR DOSCAR EIGENVAL IBZKPT OSZICAR OUTCAR* PCDAT PROCAR WAVECAR XDATCAR vasprun"
```

```
cp $infile $SCRATCH
chkfile $outfile
#
## Do some work:
cd $SCRATCH
mpirun vasp.sh
```

### A.1.5 POTCAR

The POTCAR-file contains information about the pseudopotentials used in the calculations, respectively In\_d, Mn\_sv and O. The POTCAR-files for each atom are combined to one POTCAR-file for the compound. VASP use the POTCAR file to gather information about the atoms (i.e. their mass, valence and energy of the reference configuration for which the pseudopotential was created[52]).

## A.2 Density of state calculations

Density of states calculations were done by utilizing an already relaxed supercell and performing a static calculation, atoms not allowed relax, while making the INCAR parameters listed in Listing A.6 stricter. The k-mesh for the supercell was increased from 2x2x2 to 4x4x4 for increased accuracy. The produced DOSCAR contains the information about density of states for all atoms.

**Listing A.6:** Parameters for a density of state calculation

```
PREC      = High
NSW       = 0
ISIF      = 0
IBRION    = 0
LCHARG    = .TRUE.
ICHARG    = 11
ISMEAR    = -5
LORBIT    = 11
EMIN      = -10
EMAX      = 10
NEDOS     = 601
```

## A.3 Climbing image nudged elastic band calculations

Fixed volume was used to perform the CI-NEB calculations. A few tags to specify characteristics of a CI-NEB calculations were added to the INCAR-file, see Listing A.7. The number of intermediate images is specified in the IMAGES-tag and the spring force is given in the SPRING-tag. The LCLIMB-tag activates the climbing-image nudged elastic band method.

**Listing A.7:** Parameters for a CI-NEB calculation

```
#### Nudged elastic band calculations ####
ISIF      = 2
IBRION    = 1
IMAGES    = 1
SPRING    = -5.0
LCLIMB    = .TRUE.
```

## A.4 Berry-Phase calculations

For Berry-Phase calculations only a few tags were changed in the INCAR-file. The number of ionic steps, NSW, were set to 0 to perform a static calculations and a tag to calculate the polarization, LCALCPOL, was set to true, see Listing A.8.

**Listing A.8:** Parameters for a Berry-Phase calculation

```
NSW       = 0
ISIF      = 0
IBRION    = 0
LCALCPOL  = .TRUE.
```



## Appendix B

# Supplementary from project work - choice of parameters

The following section is taken from the project work performed by the author spring 2014[1]. It includes testing that was done for choosing correct parameters when working with DFT and  $\text{InMnO}_3$ .

### B.1 Convergence testing

Convergence testing has been performed for k-point density and cut-off energy. Testing is done for both structures,  $P6_3cm$  and  $P\bar{3}c1$ , and atomic positions were fully relaxed with fixed unit cell volume. Calculation details for each test is given in Table B.1.

**Table B.1:** Calculation details for test of convergence for k-point density and cut-off energy.

	<b>Relaxation</b>	<b>ENCUT [eV]</b>	<b>EDIFF [eV]</b>	<b>EDIFFG [eV]</b>	<b>K-mesh</b>
K-point	Constant volume	550	10e-6	-0.01	Varying
Cut-off energy	Constant volume	Varying	10e-6	-0.01	4x4x2

### K-point-testing

Calculations were done for the following k-points ( $a \times a \times c$ ): 2x2x1, 3x3x1, 4x4x2, 5x5x3, 6x6x3, 6x6x4, 8x8x4. The length of the c-axis is approximately twice as long as the a-axis, see Table 2.2, and as mentioned before, large is small in reciprocal space and therefore about half the k-point density is necessary along the c-axis compared to the a-axis. Figure B.1a and B.1b shows the total number of k-points ( $a \cdot a \cdot c$ ) plotted against the ground-state energy. The energy difference between  $P\bar{3}c1$  and  $P6_3cm$ ,  $\Delta E_{P\bar{3}c1} - E_{P6_3cm}$ , is plotted in Figure B.1c. By

analyzing the results from the calculations the structures were considered converged with a k-point density of  $4 \times 4 \times 2$ . This k-mesh was used for further calculations.

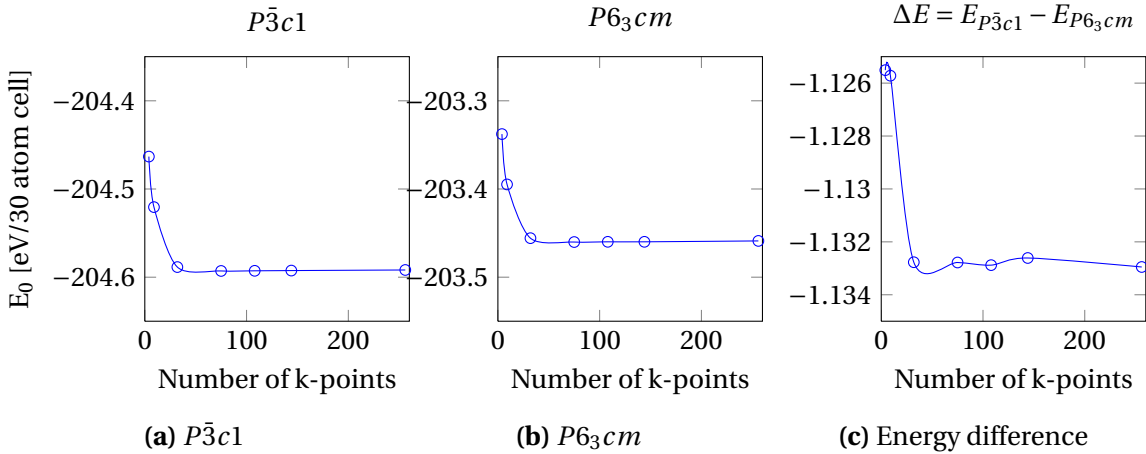


**Figure B.1:** K-point density tests on  $\text{InMnO}_3$  for  $P\bar{3}c1$  and  $P6_3cm$ , and the energy difference between  $P\bar{3}c1$  and  $P6_3cm$ . All calculations were performed with PBEsol and variables as given in Table B.1.

### Cut-off testing

Cut-off testing was done for the following cut-off energies: [250, 300, ..., 650, 700]. The goal for this testing was to find out what cut-off energy is necessary to reach convergence. Figure B.2a and B.2b show the cut-off energies plotted against the ground-state energy for the two structures. The energy difference between  $P\bar{3}c1$  and  $P6_3cm$ ,  $\Delta E = E_{P\bar{3}c1} - E_{P6_3cm}$ , is plotted in figure B.2c. By analysing the results from the calculations both structures were considered converged with a cut-off energy of 550eV and this value was used for further calculations.

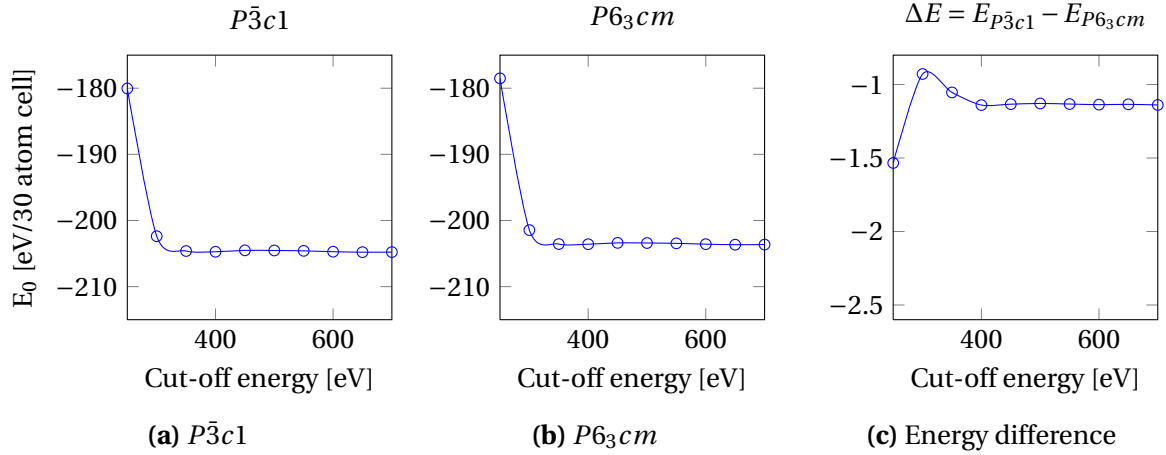


**Figure B.2:** Cut-off energy tests on  $\text{InMnO}_3$  for  $P\bar{3}c1$  and  $P6_3cm$ , and the energy difference between  $P\bar{3}c1$  and  $P6_3cm$ . All calculations were performed with PBEsol and variables as given in Table B.1.

## B.2 The meaning of pseudopotential and Hubbard U

To determine what pseudopotential for Mn that should be used tests were performed for the three combinations given below. The pseudopotential for In was chosen to be In\_d since it represents the potential with most valence electrons, and a detailed and accurate description of In was important for this project. The standard oxygen potential was chosen since it, from experience, has proved to work well. The different Mn potentials are distinguished by looking at the number of valence electrons. Mn includes seven, Mn\_sv includes fifteen and Mn\_pv includes thirteen valence electrons, respectively. A full volume relaxation was done and a 550eV cut-off energy and  $4 \times 4 \times 2$  k-point density were used.

Pseudopotential combinations tested:

1. In\_dMnO
2. In\_dMn\_svO
3. In\_dMn\_pvO

Since DFT gives a poor description of the band gap an electrostatic potential had to be added to the Mn d-orbitals to better reproduce this property. This potential was set through the vari-

able Hubbard U. The goal was to produce a band gap that was as close to the experimental value as possible. There are no reported values for the band gap for  $\text{InMnO}_3$ , but it is assumed that it should be in the range of  $\text{YMnO}_3$  that is given as 1.6 eV[71]. In total, four different values for Hubbard U were tested,  $U = 3, 4, 5, 6$  eV.

Figure B.3 shows the energy difference between  $P\bar{3}c1$  and  $P6_3cm$ ,  $\Delta E = E_{P\bar{3}c1} - E_{P6_3cm}$ , plotted against the Hubbard-U for the different pseudopotentials. By observation the energy difference for Mn and Mn\_pv has nearly a linear increase with Hubbard-U, while Mn\_sv slowly converge when approaching U equal to 5 and 6. Figure B.4 shows how the unit cell volume change with Hubbard-U for the different potential combinations. The unit cell volume increases with increasing Hubbard-U, which explains the added external potential from Hubbard-U[7]. By comparing the graphs it is evident that Mn\_sv has in general lower unit cell volume than the two other combinations and this fit better with the experimental value of  $344.44\text{\AA}^3$  from Table 2.2. The change in band gap with respect to choice of pseudopotential and Hubbard-U in Figure B.5 shows that the potential combinations with Mn and Mn\_pv are not able to reproduce the experimental band gap, even when U increases. Mn\_sv is much closer although it still underestimates the band gap in some extent. When comparing the calculated values for the lattice constants, a and c, with experimental values given in Table 2.2 it is observed that the calculated lattice constants are overestimated. The potential combination with Mn\_sv gives the values closest to the experimental.

For all variables, i.e energy difference, unit cell volume, band gap and lattice parameters, the potential combination with Mn\_sv gives the best fit. Even though it is more computational expensive to use a potential with several valence electrons the Mn\_sv potential is chosen to give better accuracy to the calculations. When choosing Hubbard-U the most important parameter to consider is the band gap. A Hubbard-U of 5eV was chosen to compensate between a correct band gap and accurate volume and lattice constants.



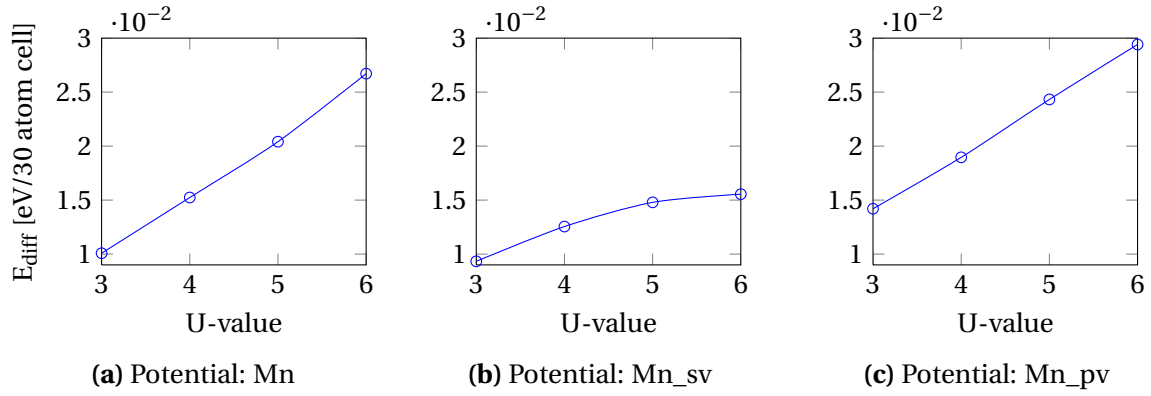


**Figure B.3:** Energy difference between  $P\bar{3}c1$  and  $P6_3cm$  for three potential combinations plotted with respect to values of Hubbard U.

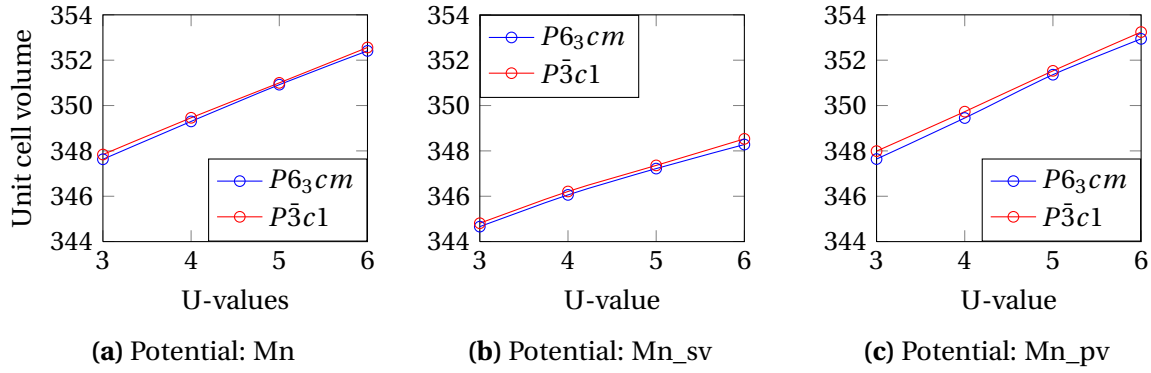


**Figure B.4:** Change in unit cell volume for three potential combinations plotted against Hubbard U for  $P\bar{3}c1$  and  $P6_3cm$  in  $\text{InMnO}_3$ .

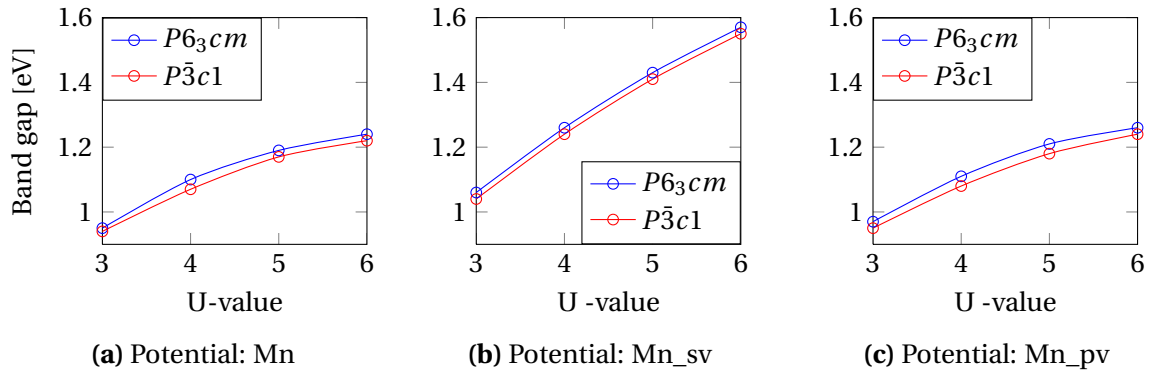


**Figure B.5:** Change in band gap for three potential combinations plotted against Hubbard U for  $P\bar{3}c1$  and  $P6_3cm$  in  $\text{InMnO}_3$ .

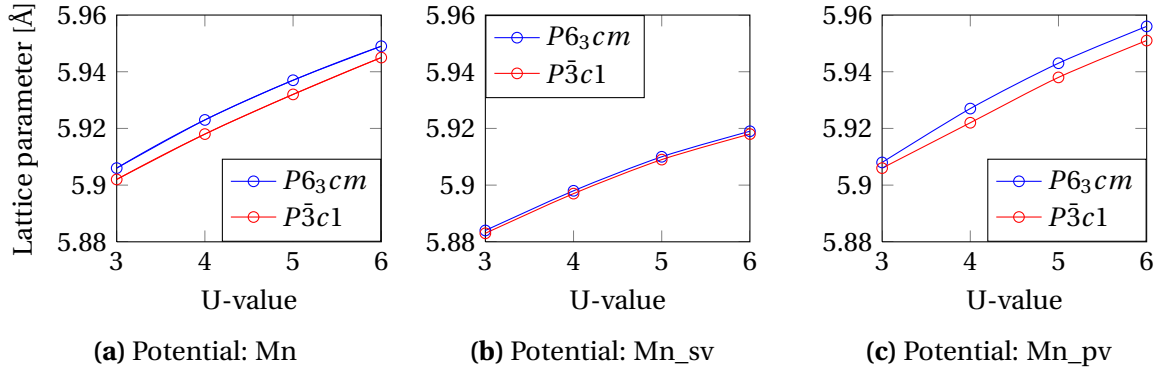


**Figure B.6:** Change in  $a$  lattice parameter for three potential combinations plotted against Hubbard  $U$  for  $P\bar{3}c1$  and  $P6_3cm$  in  $\text{InMnO}_3$ .

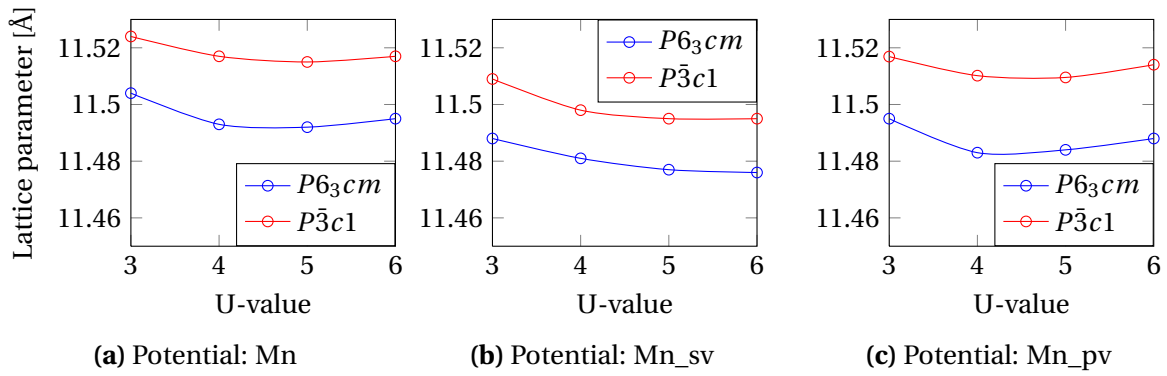


**Figure B.7:** Change in  $c$  lattice parameter for three potential combinations plotted against Hubbard  $U$  for  $P\bar{3}c1$  and  $P6_3cm$  in  $\text{InMnO}_3$ .

## Appendix C

# Results from project work

The following section is taken from the project work performed by the author spring 2014[1]. It includes results from DFT-calculations that are relevant for this thesis.

### C.1 Stoichiometric cell

Table C.1 and Figure C.1 display the calculated energies for a stoichiometric supercell with the  $P\bar{3}c1$  and  $P6_3cm$  structure. The relaxations were done with fixed and relaxed volume as explained in section 5.5.1. Relaxations for the stoichiometric cells were done with and without symmetry constraints. When applying symmetry constraints to calculations the position of specific atoms are held constant, see section 5.6.1.

Table C.2 shows the calculated new lattice parameters and volumes after relaxation compared to experimental values from literature. As mentioned before, each supercell was made by doing a full relaxation of volume and atomic positions for a single unit cell. These unit cells were based on the experimental values for lattice parameters, volume and atomic positions given in Table 2.3. The  $a$  lattice parameters are divided on two and the volumes on four to convert them from a supercell into a unit cell. This will make it easier to compare with experimental values. For better comparison the volume is given in terms of a supercell in Figure C.1. When the single unit cells were fully relaxed the force criterion was set to  $-0.01\text{eV}$ . To be able to achieve convergence for the supercell the value had to be adjusted to  $-0.05\text{eV}$ . This is the reason for the difference in energy for convergence testing on a stoichiometric unit cell and the relaxation of stoichiometric supercells.

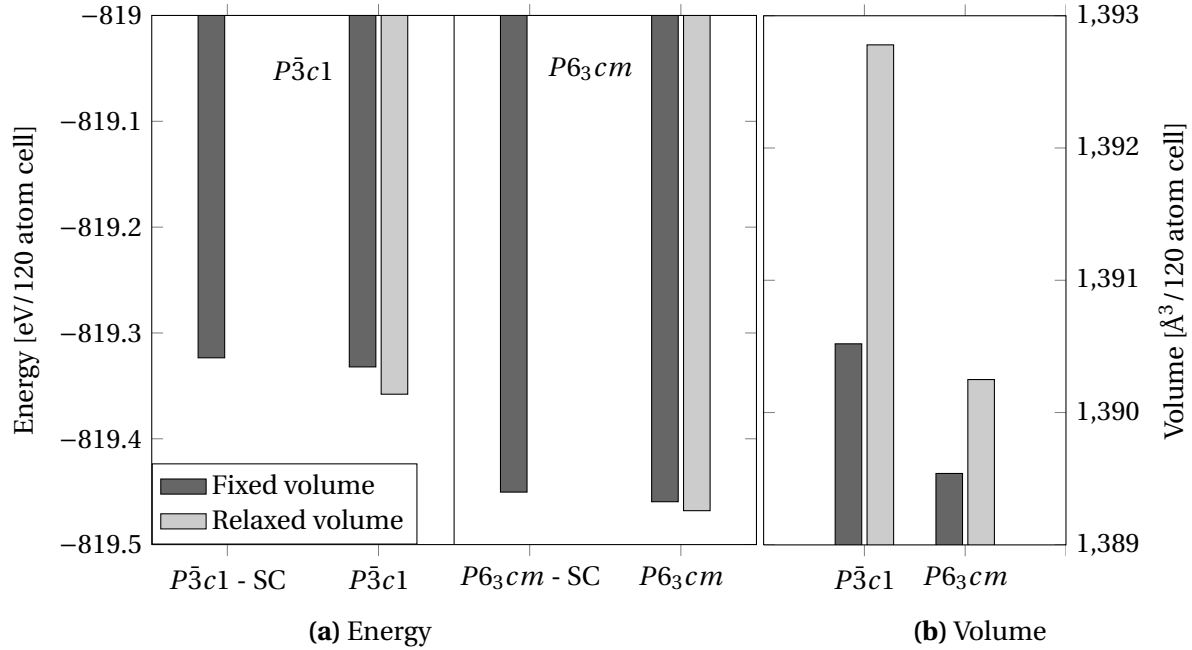


**Figure C.1:** Barplot showing a) the ground-state energies and b) volumes calculated for a stoichiometric supercell cell for  $P\bar{3}c1$  and  $P6_3cm$  with and without symmetry constrains. Relaxation of positions and lattice parameters was done with fixed volume and relaxed volume.

**Table C.1:** Calculated ground-state energy for a stoichiometric supercell for  $P\bar{3}c1$  and  $P6_3cm$ , done with and without symmetry constrains and for fixed and relaxed volume.

Structure	$E_0$ [eV/120 atom cell] w/ fixed volume	$E_0$ [eV/120 atom cell] w/ relaxed volume
$P\bar{3}c1$	-819.33207	-819.35789
$P\bar{3}c1$ - SC	-819.32353	-*
$P6_3cm$	-819.45953	-819.46795
$P6_3cm$ - SC	-819.45038	-*

\*Relaxations were the volume is relaxed was not performed with symmetry constrains (SC), because when the volume changes the atomic positions will change accordingly to each other.

**Table C.2:**  $a$  and  $c$  lattice parameters and volume after full relaxation of atomic position and volume for  $P\bar{3}c1$  and  $P6_3cm$ . Lengths and volume are given in terms of a single unit cell.

Structure	Lattice parameter, $a$ [Å]	Lattice parameter, $c$ [Å]	Volume per unit cell [Å <sup>3</sup> ]
$P\bar{3}c1$ - fixed volume	5.9085	11.4984	347.63
$P\bar{3}c1$ - relaxed volume	5.9097	11.4826	348.20
$P6_3cm$ - fixed volume	5.9140	11.4687	347.39
$P6_3cm$ - relaxed volume	5.9152	11.4754	347.56
<b>Literature values [7]:</b>			
$P\bar{3}c1$ & $P6_3cm$	5.8846	11.4854	344.44

## C.2 Interstitial oxygens

The different interstitial positions are listed in Table C.3 and presented with a yellow atom in the schematics in Figure C.3. Table C.4 lists the ground-state energies after relaxation for the different interstitial oxygen positions in the two structures. Calculations were done with fixed and relaxed volume. Table C.5 lists the lattice parameters and volume per unit cell after the supercells were relaxed in volume and atomic positions. Figure C.2 displays the calculated energies for the different interstitial oxygen positions and volume for  $P\bar{3}c1$  and  $P6_3cm$ . For better comparison the volume is given in terms of a unit cell in Table C.5, while the supercell volumes are showed in Figure C.2.

**Table C.3:** Interstitial oxygen positions in the  $P\bar{3}c1$ - and  $P6_3cm$ -structure for  $\text{InMnO}_3$ . All positions are in the Mn-plane, that means planar positions.

Structure	Site	Position
$P\bar{3}c1$	Oi1	(1/3, 1/3, 3/4)
	Oi2	(2/3, 2/3, 1/4)
$P6_3cm$	Oi1	(1/3, 1/3, 0)
	Oi2	(2/3, 2/3, 1/2)

**Table C.4:** Calculated ground-state energy for a supercell with interstitial oxygen in different positions in  $P\bar{3}c1$  and  $P6_3cm$ . Relaxation of positions and lattice parameters was done with fixed volume and relaxed volume.

Structure	Site	$E_0$ [eV/120 atom cell] w/fixed volume	$E_0$ [eV/120 atom cell] w/relaxed volume
$P\bar{3}c1$	Oi1	-823.98135	-824.05357
	Oi2	-823.93425	-824.03817
$P6_3cm$	Oi1	-823.99531	-824.04214
	Oi2	-823.99250	-824.04124

**Table C.5:** Lattice parameters after full relaxation of atomic positions and volume for  $P\bar{3}c1$  and  $P6_3cm$  with interstitial oxygens in different positions. Lengths and volume are given in terms of a single unit cell.

Structure	Site	Lattice parameter, a [Å]	Lattice parameter, c [Å]	Volume per unit cell [Å <sup>3</sup> ]
$P\bar{3}c1$	Oi1	5.8943	11.4992	348.56
	Oi2	5.8910	11.5059	348.44
$P6_3cm$	Oi1	5.9070	11.4827	348.34
	Oi2	5.9063	11.4840	348.33

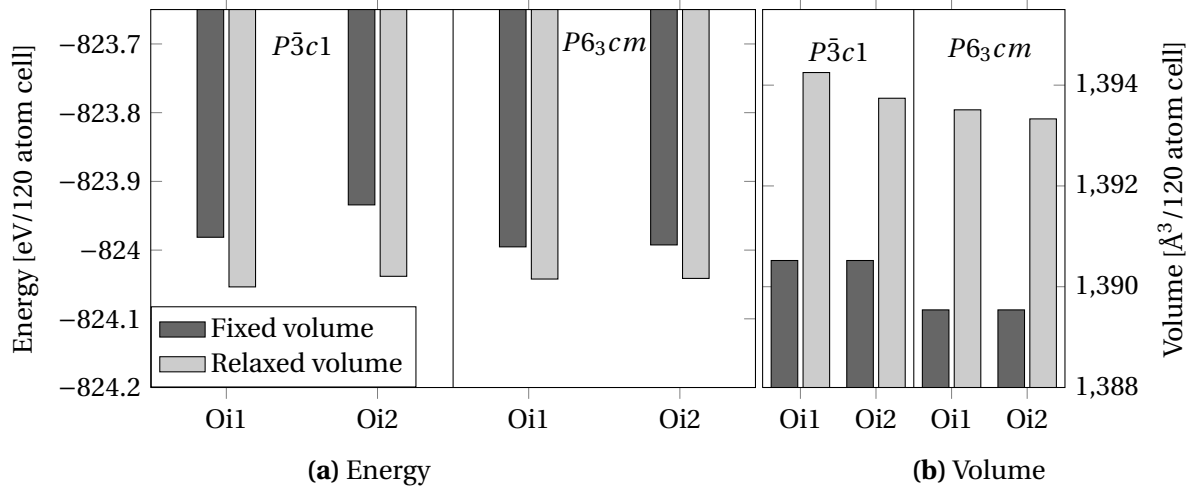


**Figure C.2:** Barplot showing the a) ground-state energy and b) volume calculated for a supercell with interstitial oxygen in different positions in  $P\bar{3}c1$  and  $P6_3cm$ . Relaxation of positions and lattice parameters was done with fixed volume and relaxed volume.

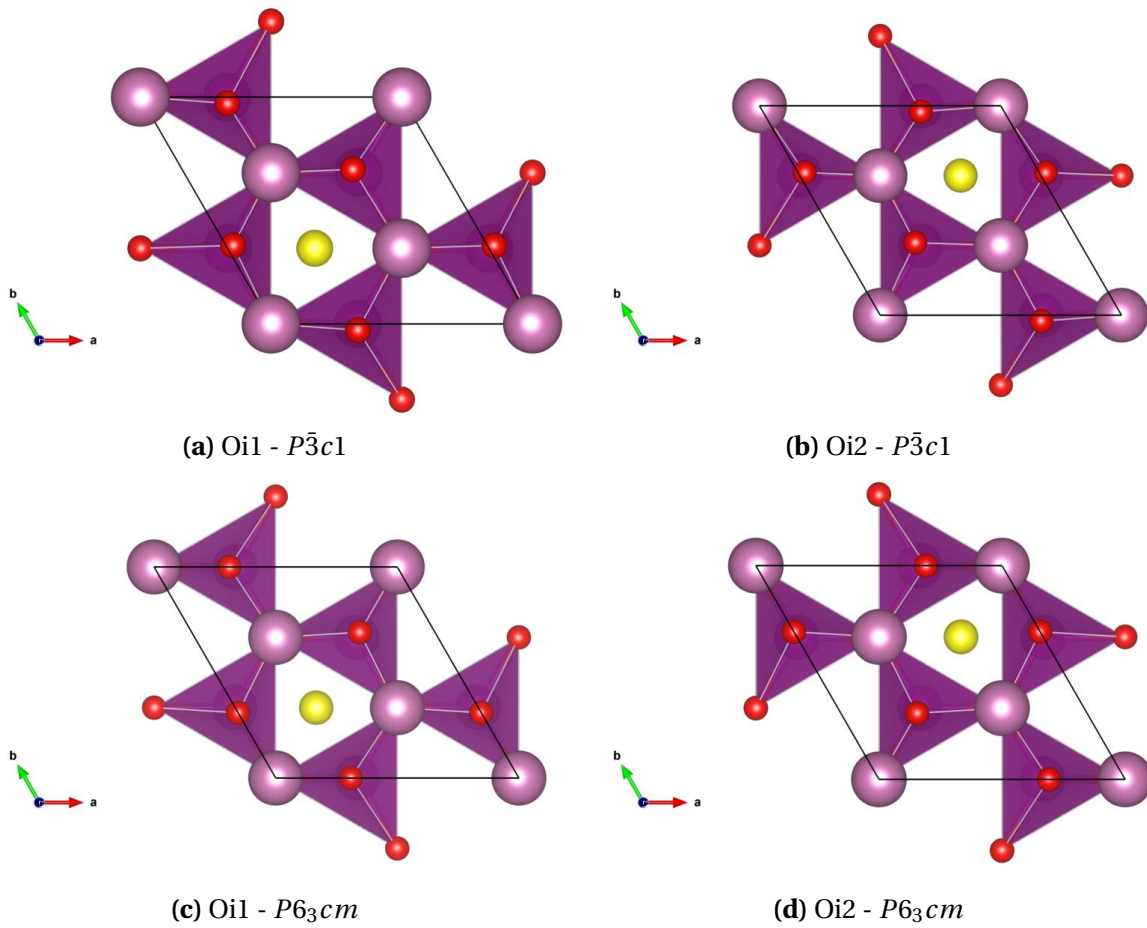


**Figure C.3:** Position of interstitial oxygen, yellow atom, in the  $P\bar{3}c1$  and  $P6_3cm$  structure for  $\text{InMnO}_3$  seen from the  $c$ -axis.

### C.3 Oxygen vacancies

The different oxygen vacancy positions are listed in Table C.6 and presented with an arrow for each position in the schematics in Figure C.5. Table C.7 lists the ground-state energies after relaxation for the different oxygen vacancy positions in the two structures. Calculations were done with fixed and relaxed volume. Table C.8 lists the lattice parameters and volume per unit cell after the supercells were relaxed in volume and atomic positions. Figure C.4 displays the calculated energies for the different oxygen vacancy positions and volume for  $P\bar{3}c1$  and  $P6_3cm$ . For better comparison the volume is given in terms of a unit cell in Table C.8, while the total supercell volumes are showed in Figure C.4.

**Table C.6:** Oxygen vacancy positions in the  $P\bar{3}c1$ - and  $P6_3cm$ -structure for  $\text{InMnO}_3$ .

Structure	Site	Position	Comment
$P\bar{3}c1$	O1	(0,0,1/4)	Planar
	O2	(1/3, 2/3, 0.2313)	Planar
	O3	(0.3171, 0.3412, 0.4142)	Apical
$P6_3cm$	O1	(0.311, 0, 0.1749)	Apical
	O2	(0.6466, 0, 0.3445)	Apical
	O3	(0, 0, 0.4746)	Planar
	O4	(1/3, 2/3, 0.0077)	Planar

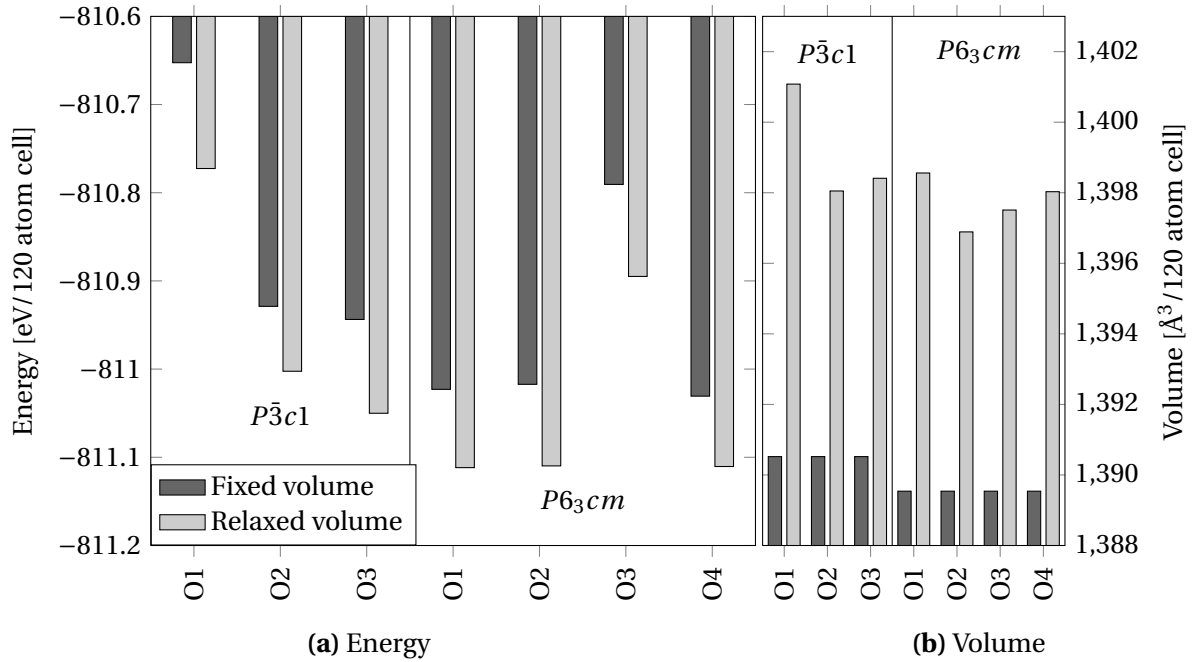
**Table C.7:** Calculated ground-state energy for a supercell with vacant oxygen in different positions in  $P\bar{3}c1$  and  $P6_3cm$ . Relaxation of positions and lattice parameters was done with fixed volume and relaxed volume.

Structure	Site	$E_0$ [eV/120 atom cell] w/fixed volume	$E_0$ [eV/120 atom cell] w/relaxed volume
$P\bar{3}c1$	O1	-810.65253	-810.77252
	O2	-810.92881	-811.00240
	O3	-810.94366	-811.05004
$P6_3cm$	O1	-811.02293	-811.11169
	O2	-811.01723	-811.10971
	O3	-810.79055	-810.89488
	O4	-811.03063	-811.11041

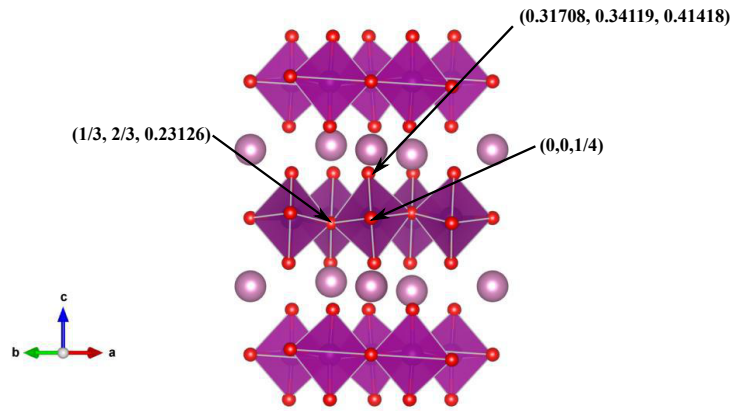
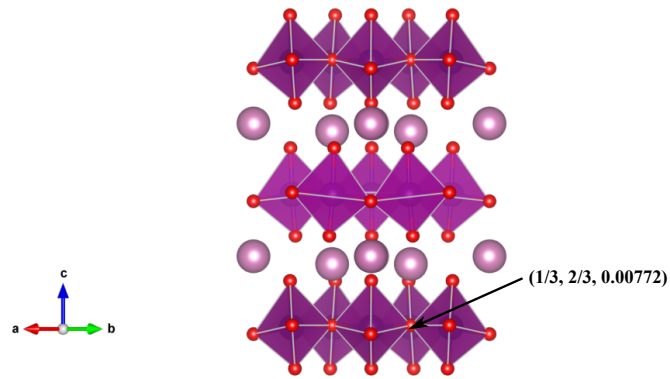
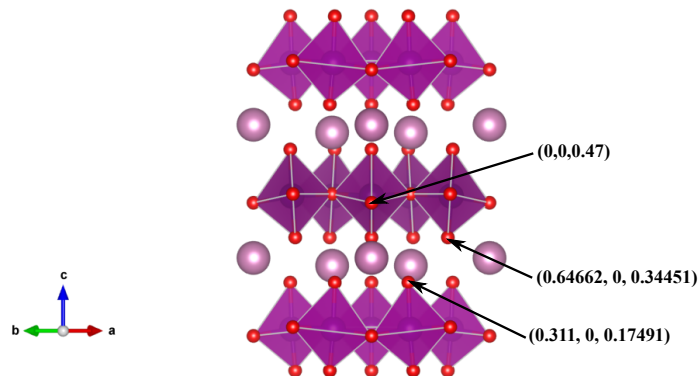


**Table C.8:** Lattice parameters after full relaxation of atomic positions and volume for  $P\bar{3}c1$  and  $P6_3cm$  with vacant oxygens in different positions. Lengths and volume are given in terms of a single unit cell.

Structure	Site	Lattice parameter, a [Å]	Lattice parameter, c [Å]	Volume per unit cell [Å <sup>3</sup> ]
$P\bar{3}c1$	O1	5.9181	11.5171	350.27
	O2	5.9174	11,5120	349.51
	O3	5.9251	11.4696	349.60
$P6_3cm$	O1	5.9338	11.5146	349.64
	O2	5.9360	11.4953	349.22
	O3	5.9363	11.4575	349.38
	O4	5.9292	11.4603	349.51



**Figure C.4:** Barplot showing the a) ground-state energy and b) volume calculated for a supercell with vacant oxygen in different positions in  $P\bar{3}c1$  and  $P6_3cm$ . Relaxation of positions and lattice parameters was done with fixed volume and relaxed volume.

(a)  $P\bar{3}c1$  in  $\bar{1}\bar{1}0$  direction(b)  $P6_3cm$  in  $110$ -direction(c)  $P6_3cm$  in  $\bar{1}\bar{1}0$  direction

**Figure C.5:** Schematic of the position of the different oxygen vacancies in for  $\text{InMnO}_3$  in  $P\bar{3}c1$  and  $P6_3cm$ .

## C.4 Energy differences

Table C.9 presents the calculated energy differences between  $P\bar{3}c1$  and  $P6_3cm$ ,  $\Delta E = E_{P\bar{3}c1} - E_{P6_3cm}$ , for a stoichiometric cell as well as the different interstitial and vacant oxygen positions. The energy differences for defects are calculated by subtracting the ground-state energy for each position, interstitial or vacant, in the  $P\bar{3}c1$ -structure with the ground-state energy of the most stable position, interstitial or vacant, in the  $P6_3cm$ -structure.

**Table C.9:** Energy differences between the different point defect positions for  $P\bar{3}c1$  and the most stable point defect position for  $P6_3cm$ . Relaxations of positions and lattice parameters were done with fixed volume and relaxed volume.

Type	Site	Energy diff. [eV/120 atom cell] w/fixed volume	Energy diff. [eV/120 atom cell] w/relaxed volume
Stoc.	Symmetry constrained	0.12685	-
	Free	0.12746	0.11006
O <sub>i</sub>	Oi1	0.01396	-0.01143
	Oi2	0.06106	0.00397
V <sub>O</sub>	O1	0.37810	0.33789
	O2	0.10182	0.10801
	O3	0.08697	0.06037



## Appendix D

# Vapour pressure of In and Y

To calculate the vapour pressure for In(s) and Y(s) at different temperatures the equation and values from table "Vapor Pressure of the Metallic Elements" in *CRC Handbook of Chemistry and Physics*[72] were used. Equation D.1 gives the formula for calculating the vapour pressure at different temperatures, where T is in Kelvin [K]. Figure D.1 lists the constants in the equation for In(s) and Y(s) respectively. Table D.2 shows the calculated vapour pressures for In(s) and Y(s) at different temperatures.

$$\log p[\text{atm}] = A + \frac{B}{T} + C \log(T) + \frac{D}{T^3} \quad (\text{D.1})$$

**Table D.1:** Constants for calculating the vapour pressure with equation D.1 for In(s) and Y(s).

Compound	A	B	C	D
In-sol.	5.991	-12548	0	0
Y-sol.	9.735	-22306	-0.8705	0

**Table D.2:** Calculated vapour pressure for In(s) and Y(s) at different temperatures with equation and constant from "Vapor Pressure of the Metallic Elements" in *CRC Handbook of Chemistry and Physics*[72]

Temp.[C°]	Vapour pressure for In(s) [atm]	Vapour pressure for Y(s) [atm]
25	$7.65 \cdot 10^{-37}$	$5.36 \cdot 10^{-68}$
100	$2.24 \cdot 10^{-28}$	$4.95 \cdot 10^{-53}$
200	$2.90 \cdot 10^{-21}$	$1.77 \cdot 10^{-40}$
500	$5.73 \cdot 10^{-11}$	$2.31 \cdot 10^{-22}$
1000	$1.36 \cdot 10^{-04}$	$3.24 \cdot 10^{-11}$
2000	$2.95 \cdot 10^{+00}$	$9.99 \cdot 10^{-04}$